Electronic states and optical properties of quantum well heterostructures with strain and electric field effects

Desmond Michael Ryan

Ryan, Desmond Michael (1997) Electronic states and optical properties of quantum well heterostructures with strain and electric field effects. Doctoral thesis, Durham University.

To

Helen

Atque inter silvas Academi quaerere verum.

Horace 65-8 B. C.

Electronic States and Optical Properties of Quantum Well Heterostructures with Strain and Electric Field Effects.

by

Desmond Michael Ryan

Submitted for the degree of Doctor of Philosophy

Department of Physics,

University of Durham

September 1997

ABSTRACT

The aim of this work was to develop an envelope function method to calculate the electronic states and optical properties of complex quantum well heterostructures, and to demonstrate its effectiveness by application to some device structures of topical interest. In particular, structures have been considered which might form the basis of intensity modulators and polarization insensitive amplifier devices for light at a wavelength of 1.55 μm.

The modulator structures considered all have the general form of two coupled quantum wells of different widths as the active region. The application of an electric field in the growth direction is intended to result in a shift in the energy and spatial localisation of the confined states and produce an increase in the absorption coefficient at longer wavelengths than the zero field absorption edge. The effectiveness of certain structures is examined in terms of field induced absorption increase at 1.55 μm. A system which shows a significant increase in absorption coefficient at this wavelength on application of a practical electric field has been identified as a possible candidate for an intensity modulator.

In the case of the amplifier, the active region of the most promising structure considered consists of a stepped well which comprises two layers, one with tensile and one with compressive strain. It is known that the presence of the two oppositely

strained layers can result in the TE and TM gain peaks appearing at similar photon energies. Our calculations show that a suitable choice of strain and layer widths can result in a small or zero difference between the TE and TM gains at 1.55 μm, which can be important for the polarization insensitive operation of devices in optical communications applications.

In order to predict the optical properties of quantum well devices it is necessary to calculate the electron and hole states for a range of in-plane wavevectors. The calculations developed and carried out in this work are based on a multi-layer (eight band) ***k.p*** model including strain effects. The interfacial boundary conditions which result from approximations to Burt's exact envelope function theory are included in the model. The effect of an electric field is modelled by including a potential energy term in each layer Hamiltonian which is equal to the average energy shift across the layer in question due to the presence of the field. The model has been developed with flexibility in mind and has applications beyond the specific devices considered in this thesis.

ACKNOWLEDGEMENTS

I wish to thank my supervisor, Dick Abram, for the gargantuan amount of encouragement, direction and advice he has given me during my time at Durham. His energy, sense of humour and profound understanding of physics have made this project both stimulating and enjoyable. I wish to thank David Robbins, my industrial supervisor, for his advice and guidance on a number of the devices examined in this thesis. He made my numerous visits to Caswell very pleasant and fruitful, and indeed made me feel very much part of the team. My thanks also for providing me with a number of programs and experimental data and for the help from his colleagues Jeanette Fine, Joe Metcalf, Andrew Wood and Joy Thompson. I wish to thank Stuart Brand for providing me with the 1D effective mass energy solver, for his help on a number of bandstructure issues and for his wry sense of humour. I would also like to thank Mark Walmsley for his advice on the multi-layer method and for making his programs available to me. I would like to thank the boys Dave (Wavy), Gavin, Dan, Rick, Dave (tng) and Steve for numerous physics discussions over a half at the local tavern. They also made worthy computer chess (aka *DOOM*) opponents from time to time.

I would particularly like to thank my wife, Helen, for all the love, friendship, support, encouragement and patience she has shown me over the duration of this work. Not many people would put up with their partner leaving paid employment, selling a house and moving nearly three hundred miles to live in student accommodation so as to satisfy their academic desires. Helen...you are the best (*Et vera incessu patuit dea* Virgil 70-19 B.C.).

Financial support from EPSRC and GEC-Marconi Materials Technology is acknowledged.

CONTENTS

DECLARATION

I hereby declare that the work reported in this thesis has not been previously submitted for any degree and is not being currently submitted in candidature for any other degree. The work reported in this thesis was carried out by the candidate.

CHAPTER ONE

INTRODUCTION

The development of the epitaxial growth techniques of molecular beam epitaxy (MBE) and metal-organic chemical vapour deposition (MOCVD) [1-4] have made possible the fabrication of very thin high quality semiconductor layers on a bulk semiconductor substrate. Normally, individual epilayer thicknesses range from 20 to as much as 2000 angstroms, although thicker and thinner layers are quite feasible. MBE and MOCVD also allow precise control of the chemical composition of the growing crystal providing the ability to grow successive thin layers of different elemental, compound or alloy semiconductors to form a heterostructure [1,2,8,9].

The growth of a thin (≤ 1000 angstroms) layer of narrow bandgap semiconductor between two wider bandgap semiconductor layers can result in the physical realisation of a finite square well potential where electrons exhibit quantum mechanical behaviour - a quantum well [10]. In some cases, *AlGaAs/GaAs/AlGaAs* for instance, both the holes in the valence band and the electrons in the conduction band experience a bandedge profile essentially equivalent to a square potential well. The carriers are free to move in the plane of the well, but are confined in the growth direction. The spatial confinement in the growth direction produces quantised energy levels [3,8,10]. If carrier-carrier interactions are ignored and the effective mass model of carrier behaviour used, then the quantised energy levels relative to the bandedge are just a function of the well width, the depth of the well and the carrier effective mass in the barrier and well layers. For given barrier and well materials, the energy separation between the electron and hole levels can be tailored by adjusting the width of the well layer. This ability to tune the energy bandgap of the quantum well structure has important applications particularly in semiconductor lasers and light emitting diodes. The quantum well laser can be designed so that the emission wavelength corresponds to the wavelength of minimum loss and dispersion for silica based optical fibres which are used for long distance telecommunications. It is also possible to produce bulk materials with a continuous range of bandgaps by the process of alloying. For example the two binaries *GaAs* and *AlAs* can form the alloy $Al_xGa_{1-x}As$, which has a bandgap determined by the relative ratio of the constituent binaries [3,4]. Hence alloys provide the means to grow quantum well structures of a fixed geometry but with different bandgaps and confining potentials.

The growth of high quality semiconductor heterostructures was initially restricted to so called lattice matched systems, such as *GaAs*/*AlGaAs*, where the constituent materials have very similar lattice constants. However it is now possible to grow routinely high quality heterostructures made up of layers of semiconductors with different lattice constants. Misfit dislocations can be avoided in sufficiently thin layers when the crystal structure of each layer elastically deforms to produce matching of the lattice constant in the plane of each interface [3,11-14]. The resultant strain in semiconductor layers provides a further degree of control, particularly through the bandstructure where strain modifies the bandgap and produces splittings of degeneracies in the bandstructures such as that of the heavy and light hole bands at the top of the valence band and satellite valleys in the conduction band. For quantum wells, the presence of a compressively strained well layer results in a reduced in-plane effective mass of the highest valence subband, which is heavy hole in character. This leads to a reduced threshold current for lasers based on compressively strained quantum wells [11,15]. The combination of thin layers from precision epitaxial layer growth techniques, semiconductor alloying and the incorporation of strain have resulted in the field of bandstructure engineering where devices with tailored electronic or optical characteristics can be grown [11]. Semiconductor heterostructures have also led to the discovery of new fundamental physical phenomena such as the quantum Hall effect [5,6,7].

In this thesis we describe the development of an envelope function method to calculate the electronic states and optical properties of complex quantum well heterostructures and demonstrate its effectiveness by application to some device structures of topical interest. The structures considered are relevant to modulators and amplifiers which find application in optical communications systems [3,15]. Calculations of the optical response for both devices have been carried out in an attempt to predict device effectiveness. For the modulator, the active region consists of two coupled quantum wells of different widths [16]. The application of an external electric field in the growth direction results in a shift in the energy of the confined states (the quantum confined Stark effect [3]) and a change in the spatial localisation of the states. The change in the absorption of light with electric field at a wavelength of 1.55 μm is the primary concern. In the case of the amplifier, the active region of the most promising structure considered consists of a stepped well which comprises two layers, one with tensile and one with compressive strain [17]. The presence of the two oppositely strained layers can result in the highest heavy hole and light hole subbands being at similar energies, and the energy separation between these and the lowest conduction subband being less than 0.8 eV. The polarization sensitivity of the gain at a wavelength of 1.55 μm is considered in this work.

In order to predict the optical properties of the structures described above it is necessary to calculate the electron and hole states for a range of in-plane wavevectors. Our calculations are based on an eight band ***k.p*** method. Until recently the theory of envelope function behaviour at heterointerfaces had been contentious, but many of the issues have now been resolved by the development of an exact envelope function theory by Burt [18]. The required heterointerface boundary conditions are calculated for the eight band approach using an approximation to the exact envelope function theory and included in the ***k.p*** model of heterostructures [19]. The effect of electric field has been included by breaking the structure in to many thin slices where the electrostatic potential can be taken as spatially constant. It should be emphasised that the electronic structure calculation has been developed with flexibility in mind and has applications beyond the specific devices considered in this thesis. For example the bandstructure model could also be used to examine quantum well cascade lasers [3,20-22] and piezo-electric structures (when a zincblende crystal is strained in the (111) direction, a large internal field is generated)

[23-25]. The model can also be applied to quantum well structures which require self-consistent calculations due to the effects of carrier charge such as modulation [3,7,26] and delta doped structures [27,28].

Chapter 2 describes the calculation of the electronic states of single strained quantum wells using a complex bandstructure approach based on the eight band ***k.p*** method. The interfacial boundary conditions which result from approximations to Burt's exact envelope function theory are calculated and included in the bandstructure model. The effects of these boundary conditions on the electronic states and bandstructure are compared to those derived from the more usual symmetrized Hamiltonian approach for a single tensilely strained quantum well. The chapter concludes with a demonstration of how the information on the bandstructure and the wave functions can be used to predict the optical absorption of a quantum well structure. If further approximations are made, the ***k.p*** approach can be reduced to a much simpler one-dimensional effective mass model which is particularly well suited to the rapid calculation of the energies and wave functions of the electronic states at zero in-plane wavevector.

Chapter 3 describes the calculation of the electronic states and bandstructure of an asymmetric coupled quantum well system in an external applied electric field. The method of solution follows that for a single quantum well except that the active region is broken up into a finite number of layers. The effect of the electric field is modelled by including a potential energy term in each layer Hamiltonian which is equal to the average energy shift in the layer in question due to the presence of the field. Solutions are found by matching the layer solutions at each interface. The model is applied to two coupled quantum well structures which have been proposed by GEC-Marconi as possible candidates for light intensity modulators at a wavelength of 1.55 μm. The field dependent absorption spectra for the two structures are calculated and the results examined in terms of light intensity modulation at 1.55 μm. GEC-Marconi did attempt to grow the structures using MOVPE but unfortunately the grown devices deviated from the target specification. Nevertheless the comparison between the theoretical predictions and the experimental measurements that is presented is instructive. The state energies, envelope functions and relevant optical matrix elements are also calculated as a function of electric field using the one-dimensional effective mass model and are compared to those obtained from the ***k.p*** model.

Chapter 4 examines the polarization sensitivity of the gain for two types of quantum well structure. The first is a single tensilely strained quantum well, but the second provides the basis for a more effective device and consists of a stepped well which comprises two layers, one with tensile and one with compressive strain. Three structures of the second type are examined. The net TE and TM gains, which include optical confinement effects and carrier dependent bandgap narrowing, are calculated for a range of carrier densities. The results are discussed in terms of the polarization sensitivity of the gain, the bandwidth over which the polarization sensitivity is acceptably low and the maximum achievable gain at 1.55 μm.

Chapter 5 presents the conclusions and suggestions for further work.

References for Chapter One

[1] T. P. Pearsall, *GaInAsP alloy semiconductors*, Wiley (1982)

[2] S. M. Sze, *Physics of semiconductor devices*, Wiley (1981)

[3] J. Singh, *Semiconductor optoelectronics*, McGraw-Hill (1995)

[4] M. Zambuto, *Semiconductor devices*, McGraw-Hill (1989)

[5] R. B. Laughlin, Phys. Rev. B, **50**, 1395 (1983)

[6] J. K. Jain, Science, **266**, 1199 (1994)

[7] K. Seegar, *Semiconductor physics: an introduction* 5th ed., Springer-Verlag (1991)

[8] C. Weisbuch and B. Vinter, *Quantum semiconductor structures: fundamentals and applications*, Academic Press (1991)

[9] H. C. Casey Jr. and M. B. Panish, *Heterostructure Lasers Part A: fundamental principles*, Academic Press (1978)

[10] F. K. Richtmyer, E. H. Kennard and J. N. Cooper, *Introduction to modern physics* 6th ed., TATA McGraw-Hill (1986)

[11] E. P. O' Reilly, Semicond. Sci. Technol., **4**, 121 (1989)

[12] I. J. Fritz, S. T. Picraux, L. R. Dawson, T. J. Drummond, W. D. Laidig and N. G. Anderson, Appl. Phys. Lett., **46**, 967 (1985)

[13] T. J. Andersson, Z. G. Chen, V. D. Kulakovskii, A. Uddin and J. T. Vallin, Appl. Phys. Lett., **51**, 752 (1987)

[14] D. J. Dunstan and A. R. Adams, Semicond. Sci. Technol., **5**, 1202 (1990)

[15] P. J. A. Thijs, L. F. Tiemeijer, J. J. M. Binsma and T. van Dongen, IEEE J. Quant. Elect., **30**, 477 (1994)

[16] S. J. Kim, Y. T. Oh, S. K. Kim, T. W. Kang and T. W. Kim, J. Appl. Phys., **77**, 2486 (1995)

[17] D. Sigogne, A. Ougazzaden, D. Meichenin, B. Mersali, A. Carenco, J. C. Simon, I. Valiente, C. Vassallo and L. Billes, Electron. Lett., **32**, 1403 (1996)

[18] M. G. Burt, J. Phys: Condens. Matter, **4**, 6651 (1992)

[19] B. A. Foreman, Phys. Rev. B, **48**, 4964 (1993)

[20] J. Faist, Science, 264, **553**, (1994)

[21] S. J. Eglash and H. K. Choi, Appl. Phys. Lett., **64**, 833 (1994)

[22] R. Q. Yang, Appl. Phys. Lett., **66**, 959 (1995)

[23] D. L. Smith, Solid State Commun., **57**, 919 (1986)

[24] D. L. Smith and C. Mailhiot, Phys. Rev. B, **35**, 1242 (1987)

[25] D. L. Smith and C. Mailhiot, J Vac. Sci. Technol., **A7**, 609 (1989)

[26] F. Y. Huang, J. Li, L. M. Li and H. Morkoc, Appl. Phys. Lett., **63**, 1669 (1993)

[27] W. Batty and D. W. E. Allsopp, Electron. Lett., **29**, 2066 (1993)

[28] W. Batty and D. W. E. Allsopp, IEEE Photon. Technol. Lett., **7**, 635 (1995)

CHAPTER TWO

QUANTUM WELL BANDSTRUCTURE AND OPTICAL ABSORPTION

2.1 Introduction

The main subject of this chapter is the calculation of the electronic states of strained and unstrained semiconductor quantum wells. The chapter is concluded with a demonstration of how the information on the bandstructure and wave functions can be used to predict the optical properties of a quantum well structure, in particular the absorption coefficient. The electronic structure is calculated by applying Burt's envelope function formalism which provides a well defined treatment of wave functions at heterointerfaces. This approach is compared with an alternative by considering the bandstructure and wave functions for a tensilely strained quantum well. A much simpler one-dimensional effective mass model is also developed which is particularly suited to the rapid calculation of the confined electronic states at zero in-plane wavevector. The calculational methods discussed in this chapter form the basis of the theoretical study of quantum heterostructures in the remainder of the thesis.

2.2 Bulk bandstructure

The energy eigenfunctions of an electron moving in the periodic potential of a semiconductor crystal may be written in Bloch form

$$\psi = u_{nk}(\boldsymbol{r})e^{i\boldsymbol{k}.\boldsymbol{r}} \tag{1}$$

where $u_{nk}(\boldsymbol{r})$ is called the Bloch periodic part of the wave function for band n and has the periodicity of the potential. In the reduced zone scheme the wave vector $\boldsymbol{k}$ is required to lie in the first Brillouin zone. The Bloch periodic part for any given $\boldsymbol{k}$ in band n, may be expressed as a linear combination of the Bloch periodic parts of the infinite set of bands at some single value of wavevector $\boldsymbol{k_0}$:

$$u_{nk}(\boldsymbol{r}) = \sum_m c_{mn}(\boldsymbol{k}-\boldsymbol{k_0})\, u_{m\mathbf{k}_0}(\boldsymbol{r}) \tag{2}$$

In practice it is normally possible to obtain a satisfactory representation of $u_{nk}(\boldsymbol{r})$ while restricting the sum in eq (2) to a finite number (typically ≤ 30) of terms. In particular when, as here, only states close to the edges of the conduction and valence bands are of interest, it is common to use eight basis functions $u_{m\mathbf{k}_0}(\boldsymbol{r})$ where $\boldsymbol{k_0}$ corresponds to the zone centre ($\boldsymbol{k_0} = 0$) and m to the heavy, light and spin split off valence bands and the conduction band for the two spin configurations. Combining eqs.(1) and (2) and substitution into the Schrodinger equation yields

$$\left[\frac{-\hbar^2}{2m}\nabla^2 - \frac{i\hbar^2}{m}\boldsymbol{k}.\nabla + \frac{\hbar^2 k^2}{2m} + V(\boldsymbol{r})\right]\sum_m c_{mn}u_{m0}(\boldsymbol{r}) = E_n(\boldsymbol{k})\sum_m c_{mn}u_{m0}(\boldsymbol{r}) \tag{3}$$

Multiplying on the left by $u_{n0}{}^*(\boldsymbol{r})$ and integrating over the unit cell gives

$$\sum_m\left(\left[E_n(\boldsymbol{k}) - \left(E_n(0) + \frac{\hbar^2 k^2}{2m}\right)\right]\delta_{nm} - \frac{\hbar}{m}\boldsymbol{k}.\boldsymbol{p}_{nm}\right)c_{mn} = 0 \tag{4}$$

where

$$\boldsymbol{p}_{nm} = \int_{unitcell} u^*_{n0}(\boldsymbol{r})\boldsymbol{p}\, u_{m0}(\boldsymbol{r})d\boldsymbol{r} \tag{5}$$

Equations (2) - (5) define the ***k.p*** representation. The above set of eight equations can be written in matrix form as

$$(\boldsymbol{H}-\lambda)\boldsymbol{c} = 0 \qquad (6)$$

where the eigenvalue λ represents the $E_n(\boldsymbol{k})$ in eq.(4) and $\boldsymbol{H}$ the remaining terms in the brackets. For each value $E_n(\boldsymbol{k})$ of the eigenvalue λ there is an eigenvector $\boldsymbol{c}$ with components c_{mn}, the coefficients in eq.(2), which define the wave function of the state in band n at wavevector $\boldsymbol{k}$.

Whilst we have limited our expansion in eq.(2) to eight basis functions it is found that interactions between these bands of interest and those that are energetically remote result in significant modifications to the respective bandstructures. In this work the interactions between the eight basis states and the remote bands are included perturbatively using the standard Lowdin approach [5].

The region of the semiconductor bandstructure of interest for optical devices considered here is that around the fundamental energy gap, which separates the occupied states from the unoccupied states of intrinsic material at absolute zero temperature. These states are derived from the outer, partially filled atomic shells of the constituent atoms. For example, in the case of the semiconductor *GaAs* the group *III* element *Ga* has an outer shell $4s^2 4p^1$ and the group *V* element *As* has an outer shell $4s^2 4p^3$ and both play a role in forming the electronic states around the energy gap. The valence band maximum is derived from atomic *p* orbitals (dominated by *As* *p*-states), and is split by the spin-orbit interaction into upper fourfold-degenerate states (Γ_8) with j=3/2 and lower twofold-degenerate states (Γ_7) with j=1/2, where j is the total angular momentum quantum number. The states at the conduction band minimum for a direct gap semiconductor (Γ_6) have wave functions that are derived from atomic s orbitals (dominated by *Ga* s-states). Therefore, it is appropriate to use the eight zone centre states (Γ_6, Γ_7 & Γ_8) to form the basis set of the Hamiltonian (Table 1).

	ψ	$\left\|j,m_j\right\rangle$	
u_1	$\left\|S\uparrow\right\rangle$	$\left\|\frac{1}{2},\frac{1}{2}\right\rangle$	Conduction
u_2	$\sqrt{\frac{1}{2}}\left\|(X+iY)\uparrow\right\rangle$	$\left\|\frac{3}{2},\frac{3}{2}\right\rangle$	Heavy hole
u_3	$\sqrt{\frac{1}{6}}\left\|(X+iY)\downarrow\right\rangle-\sqrt{\frac{2}{3}}\left\|Z\uparrow\right\rangle$	$\left\|\frac{3}{2},\frac{1}{2}\right\rangle$	Light hole
u_4	$\sqrt{\frac{1}{3}}\left[\left\|(X+iY)\downarrow\right\rangle+\left\|Z\uparrow\right\rangle\right]$	$\left\|\frac{1}{2},\frac{1}{2}\right\rangle$	spin split off
u_5	$\left\|S\downarrow\right\rangle$	$\left\|\frac{1}{2},-\frac{1}{2}\right\rangle$	Conduction
u_6	$\sqrt{\frac{1}{2}}\left\|(X-iY)\downarrow\right\rangle$	$\left\|\frac{3}{2},-\frac{3}{2}\right\rangle$	Heavy hole
u_7	$-\sqrt{\frac{1}{6}}\left\|(X-iY)\uparrow\right\rangle-\sqrt{\frac{2}{3}}\left\|Z\downarrow\right\rangle$	$\left\|\frac{3}{2},-\frac{1}{2}\right\rangle$	Light hole
u_8	$-\sqrt{\frac{1}{3}}\left[\left\|(X-iY)\uparrow\right\rangle-\left\|Z\downarrow\right\rangle\right]$	$\left\|\frac{1}{2},-\frac{1}{2}\right\rangle$	spin split off

Table 1: *The basis set of the Hamiltonian,* ***H****, in eq.(6).*

where *S* denotes *s* type atomic orbitals

X, Y & Z denote p_x, p_y & p_z type atomic orbitals

$\uparrow$&$\downarrow$ indicate spin up and spin down

j is the total angular momentum quantum number

m_j is the z component of the total angular momentum quantum number

With this basis the Hamiltonian follows [1,2,5,6] as given in Table 2.

In Table 2

$$k_{\parallel}^2 = k_x^2 + k_y^2 \tag{7}$$

$$k_+ = k_x + i\,k_y \tag{8}$$

$$k_- = k_x - i\,k_y \tag{9}$$

As written, all wavevectors in Table 2 are expressed in units of $\sqrt{\hbar^2/2m}$ where m is the free electron mass. That is any factor of wavevector should be multiplied by $\sqrt{\hbar^2/2m}$ to correspond to the notation in the text. Also

$$P = \sqrt{\frac{2m}{\hbar^2}}\,P_{kane} \tag{10}$$

$$P_{kane} = -i\frac{\hbar}{m}\langle s|\,p_x\,|x\rangle \tag{11}$$

$$p_x = \frac{\hbar}{i}\frac{\partial}{\partial x} \tag{12}$$

E_c = energy of the edge conduction band (at the Γ point)

E_v = energy of the edge valence band (at the Γ point)

Δ = spin orbit splitting energy (at the Γ point)

$$\begin{bmatrix}
sk^2+E_c & \sqrt{\frac{1}{2}}iPk_+ & -\sqrt{\frac{2}{3}}iPk_z & \sqrt{\frac{1}{3}}iPk_z & 0 & 0 & -\sqrt{\frac{1}{6}}iPk_- & -\sqrt{\frac{1}{3}}iPk_- \\
-\sqrt{\frac{1}{2}}iPk_- & \begin{array}{c}(2\gamma_2-\gamma_1)k_z^2+E_v\\ -(\gamma_1+\gamma_2)k_\parallel^2\end{array} & 2\sqrt{3}\gamma_3k_-k_z & -\sqrt{6}\gamma_3k_-k_z & 0 & 0 & \begin{array}{c}\sqrt{3}\gamma_2(k_x^2-k_y^2)\\ -2\sqrt{3}i\gamma_3k_xk_y\end{array} & \begin{array}{c}\sqrt{6}\gamma_2(k_x^2-k_y^2)\\ -2\sqrt{6}i\gamma_3k_xk_y\end{array} \\
\sqrt{\frac{2}{3}}iPk_z & 2\sqrt{3}\gamma_3k_+k_z & \begin{array}{c}-(\gamma_1+2\gamma_2)k_z^2\\ +(\gamma_2-\gamma_1)k_\parallel^2+E_v\end{array} & \begin{array}{c}2\sqrt{2}\gamma_2k_z^2\\ -\sqrt{2}\gamma_2k_\parallel^2\end{array} & -\sqrt{\frac{1}{6}}iPk_- & \begin{array}{c}-\sqrt{3}\gamma_2(k_x^2-k_y^2)\\ +2\sqrt{3}i\gamma_3k_xk_y\end{array} & 0 & -3\sqrt{2}\gamma_3k_-k_z \\
-\sqrt{\frac{1}{3}}iPk_z & -\sqrt{6}\gamma_3k_+k_z & \begin{array}{c}2\sqrt{2}\gamma_2k_z^2\\ -\sqrt{2}\gamma_2k_\parallel^2\end{array} & \begin{array}{c}-\gamma_1k_z^2+E_v\\ -\gamma_1k_\parallel^2-\Delta\end{array} & -\sqrt{\frac{1}{3}}iPk_- & \begin{array}{c}-\sqrt{6}\gamma_2(k_x^2-k_y^2)\\ +2\sqrt{6}i\gamma_3k_xk_y\end{array} & 3\sqrt{2}\gamma_3k_-k_z & 0 \\
0 & 0 & \sqrt{\frac{1}{6}}iPk_+ & \sqrt{\frac{1}{3}}iPk_+ & sk^2+E_c & \sqrt{\frac{1}{2}}iPk_- & -\sqrt{\frac{2}{3}}iPk_z & \sqrt{\frac{1}{3}}iPk_z \\
0 & 0 & \begin{array}{c}-\sqrt{3}\gamma_2(k_x^2-k_y^2)\\ -2\sqrt{3}i\gamma_3k_xk_y\end{array} & \begin{array}{c}-\sqrt{6}\gamma_2(k_x^2-k_y^2)\\ -2\sqrt{6}i\gamma_3k_xk_y\end{array} & -\sqrt{\frac{1}{2}}iPk_+ & \begin{array}{c}(2\gamma_2-\gamma_1)k_z^2+E_v\\ -(\gamma_1+\gamma_2)k_\parallel^2\end{array} & 2\sqrt{3}\gamma_3k_+k_z & -\sqrt{6}\gamma_3k_+k_z \\
\sqrt{\frac{1}{6}}iPk_+ & \begin{array}{c}\sqrt{3}\gamma_2(k_x^2-k_y^2)\\ +2\sqrt{3}i\gamma_3k_xk_y\end{array} & 0 & 3\sqrt{2}\gamma_3k_+k_z & \sqrt{\frac{2}{3}}iPk_z & 2\sqrt{3}\gamma_3k_-k_z & \begin{array}{c}-(\gamma_1+2\gamma_2)k_z^2\\ +(\gamma_2-\gamma_1)k_\parallel^2+E_v\end{array} & \begin{array}{c}2\sqrt{2}\gamma_2k_z^2\\ -\sqrt{2}\gamma_2k_\parallel^2\end{array} \\
\sqrt{\frac{1}{3}}iPk_+ & \begin{array}{c}\sqrt{6}\gamma_2(k_x^2-k_y^2)\\ +2\sqrt{6}i\gamma_3k_xk_y\end{array} & -3\sqrt{2}\gamma_3k_+k_z & 0 & -\sqrt{\frac{1}{3}}iPk_z & -\sqrt{6}\gamma_3k_-k_z & \begin{array}{c}2\sqrt{2}\gamma_2k_z^2\\ -\sqrt{2}\gamma_2k_\parallel^2\end{array} & \begin{array}{c}-\gamma_1k_z^2+E_v\\ -\gamma_1k_\parallel^2-\Delta\end{array}
\end{bmatrix}$$

Table 2: *The Hamiltonian matrix* $\boldsymbol{H}$, *of eq.(6), using the basis set in Table 1. The interactions between the eight basis states and the remote bands are included perturbatively using the standard Lowdin approach. All wavevectors are expressed in units of* $\sqrt{\frac{\hbar^2}{2m}}$.

$\gamma_1, \gamma_2 \& \gamma_3$ are the modified Luttinger parameters and are related to the parameters γ_i^L (i = 1-3) originally defined by Luttinger [7]

$$\gamma_1 = \gamma_1^L - \frac{\chi}{2} \tag{13}$$

$$\gamma_{2,3} = \gamma_{2,3}^L - \frac{\chi}{4} \tag{14}$$

where $\chi = \frac{4m P_{Kane}^2}{3\hbar^2 E_g} = \frac{2}{3}\frac{P^2}{E_g}$ is defined in terms of the bandgap $E_g = E_c - E_v$

The effective masses at the edges of the valence and conduction bands may be related to the modified Luttinger parameters by

$$\frac{m}{m_{hh}} = \gamma_1 - 2\gamma_2 \tag{15}$$

$$\frac{m}{m_c} = s + \chi\left(1 + \frac{1}{2r}\right) \tag{16}$$

$$\frac{m}{m_{lh}} = \gamma_1 + 2\gamma_2 + \chi \tag{17}$$

$$\frac{m}{m_{sso}} = \gamma_1 + \frac{\chi r}{2} \tag{18}$$

$$\frac{m}{m_{hh111}} = \gamma_1 - 2\gamma_3 \tag{19}$$

where

$$r = \frac{E_g}{\Delta + E_g} \tag{20}$$

m_{hh} = heavy hole mass in the (001) direction

m_c = conduction mass in the (001) direction

m_{lh} = light hole mass in the (001) direction

m_{sso} = spin split off mass in the (001) direction

m_{hh111} = heavy hole mass in the (111) direction

Therefore, if the five effective masses, E_g and Δ are known all the required parameters in the Hamiltonian can be calculated.

The energy eigenvalues, E, and the corresponding eigenvectors of the ***k.p*** equation (4) can now be obtained numerically for any given wavevector, ***k***. In application to quantum well problems this normally involves fixing E, k_x and k_y and solving for k_z. The Hamiltonian is written as

$$(\boldsymbol{H}_2 k_z^2 + \boldsymbol{H}_1 k_z + \boldsymbol{H}_0) \tag{21}$$

where $\boldsymbol{H}_0$, $\boldsymbol{H}_1$ and $\boldsymbol{H}_2$ are independent of k_z

The ***k.p*** equation is

$$(\boldsymbol{H}_2 k_z^2 + \boldsymbol{H}_1 k_z + (\boldsymbol{H}_0 - E))\,\boldsymbol{c} = \boldsymbol{0} \tag{22}$$

and can be turned into an eigenvalue equation for k_z by multiplying eq.(22) on the left by $-\mathrm{H}_2^{-1}$, moving the first term to the right hand side and including the trivial relation $k_z\,\boldsymbol{c} = k_z\,\boldsymbol{c}$.

$$\begin{bmatrix} 0 & 1 \\ -\boldsymbol{H}_2^{-1}(\boldsymbol{H}_0 - E) & -\boldsymbol{H}_2^{-1}\boldsymbol{H}_1 \end{bmatrix} \begin{bmatrix} \boldsymbol{c} \\ k_z \boldsymbol{c} \end{bmatrix} = k_z \begin{bmatrix} \boldsymbol{c} \\ k_z \boldsymbol{c} \end{bmatrix} \tag{23}$$

It is straightforward to show that if k_z is a solution to the above equation then so also are $-k_z$, k_z^* and $-k_z^*$ [6]. The matrix on the left hand side of eq.(23) is of order 16 and consequently 16 eigenvalues and eigenvectors can be obtained. Therefore, the general solution to eq.(23) at any particular E, k_x, k_y is of the form

$$\psi = \sum_i \sum_j A_i F_{ij}\, e^{i\boldsymbol{k}_i\cdot\boldsymbol{r}} \left|u_j\right\rangle \tag{24}$$

where the A_i are constants and the indices i and j run from 1 to 16 and 1 to 8 respectively. Examination of the bulk bandstructure shows that there are only three distinct bands in the normal sense of the word (since the conduction band is coupled to the light hole band by a band of imaginary k_z's in the forbidden bandgap for $k_x = k_y = 0$) which provide twelve k_z eigenvalues. The bulk bandstructure for GaAs, at $k_x = k_y = 0$, is shown in Figure 1. The remaining four eigenvalues of the sixteen have large imaginary k_z values for all energies and in-plane wavevectors considered (and have been discussed by a number of authors [6,9,10,11]) and have an insignificant effect on the solutions to the quantum well structure.

2.3 Strain effects

A strained epitaxial layer can be produced by growing a thin layer of a semiconductor with bulk lattice constant a_e on a thick semiconductor substrate with lattice constant a_s [12-14]. If the epilayer is grown in the z-direction then it will experience a net biaxial strain, $\varepsilon_{\|}$, in the x-y plane given by the expression

$$\varepsilon_{\|} = \varepsilon_{xx} = \varepsilon_{yy} = (a_s - a_e)/a_e \tag{25}$$

The layer will also relax in the growth direction resulting in a strain given by

$$\varepsilon_{\perp} = -\frac{2\sigma}{1-\sigma}\varepsilon_{\|} \tag{26}$$

where σ is Poisson's ratio (approximately $\frac{1}{3}$ for tetrahedral semiconductors). The energy stored per unit area, due to the strain field [15], is given by

$$E_{stored} = 2G\left(\frac{1+\sigma}{1-\sigma}\right)\varepsilon_{\|}^2 h \tag{27}$$

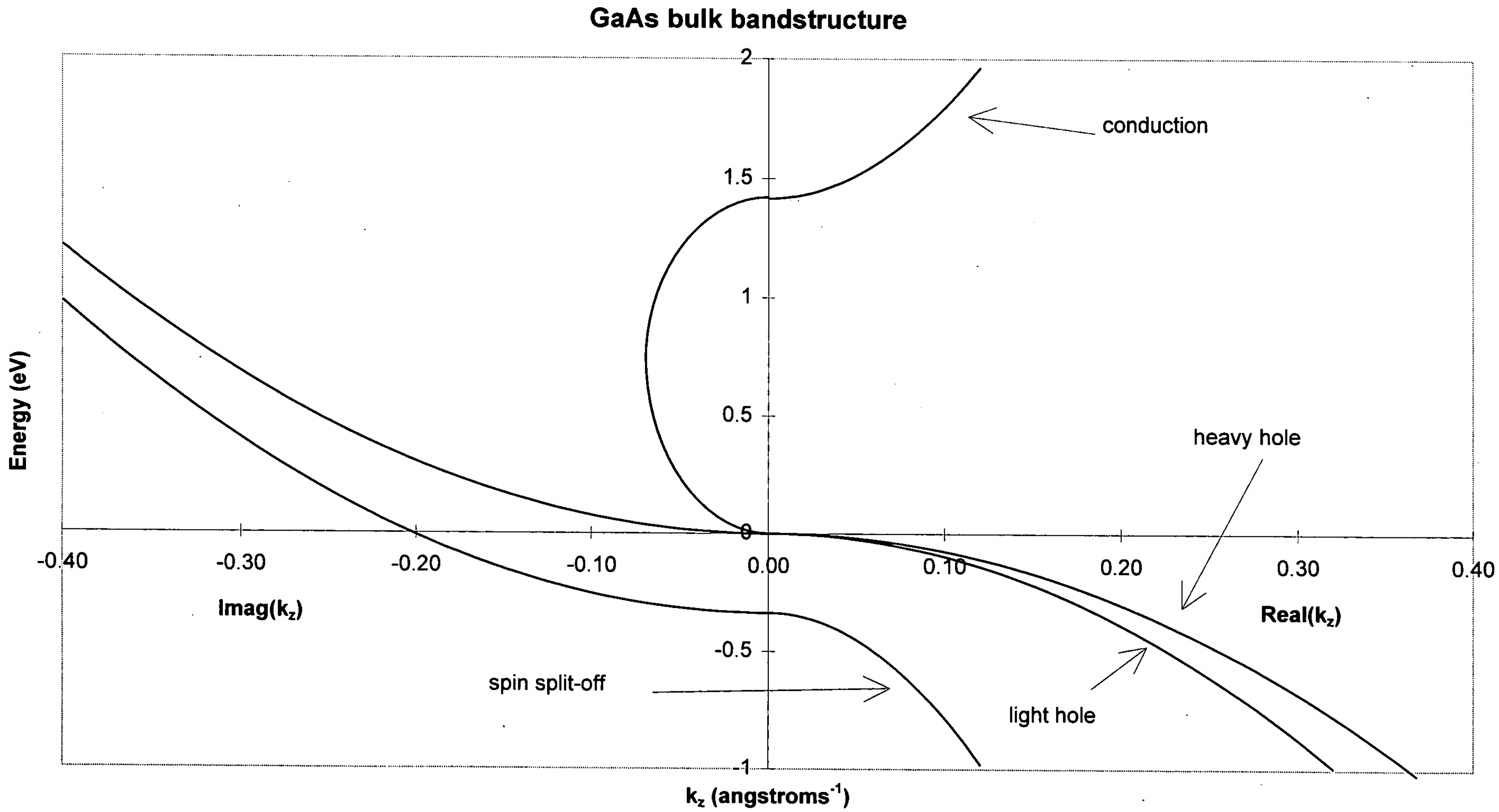

Figure 1: *The bulk complex bandstructure for GaAs at* $\boldsymbol{k_{||}=0}$, *calculated using the* ***k.p*** *method*

where,

G = shear modulus of the epilayer

h = thickness of the epilayer

At some critical thickness the energy stored per unit area will equal the energy required to form dislocations and it is energetically favourable for the structure to relieve the strain through the formation of dislocations. However, below this critical thickness the structure will normally be stable. It has been predicted by [12-14,18] that $h_c \cong 90$ angstroms for $\varepsilon_{||} = 1\%$, although the exact value depends on the material in question as well as the growth conditions [53-54]. However, it is sometimes possible to grow stable strained layers greater than the critical thickness [16], since the energy required to form a dislocation is greater than that required to propagate one that is already present. Therefore, if good quality growth can be achieved, layers with a thickness-strain product of 200 angstrom-% can be grown [17,18].

For a layer grown in the z-direction in cubic material, the strain tensor is diagonal [19-22] and is given in eq.(28) in the S, X, Y and Z basis (Note: The strain terms are small compared to the spin orbit splitting energy and the Kane momentum matrix element and therefore the same basis set, as for the unstrained material, can be retained without modification [22]).

$$\begin{bmatrix} c(\varepsilon_{xx}+\varepsilon_{yy}+\varepsilon_{zz}) & 0 & 0 & 0 \\ 0 & l\,\varepsilon_{xx}+m(\varepsilon_{yy}+\varepsilon_{zz}) & 0 & 0 \\ 0 & 0 & l\,\varepsilon_{yy}+m(\varepsilon_{xx}+\varepsilon_{zz}) & 0 \\ 0 & 0 & 0 & l\,\varepsilon_{zz}+m(\varepsilon_{xx}+\varepsilon_{yy}) \end{bmatrix} \tag{28}$$

where,

$$\varepsilon_{zz} = -2\,\frac{C_{12}}{C_{11}}\,\varepsilon_{\|} \tag{29}$$

$$\varepsilon_{\|} = \varepsilon_{xx} = \varepsilon_{yy}$$

C_{12} & C_{11} are elastic modulii of the epilayer and c, l & m are strain-dependent matrix elements which are related to the Pikus-Bir deformation potentials a_c, a_v and b_v by [19-22]

$$a_c = c = \text{conduction hydrostatic deformation potential} \tag{30}$$

$$a_v = -\frac{1}{3}(l+2m) = \text{valence hydrostatic deformation potential} \tag{31}$$

$$b_v = +\frac{1}{3}(l-m) = \text{valence shear deformation potential} \tag{32}$$

The strain dependent contribution to the Hamiltonian matrix of Table 2 (with the basis of Table 1) is straightforward to calculate and is given in eq.(33).

$$\boldsymbol{H}_{strain} = \begin{bmatrix} \boldsymbol{Z} & 0 \\ 0 & \boldsymbol{Z} \end{bmatrix}$$

where

$$\boldsymbol{Z} = \begin{bmatrix} c(\varepsilon_{xx}+\varepsilon_{yy}+\varepsilon_{zz}) & 0 & 0 & 0 \\ 0 & \begin{array}{l}\frac{1}{2}\left(\varepsilon_{xx}+\varepsilon_{yy}\right)\left(l+m\right)\\ +m\,\varepsilon_{zz}\end{array} & 0 & 0 \\ 0 & 0 & \begin{array}{l}\frac{1}{6}\left(\varepsilon_{xx}+\varepsilon_{yy}+4\,\varepsilon_{zz}\right)l\\ +\frac{1}{6}\left(5\,\varepsilon_{xx}+5\,\varepsilon_{yy}+2\,\varepsilon_{zz}\right)m\end{array} & \frac{\sqrt{2}}{6}\left(\varepsilon_{xx}+\varepsilon_{yy}-2\,\varepsilon_{zz}\right)\left(l-m\right) \\ 0 & 0 & \frac{\sqrt{2}}{6}\left(\varepsilon_{xx}+\varepsilon_{yy}-2\,\varepsilon_{zz}\right)\left(l-m\right) & \frac{1}{3}\left(\varepsilon_{xx}+\varepsilon_{yy}+\varepsilon_{zz}\right)\left(l+2m\right) \end{bmatrix} \tag{33}$$

At this point it is worth examining qualitatively the effects of the strain terms on the bulk bandstructure. When the natural lattice constant of the epilayer is larger than that of the substrate, the epilayer is under biaxial compression ($\varepsilon_{||}$ is negative and hence ε_{zz} is positive). The hydrostatic strain component, $2\varepsilon_{||}+\varepsilon_{zz}$, of the compression increases the mean bandgap, whilst the axial strain component, $\varepsilon_{zz}-\varepsilon_{||}$, splits the degeneracy of the valence band maximum, pushing the heavy hole band to higher electron energy and the light hole band to lower electron energy [15]. The heavy hole band constitutes the valence bandedge and is now heavy along the growth direction but comparatively light in the *x-y* plane. When the lattice constant of the epilayer is smaller than the substrate lattice constant, the epilayer is under biaxial tension ($\varepsilon_{||}$ is positive and ε_{zz} negative). The hydrostatic component of the tension reduces the mean bandgap, whilst the axial component splits the degeneracy of the valence band maximum, pushing the light hole band to higher electron energy and the heavy hole band to lower electron energy. The highest band is the light hole band which is light along the growth direction but comparatively heavy in the *x-y* plane [15,23].

2.4 Complex bandstructure description of the electronic states of a quantum well

A quantum well is a layer of narrow bandgap semiconductor grown between two larger bandgap semiconductors. The electronic states and bandstructure of a semiconductor quantum well may be obtained by generalising the standard text book approach to the solution of Schrodinger equation for a simple square well [55].

Consider the quantum well layer to lie in the *x-y* plane. The wave function, ψ, of any energy eigenstate of the system can be written as a linear combination of all allowed bulk states for the three materials (left barrier, well and right barrier) at the relevant energy subject to appropriate boundary conditions. The linear combination of bulk states can be written, for each material, in the form

$$\psi^M = \sum_i \sum_j A_i^M F_{ji}^M e^{i\mathbf{k}_i^M . \mathbf{r}} \left| u_j^M \right\rangle \tag{34}$$

where M = left barrier layer, well layer & right layer respectively

A_i^M = the coefficient specifying the contribution from each of the 16 bulk states (i=1-16) for a particular energy and in-plane wave vector (for each region)

F_{ji}^M = the coefficient specifying the contribution from each of the zone centre states (j=1-8) for the bulk state i (i=1-16) for a particular energy and in-plane wave vector (for each region)

$$\mathbf{k}_i^M = k_{ix}^M \, \mathbf{i} + k_{iy}^M \, \mathbf{j} + k_{iz}^M \, \mathbf{k} \tag{35}$$

where k_{ix}^M and k_{iy}^M are real, representing a point in the in-plane bandstructure. k_{iz}^M may be real, imaginary or complex; hence the term complex bandstructure. Only bound states of the well are considered here for which k_{iz}^M is either imaginary or complex in the barriers.

u_j^M = zone centre basis functions (j=1-8) (36)

Therefore, to determine ψ, we need to calculate the A_i^M using equations which follow directly from applying the required boundary conditions.

The wave function, ψ, is the solution of Schrodinger's equation for the system and must be continuous at the both interfaces (left barrier/well interface and well/right barrier interface) and must be finite everywhere. The derivative of ψ must also be continuous and finite. The wave function can only be continuous at all points on the interfaces, $\boldsymbol{r}_{||}$, if the in-plane wave vectors k_{ix}^M **i** + k_{iy}^M **j** are the same in all three materials for all i in the sum of eq.(34). The finiteness of the wave function is guaranteed by ensuring that the exponentials in the linear expansion go to zero as $|z|$ becomes very large. This is achieved by restricting the wave function expansions to the terms containing eight of the sixteen k_z's from the left barrier (the eight k_z whose imaginary value < 0) and from the right barrier (the eight k_z whose imaginary value > 0). The restriction on the expansion is made by choosing the A_i^M to be zero for the terms that are not to be included

The ***k.p*** method is formulated in terms of matrix elements and avoids the need for a knowledge of the explicit form of the wave functions of the zone centre basis states. Therefore to proceed further with the matching of wave functions at the boundaries it is necessary to assume that the zone centre Bloch states, $|u_j^M\rangle$, are the same in each of the three materials, which is normally a reasonable assumption when both well and barrier materials are isoelectronic (that is both well and barrier materials are *III-V* materials such as *GaAs*). The assumption also implies that P_{kane} has a similar value in all three regions and that this is the case for a number of materials shows this to be a good approximation. The continuity of the wave function across the interfaces together with the completeness and orthogonality of the $|u_j^M\rangle$ means that the coefficients of the Bloch states $|u_j^M\rangle$ in eq.(34), the envelope functions $\sum_i A_i^M F_{ji}^M e^{i\boldsymbol{k}_i^M.\boldsymbol{r}}$, must be continuous. This follows if we equate wave functions of the form of eq.(34) at an interface, multiply by $u_j^{M\,*}$ and integrate over the unit cell.

The Schrodinger equation for the system also requires the continuity of $\frac{\partial}{\partial z}\psi$, which implies that the normal derivatives of the envelope functions $\sum_i A_i^M F_{ji}^M e^{i\boldsymbol{k}_i^M.\boldsymbol{r}}$ on each side of an interface are continuous. However, it is not possible to use an infinite set of basis functions to solve practical problems and a different approach is necessary when a small number of basis states is used as is normally the case in ***k.p*** calculations. One way to proceed is to adapt the approach described to the case of a finite basis set. In general the interface conditions for the Schrodinger equation are derived by integrating that equation across the relevant interface. A similar procedure can be adopted with the matrix equation of the ***k.p*** method [6,24,25]. The Hamiltonian of eq.(21) can be written as

$$\boldsymbol{H} = (-\boldsymbol{H}_2 \frac{\partial^2}{\partial z^2} - i\boldsymbol{H}_1 \frac{\partial}{\partial z} + \boldsymbol{H}_0) \tag{37}$$

where k_z has been replaced with the operator $\frac{1}{i}\frac{\partial}{\partial z}$.

The terms $\boldsymbol{H}_0$, $\boldsymbol{H}_1$ and $\boldsymbol{H}_2$ are dependent on z since the parameters of the Hamiltonian including the effective masses, E_g and Δ vary with layer material. As it stands the Hamiltonian is not Hermitian and it has been common practice [6,24,25] to rewrite $\boldsymbol{H}$ in a symmetrized form which is Hermitian and results in conservation of probability current across an interface

$$H = [-\frac{\partial}{\partial z} H_2 \frac{\partial}{\partial z} - \frac{i}{2}(H_1 \frac{\partial}{\partial z} + \frac{\partial}{\partial z} H_1) + H_0] \tag{38}$$

This symmetrized form of the Hamiltonian is not unique and other forms have been examined by a number of workers [41-43]. However, it suffices for the discussion here because an unambiguous approach will be developed later in this Chapter. To obtain the interface matching condition corresponding to the Hamiltonian of eq.(38) we integrate the matrix form of the Schrodinger equation (as eq.(22) but with the symmetrized Hamiltonian of eq.(38)) an infinitesimal distance in the z-direction across the interface. If the interface is at $z = 0$ this gives

$$\int_{-\varepsilon}^{+\varepsilon} Hc\,dz = \left[\left(-H_2 \frac{\partial}{\partial z} - \frac{i}{2} H_1\right)c\right]_{-\varepsilon}^{+\varepsilon} = [Mc]_{-\varepsilon}^{+\varepsilon} = 0 \tag{39}$$

where only non vanishing terms have been retained on the right hand side of the first equation.

To obtain the allowed states of the quantum well it is necessary to write the boundary conditions explicitly in terms of the bulk states of the three layers.

Continuity of the wave function gives

at the left interface

$$\sum_{i=1}^{8} A_i^{lb} F_{ji}^{lb} e^{ik_i^{lb} z_{left}} = \sum_{i=1}^{16} A_i^{w} F_{ji}^{w} e^{ik_i^{w} z_{left}} \tag{40}$$

and at the right interface

$$\sum_{i=9}^{16} A_i^{rb} F_{ji}^{rb} e^{ik_i^{rb} z_{right}} = \sum_{i=1}^{16} A_i^{w} F_{ji}^{w} e^{ik_i^{w} z_{right}} \tag{41}$$

where the superscripts lb, w and rb denote left barrier, well and right barrier respectively. The z subscript on the wavevector has been dropped to simplify the notation. z_{left} is the position of the left barrier/well interface and z_{right} that of the right interface.

Equations (40) and (41) can be written in matrix form as

$$\boldsymbol{W}_{lb}\,\boldsymbol{L} = \boldsymbol{W}_{wl}\,\boldsymbol{W}$$

(42)

$$\boldsymbol{W}_{rb}\,\boldsymbol{R} = \boldsymbol{W}_{wr}\,\boldsymbol{W} \tag{43}$$

where $\boldsymbol{W}_{lb}(i,j) = F_{ij}^{lb}\, e^{ik_i^{lb} z_{left}}$ and $\boldsymbol{W}_{rb}\,(i,j) = F_{ij}^{rb}\, e^{ik_i^{rb} z_{right}}$ are 8x8 matrices (44)

$\boldsymbol{W}_{wl}(i,j) = F_{ij}^{w}\, e^{ik_i^{w} z_{left}}$ and $\boldsymbol{W}_{wr}(i,j) = F_{ij}^{w}\, e^{ik_i^{w} z_{right}}$ are 8x16 matrices (45)

$\boldsymbol{L}\,(i) = A_i^{lb}$ and $\boldsymbol{R}\,(i) = A_i^{rb}$ are eight dimensional column vectors (46)

and $\boldsymbol{W}\,(i) = A_i^{w}$ is a sixteen dimensional column vector (47)

The matrix equations (42) and (43) can be combined to give

$$\begin{bmatrix} \boldsymbol{W}_{lb} & 0 \\ 0 & \boldsymbol{W}_{rb} \end{bmatrix} \boldsymbol{B} = \begin{bmatrix} \boldsymbol{W}_{wl} \\ \boldsymbol{W}_{wr} \end{bmatrix} \boldsymbol{W} \tag{48}$$

where $\boldsymbol{B} = \begin{bmatrix} \boldsymbol{L} \\ \boldsymbol{R} \end{bmatrix}$

or,

$$\boldsymbol{W}_{barr}\,\boldsymbol{B} = \boldsymbol{W}_{well}\,\boldsymbol{W} \tag{49}$$

The boundary condition eq.(39) gives at the left interface

$$\sum_{i=1}^{8} A_i^{lb} \sum_{m=1}^{8} M_{jm}^{lb}\; F_{mi}^{lb}\; e^{ik_i^{lb} z_{left}} = \sum_{i=1}^{16} A_i^{w} \sum_{m=1}^{8} M_{jm}^{w}\; F_{mi}^{w}\; e^{ik_i^{w} z_{left}} \tag{50}$$

and at the right interface

$$\sum_{i=1}^{8} A_i^{rb} \sum_{m=1}^{8} M_{jm}^{rb}\; F_{mi}^{rb}\; e^{ik_i^{rb} z_{right}} = \sum_{i=1}^{16} A_i^{w} \sum_{m=1}^{8} M_{jm}^{w}\; F_{mi}^{w}\; e^{ik_i^{w} z_{right}} \tag{51}$$

where $M_{jm}{}^{R}$ = component (j,m) of the integrated Hamiltonian, $\boldsymbol{M}$, of eq.(39) for region R

$k_i{}^R$ = the wavevector k_z for the bulk state i (i=1-16) at a particular energy and in-plane wavevector for region R

In matrix form, eqs.(50) and (51) are

$$\boldsymbol{D}_{lb}\,\boldsymbol{L} = \boldsymbol{D}_{wl}\,\boldsymbol{W} \tag{52}$$

$$\boldsymbol{D}_{rb}\,\boldsymbol{R} = \boldsymbol{D}_{wr}\,\boldsymbol{W} \tag{53}$$

which can be combined to give,

$$\begin{bmatrix} \boldsymbol{D}_{lb} & 0 \\ 0 & \boldsymbol{D}_{rb} \end{bmatrix} \boldsymbol{B} = \begin{bmatrix} \boldsymbol{D}_{wl} \\ \boldsymbol{D}_{wr} \end{bmatrix} \boldsymbol{W} \tag{54}$$

or,

$$\boldsymbol{D}_{barr}\,\boldsymbol{B} = \boldsymbol{D}_{well}\,\boldsymbol{W} \tag{55}$$

The two boundary conditions, equations (49) and (55), can now be combined to give

$$\boldsymbol{W}_{well}{}^{-1}\,\boldsymbol{W}_{barr}\,\boldsymbol{D}_{barr}{}^{-1}\,\boldsymbol{D}_{well}\,\boldsymbol{W} = \boldsymbol{W} \tag{56}$$

or,

$$(\boldsymbol{W}_{well}{}^{-1}\,\boldsymbol{W}_{barr}\,\boldsymbol{D}_{barr}{}^{-1}\,\boldsymbol{D}_{well} - \boldsymbol{I})\boldsymbol{W} = \boldsymbol{0} \tag{57}$$

where $\boldsymbol{I}$ is the identity matrix and $\boldsymbol{0}$ is the zero column vector.

Therefore, the quantum well states can be found by searching for the energies for which the determinant of the matrix $(\boldsymbol{W}_{well}{}^{-1}\,\boldsymbol{W}_{barr}\,\boldsymbol{D}_{barr}{}^{-1}\,\boldsymbol{D}_{well} - \boldsymbol{I})$ vanishes. For such an energy the column vectors $\boldsymbol{W}$ and $\boldsymbol{B}$, the wave function coefficients, can be calculated from eqs.(56) and (55) respectively, and completely specify the wave function for the particular energy and in-plane wavevector.

2.5 Burt envelope function theory

The theory of the electronic states of quantum wells described above is unsatisfactory in at least two respects. First, it is necessary to assume that the basis functions of the ***k.p*** Hamiltonian are the same in the well and the barriers despite the fact that the theory starts with the implicit assumption that they are different. Second, the Hamiltonian is "symmetrized" during the analysis without any fundamental justification. Burt [31-37] has shown how these problems can be avoided by using a single Schrodinger equation for the whole system and using that to derive equations which describe the wave functions at discontinuities in system properties which are designed to represent interfaces.

To outline Burt's approach we follow the salient points in reference [34] and consider a one-dimensional semiconductor structure. This could be a simple bulk crystal or a lattice matched heterostructure. The electronic wave functions can be expanded in the form,

$$\psi = \sum_j F_j \left| u_j \right\rangle \tag{58}$$

where u_j are a complete set of linearly independent periodic functions with period equal to the lattice periodicity. A natural choice in a bulk crystal would be the Bloch periodic parts at the zone centre. In a heterostructure the crucial point to note is that, whatever the choice of u_j, the same functions are used throughout the system. The F_n's, the envelope functions, are functions of electron coordinate and can be expanded in terms of plane waves, with the wavevectors in question being restricted to the first Brillouin zone. The expansion in eq.(58) is complete and unique. Substitution of eq.(58) into the Schrodinger equation gives after some algebra

$$-\frac{\hbar^2}{2m}\frac{d^2}{dz^2}F_n - i\frac{\hbar}{m}\sum_m p_{nm}\frac{d}{dz}F_m + \sum_m\int_L H_{nm}(z,z')F_m(z')dz' = EF_n(z) \qquad (59)$$

where,

$$H_{nm}(z,z') = T_{nm}\Delta(z-z') + V_{nm}(z,z') \qquad (60)$$

$$\Delta(z-z') = \frac{1}{a}\sum_k e^{ik(z-z')} \qquad (61)$$

$$T_{nm} = \frac{1}{a}\int u_n^* T u_m dz \qquad (62)$$

$$V_{nm} = \frac{1}{a}\int u_n^* V u_m dz \qquad (63)$$

$$p_{nm} = \frac{1}{a}\int u_n^* p_z u_m dz \qquad (64)$$

where T, V and p are respectively the kinetic energy, the potential energy and the momentum operators, a is the periodicity of the lattice and L the length of the structure. Away from interfaces $H_{nm}(z,z') = (T_{nm} + V_{nm})\Delta(z-z') = H_{nm}\Delta(z-z')$.

For the case of the bulk crystal or well away from interfaces in a heterostructure eq.(59) becomes

$$-\frac{\hbar^2}{2m}\frac{d^2}{dz^2}F_n - \mathrm{i}\frac{\hbar}{m}\sum_m p_{nm}\frac{d}{dz}F_m + \sum_m H_{nm}F_m = EF_n \qquad (65)$$

When the microscopic potential changes abruptly at interfaces and there are no built-in or external fields eq.(65) can be used as the basis of a ***k.p*** theory of heterostructures. On each side of the interface solutions are found to eq.(65) in the form $\sum_n f_n u_n$ and then matched at the interface. The matching conditions have to be obtained from eq.(59) which in contrast to eq.(65) is valid throughout the structure, including the interfaces. Nevertheless Burt shows that when the envelope functions are slowly varying and the crystal potential $V(z)$ is local, the last term on the left hand side of eq.(59) is well approximated by the value of H_{nm} for the material at position z, which we call $H_{nm}(z)$.

Choosing u_n to be the zone centre eigenfunctions so that the crystal Hamiltonian in that basis is diagonal with elements E_n, eq.(65) becomes

$$-\frac{\hbar^2}{2m}\frac{d^2}{dz^2}F_n - i\frac{\hbar}{m}\sum_m p_{nm}\frac{d}{dz}F_m + E_nF_n = EF_n \qquad (66)$$

Seeking solutions of the form

$$F_n = A_n\,e^{ikz} \qquad (67)$$

gives the same equation as ***k.p*** theory:

$$\sum_m\left[\left(E_n + \frac{\hbar^2k^2}{2m} - E\right)\delta_{nm} + \frac{\hbar k}{m}p_{nm}\right]A_m = 0 \qquad (68)$$

In the three dimensional case eq.(66) becomes [35]

$$-\frac{\hbar^2}{2m}\nabla^2 F_n(\boldsymbol{r}) - i\frac{\hbar}{m}\sum_m \boldsymbol{p}_{nm}\cdot\nabla F_m(\boldsymbol{r}) + \sum_m H_{nm}F_m(\boldsymbol{r}) = EF_n \qquad (69)$$

with the obvious generalisation of eq.(65).

As in the conventional ***k.p*** theory the terms j in the sum of eq.(58) may be divided into two groups s and r, where the group s provide the dominant contributions and r the much smaller contributions corresponding to remote bands. The terms in the r group can be eliminated in favour of those in s by considering eq.(69) for $n = r$ and $m = s$ and ignoring the second derivative of the slowly varying $F_r(\boldsymbol{r})$:

$$F_r = (E-H_{rr})^{-1}\sum_{s'}\left(\frac{-i\hbar}{m}\,\boldsymbol{p}_{rs'}\cdot\nabla F_{s'} + H_{rs'}F_{s'}\right) \tag{70}$$

Substitution of the expression for F_r into eq.(69) yields

$$\begin{aligned}
&\frac{-\hbar^2}{2m}\sum_{s'}\nabla\cdot[\gamma^{(r)}_{ss'}\cdot\nabla F_{s'}(\boldsymbol{r})] + \sum_{s'}\frac{-i\hbar}{m}\,\boldsymbol{p}_{ss'}\cdot\nabla F_{s'}(\boldsymbol{r}) \\
&+ \sum_{s'} H^{(2)}_{ss'}(E,\boldsymbol{r})\,F_{s'}(\boldsymbol{r}) + \sum_{s',r}\frac{-i\hbar}{m}\,\boldsymbol{p}_{sr}\cdot\nabla[(E-H_{rr})^{-1}H_{rs'}]\,F_{s'}(\boldsymbol{r}) \\
&+ \sum_{s',r}\frac{-i\hbar}{m}(E-H_{rr})^{-1}(\boldsymbol{p}_{sr}H_{rs'} + H_{sr}\boldsymbol{p}_{rs'})\cdot\nabla F_{s'}(\boldsymbol{r}) = EF_s(\boldsymbol{r})
\end{aligned} \tag{71}$$

where,

$$\gamma^{(r)}_{ss'}(E,\boldsymbol{r}) = \boldsymbol{I}\delta_{ss'} + \frac{2}{m}\sum_r \boldsymbol{p}_{sr}[E-H_{rr}(\boldsymbol{r})]^{-1}\,\boldsymbol{p}_{rs'} \tag{72}$$

$$H^{(2)}_{ss'}(E;\boldsymbol{r}) = H_{ss'}(\boldsymbol{r}) + \sum_r H_{sr}(\boldsymbol{r})[E-H_{rr}(\boldsymbol{r})]^{-1}\,H_{rs'}(\boldsymbol{r}) \tag{73}$$

The fourth term on the left hand side of eq.(71) vanishes for the bulk case since H_{rr} and $H_{rs'}$ are constant. To provide a suitable description of the states around the fundamental gap it is appropriate to use the states of Table 1 in group s and place all other states in group r. It is a good approximation to neglect the terms in eq.(71) involving H_{sr} since this matrix element is only an appreciable size when s and r have the same symmetry but such states are usually well separated in energy. Making this approximation eq. (71) reduces to

$$\begin{aligned}
&\frac{-\hbar^2}{2m}\sum_{s'}\nabla\cdot[\gamma^{(r)}_{ss'}\cdot\nabla F_{s'}(\boldsymbol{r})] + \sum_{s'}\frac{-i\hbar}{m}\,\boldsymbol{p}_{ss'}\cdot\nabla F_{s'}(\boldsymbol{r}) \\
&+ \sum_{s'} H_{ss'}(R)\,F_{s'}(\boldsymbol{r}) = \mathrm{E}F_s(\boldsymbol{r})
\end{aligned} \tag{74}$$

The equation may be written in the matrix form

$$\tilde{H}_{ss'}\,F_{s'}(\boldsymbol{r}) = E\,F_s(\boldsymbol{r}) \tag{75}$$

The Hamiltonian, in the *S, X, Y* and *Z* basis, without spin is shown in Table 3 where

$$\sigma = \left(\frac{1}{3m}\right)\sum_{j}^{\Gamma_1}\frac{\left|\langle x|p_x|u_j\rangle\right|^2}{E_j - E_v} \tag{76}$$

$$\pi = \left(\frac{1}{3m}\right)\sum_{j}^{\Gamma_{15}}\frac{\left|\langle x|p_y|u_j\rangle\right|^2}{E_j - E_v} \tag{77}$$

$$\delta = \left(\frac{1}{6m}\right)\sum_{j}^{\Gamma_{12}}\frac{\left|\langle x|p_x|u_j\rangle\right|^2}{E_j - E_v} \tag{78}$$

$$\omega = \left(\frac{1}{3m}\right)\sum_{j}^{\Gamma_{15}}\frac{\langle s|p_z|u_j\rangle\langle u_j|p_y|x\rangle}{E_j - \frac{1}{2}(E_s - E_v)} \tag{79}$$

$$\lambda = \left(\frac{1}{3m}\right)\sum_{j}^{\Gamma_{15}}\frac{\left|\langle s|p_x|u_j\rangle\right|^2}{E_j - E_s} \tag{80}$$

The dimensionless quantities π and δ are the same as those defined by Foreman [38]. Foreman treats the conduction band as a remote band and therefore includes it in the summation which defines σ. However, the conduction band is treated explicitly here and does not appear in the summation of eq.(76).

It is instructive to compare the Hamiltonian of Table 3 to the one derived by Kane [1,2] which is shown in Table 4, where

$$M = \frac{-3\hbar^2}{m^2}\pi \tag{81}$$

$$L^{\prime} = \frac{-3\hbar^2}{m^2}(\sigma+2\delta) \tag{82}$$

$$N^{\prime} = \frac{-3\hbar^2}{m^2}(\sigma-\delta+\pi) \tag{83}$$

$$
\begin{bmatrix}
\begin{array}{c:c:c:c}
\begin{gathered}(1-6\lambda)k_{\parallel}^{2}+\\ k_z(1-6\lambda)k_z+E_c\end{gathered} & \begin{gathered}iPk_x-6k_zwk_y\\ -6wk_zk_y\end{gathered} & \begin{gathered}iPk_y-6k_zwk_x\\ -6wk_xk_z\end{gathered} & iPk_z-12wk_xk_y \\ \hdashline
\begin{gathered}-iPk_x-6k_zwk_y\\ -6wk_yk_z\end{gathered} & \begin{gathered}k_{\parallel}^{2}-6\sigma k_x^2-6\pi k_y^2\\ +k_z(1-6\pi)k_z-12\delta k_x^2\\ +E_v\end{gathered} & \begin{gathered}-6\sigma k_xk_y-6\pi k_yk_x\\ +6\delta k_xk_y\end{gathered} & \begin{gathered}-6\sigma k_xk_z-6k_z\pi k_x\\ +6\delta k_xk_z\end{gathered} \\ \hdashline
\begin{gathered}-iPk_y-6k_zwk_x\\ -6wk_xk_z\end{gathered} & \begin{gathered}-6\sigma k_yk_x-6\pi k_xk_y\\ +6\delta k_yk_x\end{gathered} & \begin{gathered}-6\sigma k_y^2-6\pi k_x^2-12\delta k_y^2\\ k_{\parallel}^{2}+k_z(1-6\pi)k_z+E_v\end{gathered} & \begin{gathered}-6\sigma k_yk_z+6\delta k_yk_z\\ -6k_z\pi k_y\end{gathered} \\ \hdashline
-iPk_z-12wk_xk_y & \begin{gathered}-6k_z\sigma k_x-6\pi k_xk_z\\ +6k_z\delta k_x\end{gathered} & \begin{gathered}-6k_z\sigma k_y-6\pi k_yk_z\\ +6k_z\delta k_y\end{gathered} & \begin{gathered}(1-6\pi)k_{\parallel}^{2}+E_v\\ -k_z(6\sigma+12\delta-1)k_z\end{gathered}
\end{array}
\end{bmatrix}
$$

Table 3: *The Hamiltonian matrix, calculated from Burt envelope function theory eq.(74), in the S, X, Y & Z basis set (no spin). The interactions between the four basis states and the remote bands are included perturbatively using the standard Lowdin approach. All wavevectors are expressed in units of* $\sqrt{\frac{\hbar^2}{2m}}$.

$$
\left[\begin{array}{c:c:c:c}
\begin{array}{l}(1-6\lambda)\,k_{\parallel}^{2}+\\(1-6\lambda)\,k_{z}^{2}+E_{c}\end{array} & iP\,k_{x}-12w\,k_{y}k_{z} & iP\,k_{y}-12w\,k_{x}k_{z} & iP\,k_{z}-12w\,k_{x}k_{y} \\ \hdashline
-iP\,k_{x}-12w\,k_{y}k_{z} & \begin{array}{l}k_{\parallel}^{2}-6\sigma\,k_{x}^{2}-6\pi\,k_{y}^{2}\\+(1-6\pi)\,k_{z}^{2}-12\delta\,k_{x}^{2}\\+E_{v}\end{array} & \begin{array}{l}-6\sigma\,k_{x}k_{y}-6\pi\,k_{x}k_{y}\\+6\delta\,k_{x}k_{y}\end{array} & \begin{array}{l}-6\sigma\,k_{x}k_{z}-6\pi\,k_{x}k_{z}\\+6\delta\,k_{x}k_{z}\end{array} \\ \hdashline
-iP\,k_{y}-12w\,k_{x}k_{z} & \begin{array}{l}-6\sigma\,k_{x}k_{y}-6\pi\,k_{x}k_{y}\\+6\delta\,k_{x}k_{y}\end{array} & \begin{array}{l}-6\sigma\,k_{y}^{2}-6\pi\,k_{x}^{2}-12\delta\,k_{y}^{2}\\k_{\parallel}^{2}+(1-6\pi)\,k_{z}^{2}+E_{v}\end{array} & \begin{array}{l}-6\sigma\,k_{y}k_{z}+6\delta\,k_{y}k_{z}\\-6\pi\,k_{y}k_{z}\end{array} \\ \hdashline
-iP\,k_{z}-12w\,k_{x}k_{y} & \begin{array}{l}-6\sigma\,k_{x}k_{z}-6\pi\,k_{x}k_{z}\\+6\delta\,k_{x}k_{z}\end{array} & \begin{array}{l}-6\sigma\,k_{y}k_{z}-6\pi\,k_{y}k_{z}\\+6\delta\,k_{y}k_{z}\end{array} & \begin{array}{l}(1-6\pi)\,k_{\parallel}^{2}+E_{v}\\-(6\sigma+12\delta-1)\,k_{z}^{2}\end{array}
\end{array}\right]
$$

Table 4: *The Kane Hamiltonian matrix in the S, X, Y & Z basis set (no spin). The interactions between the four basis states and the remote bands are included perturbatively using the standard Lowdin approach. All wavevectors are expressed in units of* $\sqrt{\frac{\hbar^2}{2m}}$.

$$B = \frac{-6\hbar^2}{m^2}\omega \qquad (84)$$

$$A` = \frac{-3\hbar^2}{m}\lambda \qquad (85)$$

The difference between the matrices is the ordering of k_x, k_y and k_z which is important in inhomogeneous systems and when the components of wavevector are replaced by differential operators. However, in a homogeneous system where σ, δ, π, ω and λ are independent of position the two Hamiltonians are identical.

The Hamiltonian in the angular momentum basis set (Table 1) with spin included is shown in Table 5. The linear splitting terms due to inversion asymmetry of the zincblende structure, ω, have now been dropped, which is equivalent to the common approximation $B = 0$ in ***k.p*** theory. The Kane (Table 2) and Burt (Table 5) Hamiltonians can be compared directly using the fact that the modified Luttinger parameters are related to σ, δ and π by,

$$\gamma_1 = -1+2\sigma+4\delta+4\pi \qquad (86)$$

$$\gamma_2 = \sigma+2\delta-\pi \qquad (87)$$

$$\gamma_3 = \sigma-\delta+\pi \qquad (88)$$

If we consider σ, δ and π to vary with z and k_z to be replaced by $-i\frac{\partial}{\partial z}$ a particular difference between the two Hamiltonians arises. In Burt's version the opposite spin light hole states couple as do the spin split off states but in the Kane matrix the elements representing this coupling vanish.

$$\begin{bmatrix}
\begin{matrix}(1-6\lambda)k_\parallel^2+E_c\\+k_z(1-6\lambda)k_z\end{matrix} & \sqrt{\frac{1}{2}}iPk_+ & -\sqrt{\frac{2}{3}}iPk_z & \sqrt{\frac{1}{3}}iPk_z & 0 & 0 & -\sqrt{\frac{1}{6}}iPk_- & -\sqrt{\frac{1}{3}}iPk_- \\
-\sqrt{\frac{1}{2}}iPk_- & \begin{matrix}(1-3\sigma-3\pi-6\delta)k_\parallel^2\\+k_z(1-6\pi)k_z+E_v\end{matrix} & \begin{matrix}2\sqrt{3}[\sigma k_-k_z+\\k_-k_z\pi-\delta k_-k_z]\end{matrix} & \begin{matrix}-\sqrt{6}[\sigma k_-k_z+\\k_-k_z\pi-\delta k_-k_z]\end{matrix} & 0 & 0 & \begin{matrix}\sqrt{3}[(\sigma+2\delta-\pi)\\(k_x^2-k_y^2)\\+2i(\delta-\sigma-\pi)k_xk_y]\end{matrix} & \begin{matrix}\sqrt{6}[(\sigma+2\delta-\pi)\\(k_x^2-k_y^2)\\+2i(\delta-\sigma-\pi)k_xk_y]\end{matrix} \\
\sqrt{\frac{2}{3}}iPk_z & \begin{matrix}2\sqrt{3}[k_+k_z\sigma+\\k_+\pi k_z-k_+k_z\delta]\end{matrix} & \begin{matrix}(1-\sigma-5\pi-2\delta)k_\parallel^2+E_v+\\k_z(1-4\sigma-2\pi-8\delta)k_z\end{matrix} & \begin{matrix}\sqrt{2}[2k_z(\sigma+2\delta-\pi)k_z\\-(\sigma+2\delta-\pi)k_\parallel^2]\end{matrix} & -\sqrt{\frac{1}{6}}iPk_- & \begin{matrix}-\sqrt{3}[(\sigma+2\delta-\pi)\\(k_x^2-k_y^2)\\-2i(\sigma-\delta+\pi)k_xk_y]\end{matrix} & \begin{matrix}k_-[k_z(\delta+\pi-\sigma)\\+(\sigma-\delta-\pi)k_z]\end{matrix} & \begin{matrix}-\sqrt{2}k_-[(\sigma-\delta+2\pi)k_z\\+k_z(\pi+2\sigma-2\delta)]\end{matrix} \\
-\sqrt{\frac{1}{3}}iPk_z & \begin{matrix}-\sqrt{6}[k_+k_z\sigma-k_+k_z\delta\\+k_+\pi k_z]\end{matrix} & \begin{matrix}\sqrt{2}[-(\sigma+2\delta-\pi)k_\parallel^2\\+2k_z(\sigma+2\delta-\pi)k_z]\end{matrix} & \begin{matrix}(1-2\sigma-4\pi-4\delta)k_\parallel^2-\Delta\\+k_z(1-2\sigma-4\delta-4\pi)k_z\\+E_v\end{matrix} & -\sqrt{\frac{1}{3}}iPk_- & \begin{matrix}-\sqrt{6}[(\sigma+2\delta-\pi)(k_x^2-k_y^2)\\-2i(\sigma-\delta+\pi)k_xk_y]\end{matrix} & \begin{matrix}\sqrt{2}k_-[(\sigma-\delta+2\pi)k_z\\+k_z(2\sigma-2\delta+\pi)]\end{matrix} & \begin{matrix}-2k_-[(\sigma-\delta-\pi)k_z\\+k_z(\delta+\pi-\sigma)]\end{matrix} \\
0 & 0 & \sqrt{\frac{1}{6}}iPk_+ & \sqrt{\frac{1}{3}}iPk_+ & \begin{matrix}(1-6\lambda)k_\parallel^2+E_c\\+k_z(1-6\lambda)k_z\end{matrix} & \sqrt{\frac{1}{2}}iPk_- & -\sqrt{\frac{2}{3}}iPk_z & \sqrt{\frac{1}{3}}iPk_z \\
0 & 0 & \begin{matrix}-\sqrt{3}[(\sigma+2\delta-\pi)(k_x^2-k_y^2)\\+2i(\sigma-\delta+\pi)k_xk_y]\end{matrix} & \begin{matrix}-\sqrt{6}[(\sigma+2\delta-\pi)(k_x^2-k_y^2)\\+2i(\sigma-\delta+\pi)k_xk_y]\end{matrix} & -\sqrt{\frac{1}{2}}iPk_+ & \begin{matrix}(1-3\sigma-6\delta-3\pi)k_\parallel^2\\+k_z(1-6\pi)k_z+E_v\end{matrix} & \begin{matrix}2\sqrt{3}k_+[(\sigma-\delta)k_z\\+k_z\pi]\end{matrix} & \begin{matrix}-\sqrt{6}k_+[(\sigma-\delta)k_z\\+k_z\pi]\end{matrix} \\
\sqrt{\frac{1}{6}}iPk_+ & \begin{matrix}\sqrt{3}[(\sigma+2\delta-\pi)(k_x^2-k_y^2)\\-2i(-\sigma+\delta-\pi)k_xk_y]\end{matrix} & \begin{matrix}k_+[(\delta+\pi-\sigma)k_z\\+k_z(\sigma-\delta-\pi)]\end{matrix} & \begin{matrix}\sqrt{2}k_+[k_z(\sigma-\delta+2\pi)\\+(\pi-2\delta+2\sigma)k_z]\end{matrix} & \sqrt{\frac{2}{3}}iPk_z & \begin{matrix}2\sqrt{3}k_-[k_z(\sigma-\delta)\\+\pi k_z]\end{matrix} & \begin{matrix}(1-\sigma-5\pi-2\delta)k_\parallel^2+E_v\\k_z(1-4\sigma-2\pi-8\delta)k_z\end{matrix} & \begin{matrix}-\sqrt{2}[(\sigma+2\delta-\pi)k_\parallel^2\\-2k_z(\sigma-\pi+2\delta)k_z]\end{matrix} \\
\sqrt{\frac{1}{3}}iPk_+ & \begin{matrix}\sqrt{6}[(\sigma+2\delta-\pi)(k_x^2-k_y^2)\\-2i(-\sigma+\delta-\pi)k_xk_y]\end{matrix} & \begin{matrix}-\sqrt{2}k_+[k_z(\sigma-\delta+2\pi)\\+(\pi+2\sigma-2\delta)k_z]\end{matrix} & \begin{matrix}-2k_+[k_z(\sigma-\delta-\pi)\\+(\delta+\pi-\sigma)k_z]\end{matrix} & -\sqrt{\frac{1}{3}}iPk_z & \begin{matrix}-\sqrt{6}k_-[k_z(\sigma-\delta)\\+\pi k_z]\end{matrix} & \begin{matrix}-\sqrt{2}[(\sigma+2\delta-\pi)k_\parallel^2\\-2k_z(\sigma+2\delta-\pi)k_z]\end{matrix} & \begin{matrix}(1-2\sigma-4\pi-4\delta)k_\parallel^2-\Delta\\+k_z(1-2\sigma-4\delta-4\pi)k_z\\+E_v\end{matrix}
\end{bmatrix}$$

Table 5: *The Hamiltonian matrix, calculated from Burt envelope function theory eq.(74), using the basis set in Table 1. The interactions between the eight basis states and the remote bands are included perturbatively using the standard Lowdin approach. All wavevectors are expressed in units of* $\sqrt{\frac{\hbar^2}{2m}}$.

$$\begin{bmatrix}
-\frac{\hbar^2}{2m}s\frac{\partial}{\partial z} & 0 & -\sqrt{\frac{\hbar^2}{2m}}\sqrt{\frac{1}{6}}P & \sqrt{\frac{\hbar^2}{2m}}\frac{1}{2\sqrt{3}}P & 0 & 0 & 0 & 0 \\
0 & -\frac{\hbar^2}{2m}(2\gamma_2-\gamma_1)\frac{\partial}{\partial z} & -\sqrt{\frac{\hbar^2}{2m}}\sqrt{3}i\gamma_3 k_- & \sqrt{\frac{\hbar^2}{2m}}\sqrt{\frac{3}{2}}i\gamma_3 k_- & 0 & 0 & 0 & 0 \\
\sqrt{\frac{\hbar^2}{2m}}\sqrt{\frac{1}{6}}P & -\sqrt{\frac{\hbar^2}{2m}}\sqrt{3}i\gamma_3 k_+ & \frac{\hbar^2}{2m}(\gamma_1+2\gamma_2)\frac{\partial}{\partial z} & -\frac{\hbar^2}{2m}2\sqrt{2}\gamma_2\frac{\partial}{\partial z} & 0 & 0 & 0 & \sqrt{\frac{\hbar^2}{2m}}\frac{3}{\sqrt{2}}i\gamma_3 k_- \\
-\sqrt{\frac{\hbar^2}{2m}}\frac{1}{2\sqrt{3}}P & \sqrt{\frac{\hbar^2}{2m}}\sqrt{\frac{3}{2}}i\gamma_3 k_+ & -\frac{\hbar^2}{2m}2\sqrt{2}\gamma_2\frac{\partial}{\partial z} & \frac{\hbar^2}{2m}\gamma_1\frac{\partial}{\partial z} & 0 & 0 & -\sqrt{\frac{\hbar^2}{2m}}\frac{3}{\sqrt{2}}i\gamma_3 k_- & 0 \\
0 & 0 & 0 & 0 & -\frac{\hbar^2}{2m}s\frac{\partial}{\partial z} & 0 & -\sqrt{\frac{\hbar^2}{2m}}\sqrt{\frac{1}{6}}P & \sqrt{\frac{\hbar^2}{2m}}\frac{1}{2\sqrt{3}}P \\
0 & 0 & 0 & 0 & 0 & -\frac{\hbar^2}{2m}(2\gamma_2-\gamma_1)\frac{\partial}{\partial z} & -\sqrt{\frac{\hbar^2}{2m}}\sqrt{3}i\gamma_3 k_+ & \sqrt{\frac{\hbar^2}{2m}}\sqrt{\frac{3}{2}}i\gamma_3 k_+ \\
0 & 0 & 0 & -\sqrt{\frac{\hbar^2}{2m}}\frac{3}{\sqrt{2}}i\gamma_3 k_+ & \sqrt{\frac{\hbar^2}{2m}}\sqrt{\frac{1}{6}}P & -\sqrt{\frac{\hbar^2}{2m}}\sqrt{3}i\gamma_3 k_- & \frac{\hbar^2}{2m}(\gamma_1+2\gamma_2)\frac{\partial}{\partial z} & -\frac{\hbar^2}{2m}2\sqrt{2}\gamma_2\frac{\partial}{\partial z} \\
0 & 0 & \sqrt{\frac{\hbar^2}{2m}}\frac{3}{\sqrt{2}}i\gamma_3 k_+ & 0 & -\sqrt{\frac{\hbar^2}{2m}}\frac{1}{2\sqrt{3}}P & \sqrt{\frac{\hbar^2}{2m}}\sqrt{\frac{3}{2}}i\gamma_3 k_- & -\frac{\hbar^2}{2m}2\sqrt{2}\gamma_2\frac{\partial}{\partial z} & \frac{\hbar^2}{2m}\gamma_1\frac{\partial}{\partial z}
\end{bmatrix}$$

Table 6: *The Hamiltonian matrix of Table 2 which has been symmetrized using eqs.(37-38) and integrated an infinitesimal distance across an interface in the z direction. All wavevectors are expressed in units of* $\sqrt{\frac{\hbar^2}{2m}}$.

$$\begin{bmatrix}
-\frac{\hbar^2}{2m}s\frac{\partial}{\partial z} & 0 & 0 & 0 & 0 & 0 & 0 & 0 \\
0 & -\frac{\hbar^2}{2m}(2\gamma_2-\gamma_1)\frac{\partial}{\partial z} & -\sqrt{\frac{\hbar^2}{2m}}\frac{1}{\sqrt{3}}i(1+\gamma_1-2\gamma_2)k_- & \sqrt{\frac{\hbar^2}{2m}}\frac{1}{\sqrt{6}}i(1+\gamma_1-2\gamma_2)k_- & 0 & 0 & 0 & 0 \\
0 & \sqrt{\frac{\hbar^2}{2m}}\frac{1}{\sqrt{3}}i\,(1+\gamma_1-2\gamma_2-6\gamma_3)k_+ & \frac{\hbar^2}{2m}(\gamma_1+2\gamma_2)\frac{\partial}{\partial z} & -\frac{\hbar^2}{2m}2\sqrt{2}\gamma_2\frac{\partial}{\partial z} & 0 & 0 & -\sqrt{\frac{\hbar^2}{2m}}\frac{1}{3}i\,(1+\gamma_1-2\gamma_2-3\gamma_3)k_- & -\sqrt{\frac{\hbar^2}{2m}}\frac{1}{\sqrt{3}}i\,(1+\gamma_1-2\gamma_2-12\gamma_3)k_- \\
0 & -\sqrt{\frac{\hbar^2}{2m}}\frac{1}{\sqrt{6}}i\,(1+\gamma_1-2\gamma_2-6\gamma_3)k_+ & -\frac{\hbar^2}{2m}2\sqrt{2}\gamma_2\frac{\partial}{\partial z} & \frac{\hbar^2}{2m}\gamma_1\frac{\partial}{\partial z} & 0 & 0 & \sqrt{\frac{\hbar^2}{2m}}\frac{1}{3\sqrt{2}}i\,(1+\gamma_1-2\gamma_2-12\gamma_3)k_- & \sqrt{\frac{\hbar^2}{2m}}\frac{2}{3}i\,(1+\gamma_1-2\gamma_2-3\gamma_3)k_- \\
0 & 0 & 0 & 0 & -\frac{\hbar^2}{2m}s\frac{\partial}{\partial z} & 0 & 0 & 0 \\
0 & 0 & 0 & 0 & 0 & -\frac{\hbar^2}{2m}(2\gamma_2-\gamma_1)\frac{\partial}{\partial z} & -\sqrt{\frac{\hbar^2}{2m}}\frac{1}{\sqrt{3}}i\,(1+\gamma_1-2\gamma_2)k_+ & \sqrt{\frac{\hbar^2}{2m}}\frac{1}{\sqrt{6}}i\,(1+\gamma_1-2\gamma_2)k_+ \\
0 & 0 & \sqrt{\frac{\hbar^2}{2m}}\frac{1}{3}i\,(1+\gamma_1-2\gamma_2-3\gamma_3)k_+ & -\sqrt{\frac{\hbar^2}{2m}}\frac{1}{3\sqrt{2}}i\,(1+\gamma_1-2\gamma_2+6\gamma_3)k_+ & 0 & \sqrt{\frac{\hbar^2}{2m}}\frac{1}{\sqrt{3}}i\,(1+\gamma_1-2\gamma_2-6\gamma_3)k_- & \frac{\hbar^2}{2m}(\gamma_1+2\gamma_2)\frac{\partial}{\partial z} & -\frac{\hbar^2}{2m}2\sqrt{2}\gamma_2\frac{\partial}{\partial z} \\
0 & 0 & \sqrt{\frac{\hbar^2}{2m}}\frac{1}{3\sqrt{2}}i\,(1+\gamma_1-2\gamma_2+6\gamma_3)k_+ & -\sqrt{\frac{\hbar^2}{2m}}\frac{2}{3}i\,(1+\gamma_1-2\gamma_2-3\gamma_3)k_+ & 0 & -\sqrt{\frac{\hbar^2}{2m}}\frac{1}{\sqrt{6}}i\,(1+\gamma_1-2\gamma_2-6\gamma_3)k_- & -\frac{\hbar^2}{2m}2\sqrt{2}\gamma_2\frac{\partial}{\partial z} & \frac{\hbar^2}{2m}\gamma_1\frac{\partial}{\partial z}
\end{bmatrix}$$

Table 7: *The Burt Hamiltonian of Table 5 integrated an infinitesimal distance across an interface in the z direction. All wavevectors are expressed in units of* $\sqrt{\frac{\hbar^2}{2m}}$.

Now consider a discontinuous change in σ, δ and π, representing an interface. If we wish to approach the problem by solving for the states on each side of the interface and then matching at the interface we can obtain the appropriate matching conditions from eq.(75). First, we must have that each $F_s(\boldsymbol{r})$ is continuous otherwise the second derivative in the first term on the left hand side of eq.(74) would diverge, making it impossible for the equation to be satisfied. Second, integrating eq.(75) an infinitesimal distance across the interface (at $z = 0$) in the z direction yields $\left(\int_{-\varepsilon}^{+\varepsilon} \tilde{H}_{ss'} dz\right) F_{s'}(\boldsymbol{r}) = 0$. The integrated symmetrized and Burt Hamiltonians are shown in Table 6 and 7 respectively. Note that in the Burt Hamiltonian there is no need to make the rather ill-defined approximation that the basis functions are the same on each side of the interface, because thay are chosen to be the same throughout the structure.

However, a new problem arises as a result of this choice of basis functions, namely the calculation of the Hamiltonian matrix in at least some parts of the structure. The usual choice of basis functions for a ***k.p*** Hamiltonian matrix is the zone centre states for the relevant bands and the established parameters have been derived with that implicitly assumed. But that is not possible for all parts of the heterostructure. For example if we choose to use the zone centre states of the bands of the bulk material that makes up the well, these will differ from the corresponding states of the barrier material. The only really reliable procedure is to use a more fundamental bandstructure calculation, such as the pseudopotential method, to calculate the Hamiltonian matrix for the well and barrier materials. However, if such an approach is not available, expediency requires the use of the established Hamiltonian for each material, albeit with the implicit assumption of material specific zone centre basis states. Although at first sight this appears as unsatisfactory as the assumption made in association with the symmetrized boundary conditions, there is good reason to believe that it is a rather better approach [31,34]. First, strain apart, symmetry requires that the Hamiltonian matrix elements have the same functional dependence on wavevector, further the diagonal elements at $\boldsymbol{k} = 0$ must give the correct zone centre energies for the bands. Finally, although the parameter P should be the same throughout the structure if the same basis states are used it normally does not vary greatly between the commonly used material and does not in any case appear in the interface matching conditions in the Burt formulation.

To see the effects of the two different boundary conditions, the bandstructure is calculated for a 200 angstrom, $In_{0.47}Ga_{0.53}As/In_{0.74}Ga_{0.26}As_{0.57}P_{0.43}$ quantum well with 0.44% tensile strain. The effects of strain in quantum wells are discussed in [15,23,44-52]. The material parameters used for the calculation are shown in Appendix 1. The conduction bands are shown in Figure 2 for the Burt boundary conditions (which are indistinguishable on the scale of the diagram from the bands obtained using the symmetrized boundary conditions). The small energy differences at $k_{||} = 0$ are given in Table 8.

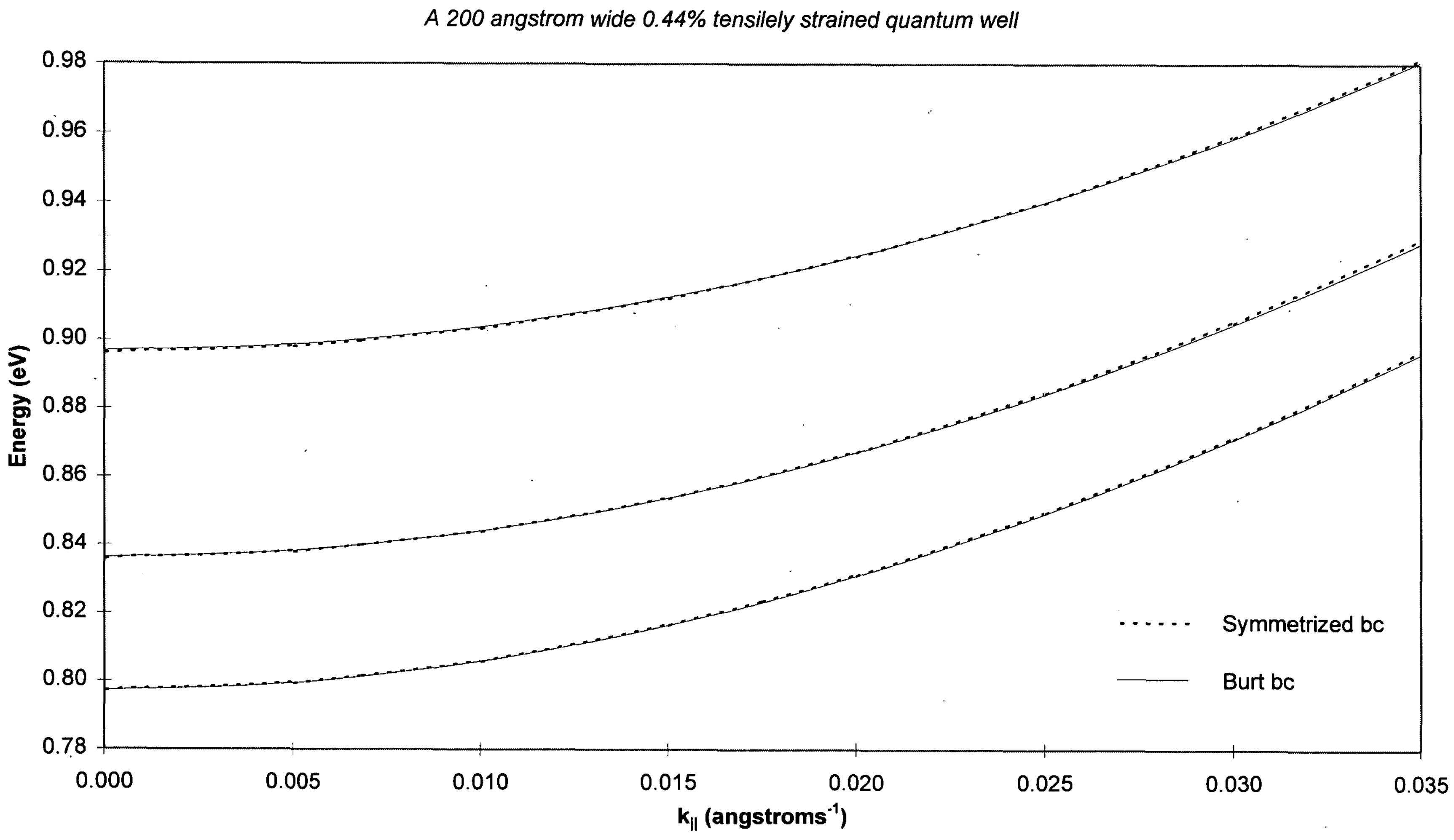

Figure 2: *Conduction bandstructure calculated using the* ***k.p*** *method for the symmetrized (dotted) and the Burt (solid) boundary conditions.*

State	Eigen-energy (eV) for the Burt condition	Eigen-energy (eV) for the symmetrized condition
Conduction 1	0.79724	0.79711
Conduction 2	0.83629	0.83585
Conduction 3	0.89689	0.89613

Table 8: *The three lowest conduction subband energies calculated using the* ***k.p*** *method at* $k_{||}=0$ *for the two boundary conditions for a 200 angstrom wide 0.44% tensilely strained quantum well.*

Figure 3 shows that the choice of boundary conditions is more significant for the valence bands but the differences are still minor. Table 9 presents the band states at $k_{||}=0$. The light hole states are at slightly lower energies with the Burt conditions, but the heavy hole energies are essentially identical which is expected since both the symmetrized and Burt integrated Hamiltonians show that this state is completely decoupled from all other states at $k_{||} = 0$. The insensitivity of the subband structure to the interface matching conditions has also been found by Meney *et al* [40] when the lowest conduction band is included in the basis set along with the three valence bands. Much more significant discrepancies are found when the conduction band is excluded from the basis set. This is because when the conduction band is excluded it makes a large remote band contribution to certain matrix elements which are then incorrectly treated with the symmetrized matrix approach.

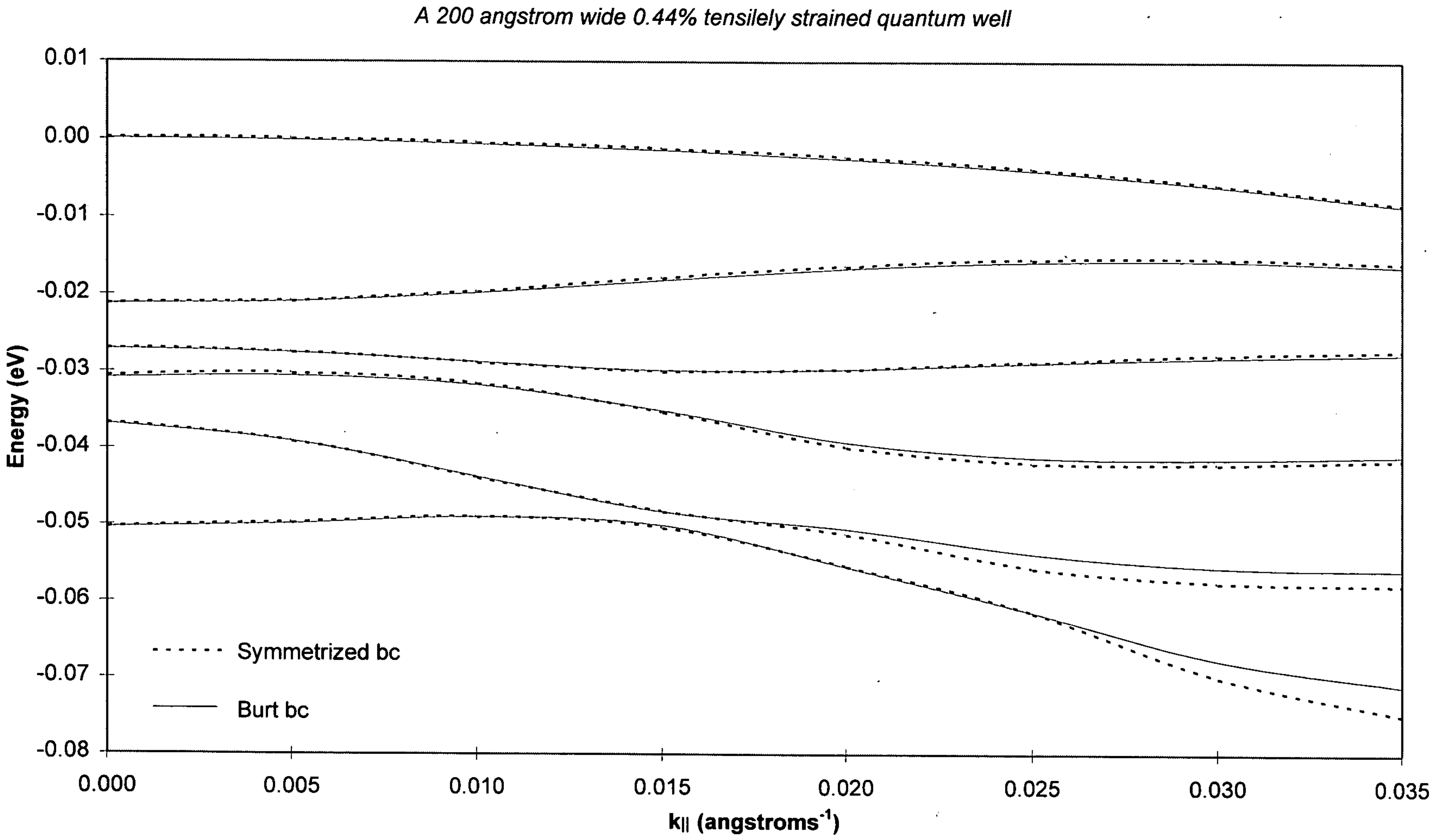

Figure 3: *Valence bandstructure calculated using the* ***k.p*** *method for the symmetrized (dotted) and the Burt (solid) boundary conditions.*

State	Character	Eigen-energy (eV) (Burt)	Eigen-energy (eV) (symmetrized)
Valence 1	light hole	+0.00011	+0.00019
Valence 2	heavy hole	-0.02122	-0.02122
Valence 3	heavy hole	-0.02707	-0.02707
Valence 4	light hole	-0.03086	-0.03061
Valence 5	heavy hole	-0.03680	-0.03680
Valence 6	heavy hole	-0.05036	-0.05036

Table 9: *The six highest valence subband energies calculated using the* ***k.p*** *method at* $k_{||}=0$ *for the two boundary conditions for a 200 angstrom wide 0.44% tensilely strained quantum well.*

2.6 The wave function envelopes

The real part of the envelope functions for the first confined conduction state at $k_{||} = 0$ are shown in Figure 4 (top) for the two boundary conditions. The two boundary conditions produce very similar differences at the edges of the well. The envelope function of the dominant state (u_1 in Table 1) displays a soft kink at both interfaces for the Burt condition and rather smoother behaviour for the symmetrized case. The light hole and spin split off components associated with this conduction state are generally small and combined are approximately 5 times smaller than the dominant conduction envelope function, as measured by the area enclosed between the z axis and the absolute value of the real part of the envelope functions. The envelope

A 200 angstrom wide 0.44% tensilely strained quantum well

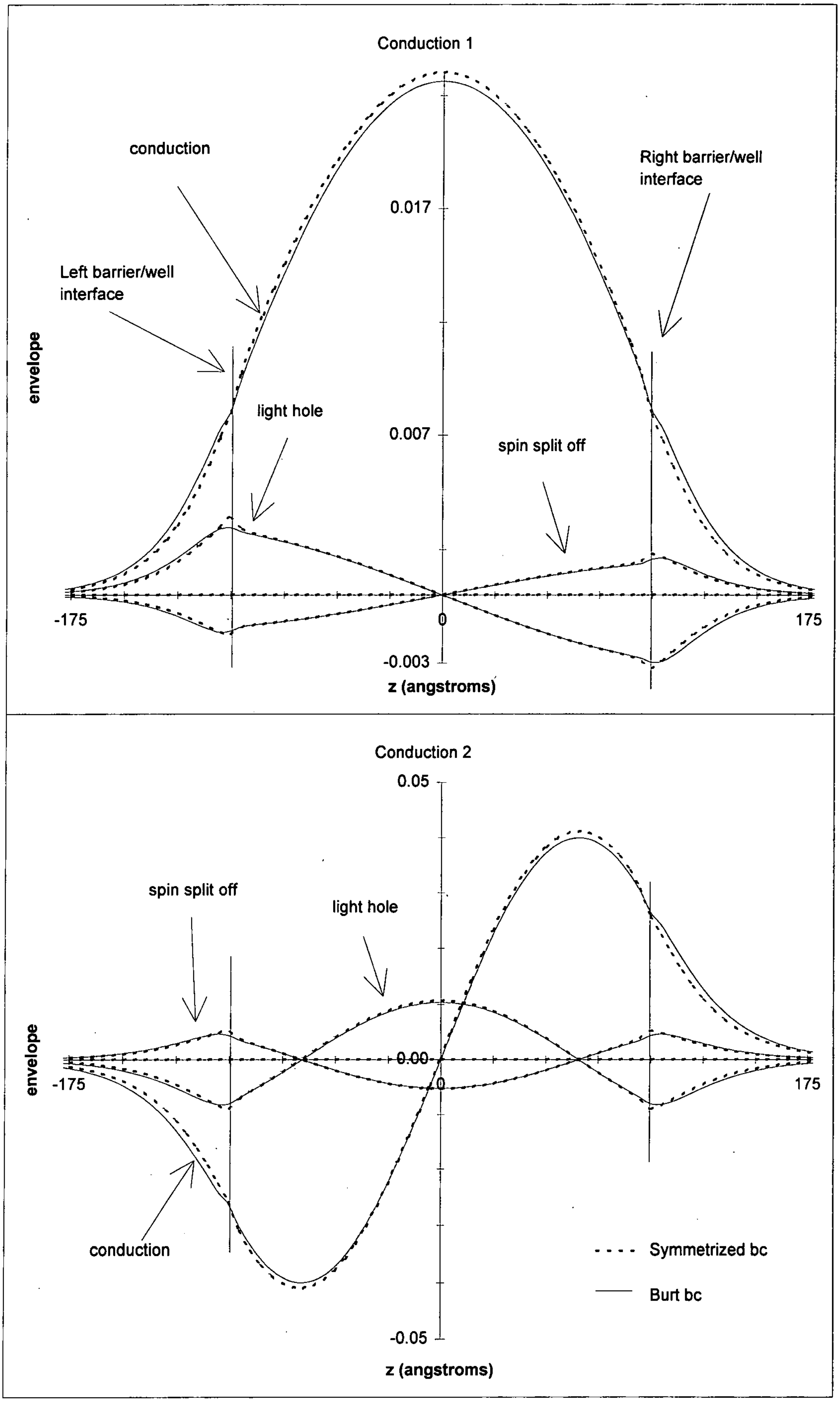

Figure 4: *Real part of envelope functions for the two lowest conduction subbands at $k_{||}=0$ calculated using the **k.p** method for the symmetrized (dotted) and the Burt (solid) boundary conditions.*

functions for the first excited state for the conduction subband at $k_{||}=0$ are shown in Figure 4 (bottom) and exhibit features similar to the first confined conduction state. The combined light hole and spin split off components associated with this conduction state are approximately 3 times smaller than the dominant conduction envelope function.

The envelope functions for the lowest hole subband are shown in Figure 5 (top). It is predominantly light hole in character at the zone centre due to the tensile strain in the well. The dominant envelope function (associated with u_3) has only very small kinks at the interfaces compared to the conduction band and the envelope functions are almost identical for both boundary conditions. The conduction and spin split off components associated with this light hole state are generally small and combined are approximately 5 times smaller than the dominant light hole envelope function. The second hole subband is purely heavy hole in character at the zone centre and the relevant envelope function is shown in Figure 5 (bottom). The two boundary conditions produce identical results. Examination of the coupling terms in Table 6 and 7 show that at $k_{||}=0$ the Burt and symmetrized boundary conditions are identical with no coupling to any other bands. Figure 6 shows the envelope functions for the second heavy hole and second light hole subbands. The combined conduction and spin split off components associated with the second light hole state are approximately 3 times smaller than the dominant light hole envelope function.

A 200 angstrom wide 0.44% tensilely strained quantum well

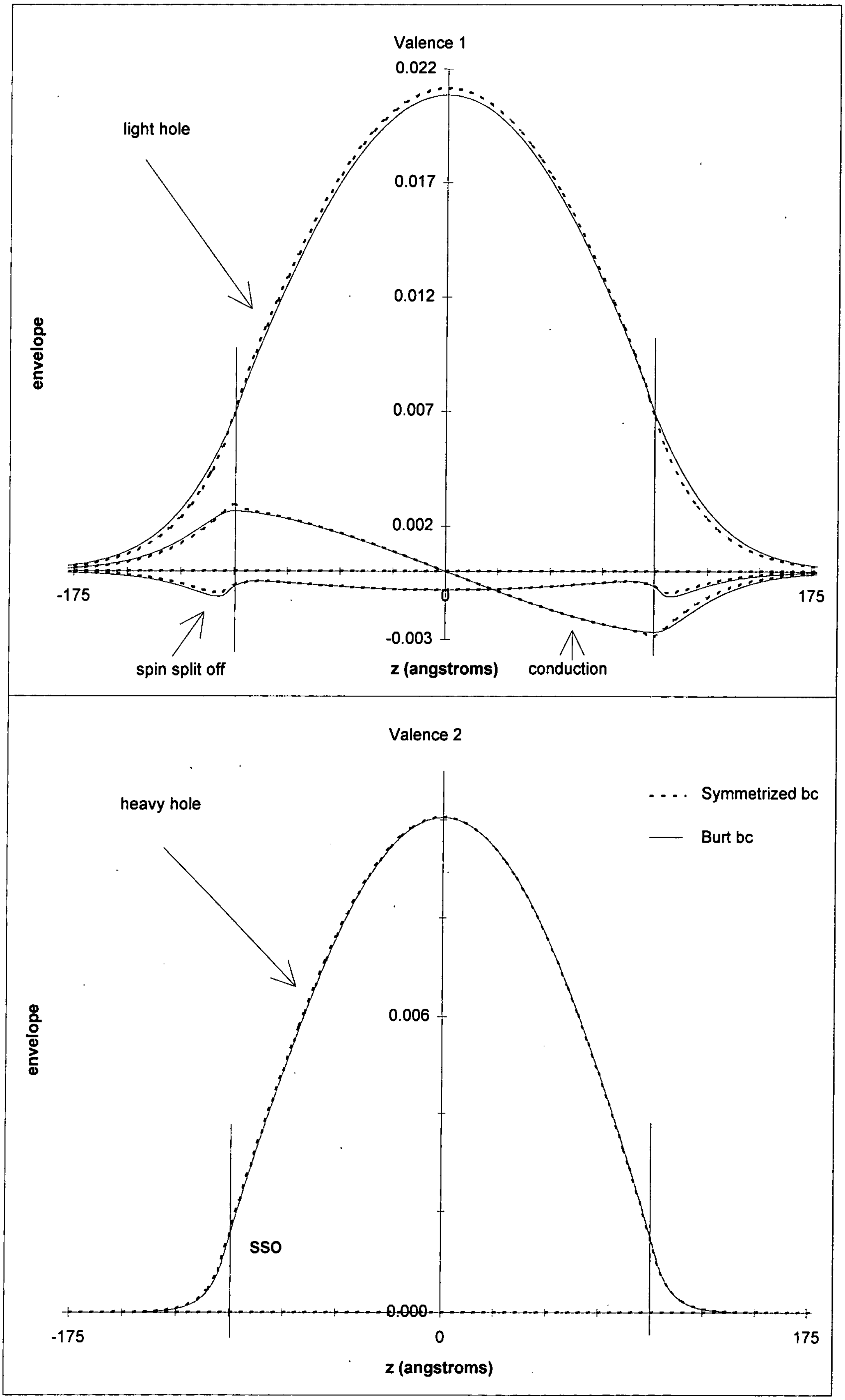

Figure 5: *Real part of envelope functions for the two highest valence subbands at $k_{||}=0$ calculated using the* ***k.p*** *method for the symmetrized (dotted) and the Burt (solid) boundary conditions.*

A 200 angstrom wide 0.44% tensilely strained quantum well

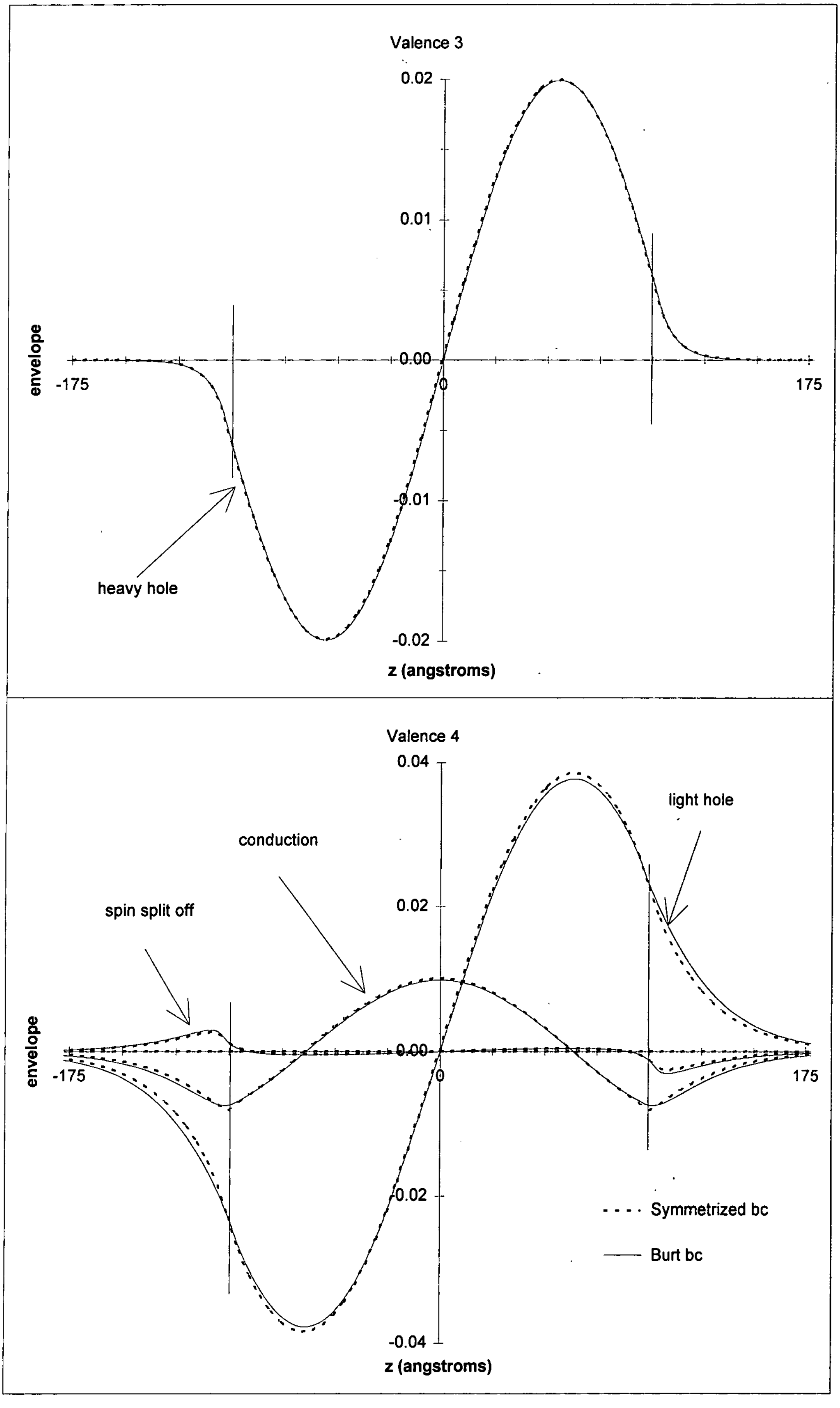

Figure 6: Real part of envelope functions for the third and fourth highest valence subbands at $k_{||}=0$ calculated using the ***k.p*** method for the symmetrized (dotted) and the Burt (solid) boundary conditions.

In conclusion, the two boundary conditions produce almost identical conduction bandstructure. A measure of the difference is that the confined conduction states at $k_{||}=0$ are slightly higher in energy by about 1 meV for the Burt conditions compared to the symmetrized conditions. There is also a similar discrepancy in the light hole bands at $k_{||} = 0$ but the heavy hole bands are essentially identical. The valence subbands have significant but not major differences for the two boundary conditions for wavevectors exceeding about 0.020 $\mathring{A}^{-1}$.

Examination of the wave functions for the $k_{||} = 0$ states of the first few conduction and valence subbands demonstrate that the envelopes derived using both conditions are very similar and show reasonable behaviour.

2.7 One-dimensional effective mass model

It was shown in Section 2.4 that the electronic states and bandstructure of a semiconductor quantum well can be obtained by generalizing the standard text book approach [55] to the solution of Schrodinger's equation for a simple square well. Although this approach is straightforward in principle the multiband nature of the semiconductor does result in mathematical complexity and heavy computational demands in practice. Here we describe some approximations to the method which considerably simplify the calculations. They are particularly appropriate for $k_{||}=0$ and in that case produce results that agree well with the fuller calculations.

$$\boldsymbol{H} = \begin{bmatrix} \boldsymbol{G} & 0 \\ 0 & \boldsymbol{G} \end{bmatrix} \tag{89}$$

where

$$\boldsymbol{G} = \begin{bmatrix} s k_z^2 + E_c + \zeta_1 & 0 & -\sqrt{\frac{2}{3}} iP\, k_z & \sqrt{\frac{1}{3}} iP\, k_z \\ 0 & (2\gamma_2 - \gamma_1) k_z^2 + E_v + \zeta_2 & 0 & 0 \\ \sqrt{\frac{2}{3}} iP\, k_z & 0 & -(2\gamma_2 + \gamma_1) k_z^2 + E_v + \zeta_3 & 2\sqrt{2}\,\gamma_2 k_z^2 + \zeta_5 \\ -\sqrt{\frac{1}{3}} iP\, k_z & 0 & 2\sqrt{2}\,\gamma_2 k_z^2 + \zeta_5 & -\gamma_1 k_z^2 + E_v - \Delta + \zeta_4 \end{bmatrix} \tag{90}$$

With this Hamiltonian the solution of the Schrodinger equation for the bulk, at any given energy, will lead to four doubly degenerate solutions, corresponding to conduction, heavy hole, light hole and spin split off bands. An approximate diagonalisation of ***G*** can be carried out to give ***G***\` where

$$\boldsymbol{G}` =$$

$$\begin{bmatrix} \left(s + \frac{P^2}{3}\left(\frac{2}{E_g} + \frac{1}{E_g + \Delta}\right)\right) k_z^2 + E_c + \zeta_1 & 0 & 0 & 0 \\ 0 & -(\gamma_1 - 2\gamma_2) k_z^2 + E_v + \zeta_2 & 0 & 0 \\ 0 & 0 & -\left(2\gamma_2 + \gamma_1 + \frac{2P^2}{3E_g}\right) k_z^2 + E_v + \zeta_3 & 0 \\ 0 & 0 & 0 & -\left(\gamma_1 + \frac{P^2}{3(E_g + \Delta)}\right) k_z^2 + E_v - \Delta + \zeta_4 \end{bmatrix} \tag{91}$$

To obtain ***G***\` the diagonal elements have been calculated by second order perturbation theory and the non-diagonal elements put equal to zero. The effective masses of each band can be identified in the diagonal elements as

$$\left(s + \frac{P^2}{3}\left(\frac{2}{E_g} + \frac{1}{E_g + \Delta}\right)\right) = \frac{m}{m_c} \tag{92}$$

$$(\gamma_1 - 2\gamma_2) = \frac{m}{m_{hh}} \tag{93}$$

$$\left(2\gamma_2+\gamma_1+\frac{2P^2}{3E_g}\right)=\frac{m}{m_{lh}} \qquad (94)$$

$$\left(\gamma_1+\frac{P^2}{3\left(E_g+\Delta\right)}\right)=\frac{m}{m_{sso}} \qquad (95)$$

which are consistent with equations (15) to (19).

In the case of a quantum well structure the respective Hamiltonians ***G`*** for the well and barrier materials define a well for each band through the difference of the relevant matrix elements at ***k***=0. The appropriate effective masses in the well and barrier follow from equations (92-95). Thus for each band we have a simple one-dimensional problem of the form described by Figure 7.

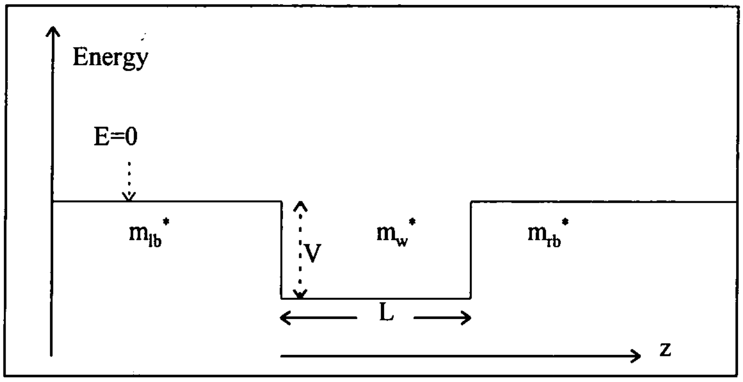

Figure 7: *A square well of depth V and width L. The difference between the relevant matrix elements of the respective Hamiltonians,* ***G`*** *(eq.(91)), for the well and barrier materials at* ***k****=0 define V for each band. The appropriate effective masses in the well and barrier materials are given in eqs.(92-95) and L equals the width of the well layer.*

The general solution to the Schrodinger equation for the structure at energy *E* is

$$\psi = \psi_{\mathrm{lb}} + \psi_{\mathrm{w}} + \psi_{\mathrm{rb}} \tag{96}$$

where

$$\psi_{\mathrm{lb}} = A e^{i k_{lb} z} + B e^{-i k_{lb} z}$$

$$\psi_{\mathrm{w}} = C e^{i k_{w} z} + D e^{-i k_{w} z}$$

$$\psi_{\mathrm{rb}} = E e^{i k_{rb} z} + F e^{-i k_{rb} z} \tag{97}$$

where *lb*, *w* and *rb* denote the left barrier, well and right barrier regions respectively, and

$$k_j = +\sqrt{\frac{2 m_j^*}{\hbar^2}\left(E - V_j\right)} \tag{98}$$

m_j^* = effective mass for region j

V_j = potential energy for region j

The interfacial boundary conditions are that ψ and $\frac{1}{m_j^*}\frac{\partial}{\partial z}\psi$ are continuous. The latter follows directly from the integration of the Schrodinger equation an infinitesimal distance in the *z* direction across an interface. The coefficients *A* and *F* are set equal to zero for E<0 to impose the condition that the wavefunction is finite everywhere. The matching conditions at the left interface are expressed in matrix form as

$$\begin{bmatrix} 1 & 1 \\ \frac{i k_{lb}}{m_{lb}^*} & \frac{-i k_{lb}}{m_{lb}^*} \end{bmatrix} \begin{bmatrix} 0 \\ B \end{bmatrix} = \begin{bmatrix} 1 & 1 \\ \frac{i k_{w}}{m_{w}^*} & \frac{-i k_{w}}{m_{w}^*} \end{bmatrix} \begin{bmatrix} C \\ D \end{bmatrix}$$

or

$$\boldsymbol{M}_{lb}\, \boldsymbol{b}_{lb} = \boldsymbol{M}_{wl}\, \boldsymbol{w} \tag{99}$$

and at the right interface as

$$\begin{bmatrix} e^{i k_w L} & e^{-i k_w L} \\ \frac{i k_w e^{i k_w L}}{m_w^*} & \frac{-i k_w e^{-i k_w L}}{m_w^*} \end{bmatrix} \begin{bmatrix} C \\ D \end{bmatrix} = \begin{bmatrix} e^{i k_{rb} L} & e^{-i k_{rb} L} \\ \frac{i k_{rb} e^{i k_{rb} L}}{m_{rb}^*} & \frac{-i k_{rb} e^{-i k_{rb} L}}{m_{rb}^*} \end{bmatrix} \begin{bmatrix} E \\ 0 \end{bmatrix}$$

or

$$\boldsymbol{M}_{wr}\,\boldsymbol{w} = \boldsymbol{M}_{rb}\,\boldsymbol{b}_{rb} \tag{100}$$

where L is the well width and $z = 0$ at the left interface. Equations (99) and (100) can be combined to give

$$\boldsymbol{b}_{rb} = \boldsymbol{M}_{rb}^{-1}\,\boldsymbol{M}_{wr}\,\boldsymbol{M}_{wl}^{-1}\,\boldsymbol{M}_{lb}\,\boldsymbol{b}_{lb}$$

or

$$\boldsymbol{b}_{rb} = \boldsymbol{N}\,\boldsymbol{b}_{lb} \tag{101}$$

For the case of E<0, energy eigenvalues for the quantum well can be found numerically by looking for energies where the matrix element $N_{22} = 0$. When $N_{22} \neq 0$, an exponentially increasing component in the right barrier exists which implies violation of the condition that the wavefunction must be finite everywhere. The wave function corresponding to a particular eigenvalue can be calculated by setting B in eq.(97) to some arbitrary value (unity say) and then deducing all the remaining coefficients from eqs.(99) and (100).

The wave function obtained in this way is the envelope function associated with the Bloch periodic part of the band under consideration. For example, in the case of the first conduction subband, $c1$, the envelope function, F_c^{c1}, multiplying the conduction basis state is determined using the element G_{11}\` in equation (91) for the well and barrier Hamiltonians. The small light hole, F_{lh}^{c1}, and spin split off, F_{sso}^{c1}, components associated with $c1$ can be calculated approximately by perturbation theory on returning to using eqs.(89) and (90). The Schrodinger equation in matrix form is

$$\begin{bmatrix} \boldsymbol{G} & 0 \\ 0 & \boldsymbol{G} \end{bmatrix} \boldsymbol{c} = E\boldsymbol{c} \tag{102}$$

Writing out explicitly the third component of the left hand side gives

$$G_{31}\, F_c^{\ cl} + G_{33}\, F_{lh}^{\ cl} + G_{34}\, F_{sso}^{\ cl} = E\, F_{lh}^{\ cl} \tag{103}$$

where the F_i are the envelope functions. The third term on the left hand side can be neglected since it is the second derivative of $F_{sso}^{\ cl}$ - a slowly varying function with a generally small magnitude.

$$F_{lh}^{\ cl} \approx \frac{G_{31} F_c^{cl}}{(E - G_{33})} = \sqrt{\frac{2}{3}}\,\frac{P}{E_g^*}\sqrt{\frac{\hbar^2}{2m}}\,\frac{\partial F_c^{cl}}{\partial z} \tag{104}$$

where the k_z appearing in G_{31} is replaced by the operator $\frac{1}{i}\frac{\partial}{\partial z}$ and

$$E_g^* = E\text{-}G_{33} = E_c + \zeta_1 - (E_v + \zeta_3) \tag{105}$$

Similarly, an approximate expression for $F_{sso}^{\ cl}$ can be obtained by writing out the fourth component of the left hand side of eq.(102). It follows

$$F_{sso}^{\ cl} \approx \frac{G_{41} F_c^{cl}}{(E - G_{44})} = -\sqrt{\frac{1}{3}}\,\frac{P}{E_g^{**} + \Delta}\sqrt{\frac{\hbar^2}{2m}}\,\frac{\partial F_c^{cl}}{\partial z} \tag{106}$$

and

$$E_g^{**} + \Delta = E\text{-}G_{44} = E_c + \zeta_1 - (E_v + \zeta_4 - \Delta) \tag{107}$$

For the first light hole subband, *lh1*, the small conduction and spin split off coupled components, $F_c^{\ lh1}$ and $F_{sso}^{\ lh1}$ respectively, can be calculated similarly to give

$$F_c^{\ lh1} \approx \frac{G_{13} F_{lh}^{lh1}}{(E - G_{11})} = \sqrt{\frac{2}{3}}\,\frac{P}{E_g^*}\sqrt{\frac{\hbar^2}{2m}}\,\frac{\partial F_{lh}^{lh1}}{\partial z} \tag{108}$$

where

$$-E_g^* = E\text{-}G_{11} = E_v + \zeta_3 - (E_c + \zeta_1) \tag{109}$$

and

$$F_{sso}^{lhl} = \frac{G_{43} F_{lh}^{lhl} + G_{41} F_c^{lhl}}{(E - G_{44})} \tag{110}$$

$G_{41}\, F_c^{lhl}$ is retained in eq.(110) since it can produce terms comparable to $G_{43}F_{lh}^{lhl}$ even though $F_c^{lhl} << F_{lh}^{lhl}$ normally. Using eq.(108) for F_c^{lhl} gives

$$F_{sso}^{lhl} = \frac{1}{\zeta_3 - \zeta_4 + \Delta}\left[\left(-2\sqrt{2}\,\gamma_2 - \frac{\sqrt{2}}{3}\frac{P^2}{E_g^*}\right)\left(\frac{\hbar^2}{2m}\right)\frac{\partial^2 F_{lh}^{lhl}}{\partial^2 z} + \zeta_5 F_{lh}^{lhl}\right] \tag{111}$$

where

$$E\text{-}G_{44} = E_v + \zeta_3 - (E_v + \zeta_4 - \Delta) = \zeta_3 - \zeta_4 + \Delta \tag{112}$$

Table 10 compares the energy eigenvalues calculated using the full ***k.p*** method and the simpler effective mass approach for the first conduction, heavy hole and light hole states of a 200 angstrom quantum well with 0.44% tensile strain.

State	One-dimensional effective mass model	***k.p*** model with Burt boundary conditions
Conduction	0.8078 eV	0.7972 eV
Heavy hole	-0.0218	-0.0212
Light hole	-0.00004	+0.00011

Table 10: *The energy eigenvalues at* $\mathbf{k}_{||} = 0$ *for the first conduction, heavy hole and light hole states of a 200 angstroms wide 0.44% tensilely strained quantum well calculated using the* ***k.p*** *method and the one-dimensional effective mass approach.*

The corresponding envelope functions are compared in Figure 8. The main envelope functions obtained from the effective mass model have been scaled to equal the value of the corresponding ***k.p*** functions at the centre of the well. The other envelope functions are calculated directly with no further scaling. It is apparent that all the effective mass envelope functions generally show excellent agreement with those calculated using the ***k.p*** method, as do the energy eigenvalues. The discontinuities at the interfaces seen in the minor envelope functions in the effective mass approach arise from the spatial derivatives of the main envelope functions with discontinuities in gradient at the interfaces - see the comment on wave function continuity after eq.(98), and the form of eq.(104).

2.8 Calculation of the optical matrix elements

In the presence of an electromagnetic field, the Hamiltonian for an electron in a periodic potential *V(r)* is given by

$$\boldsymbol{H}=\frac{1}{2m}\left(\boldsymbol{p}+|e|\boldsymbol{A}\right)^2+V(\boldsymbol{r}) \tag{113}$$

The vector potential $\boldsymbol{A}$, of a monochromatic plane electromagnetic wave, is of the form

$$\boldsymbol{A}(\boldsymbol{r},t)=\boldsymbol{A}_0\cos(\boldsymbol{k}.\boldsymbol{r}-\omega t) \tag{114}$$

and the resulting perturbation to the semiconductor Hamiltonian is written as

$$\boldsymbol{H}` =\frac{|e|}{2m}\left[e^{i\omega t}+e^{-i\omega t}\right]\boldsymbol{A}_0\cdot\boldsymbol{p} \tag{115}$$

A 200 angstrom wide 0.44% tensilely strained quantum well

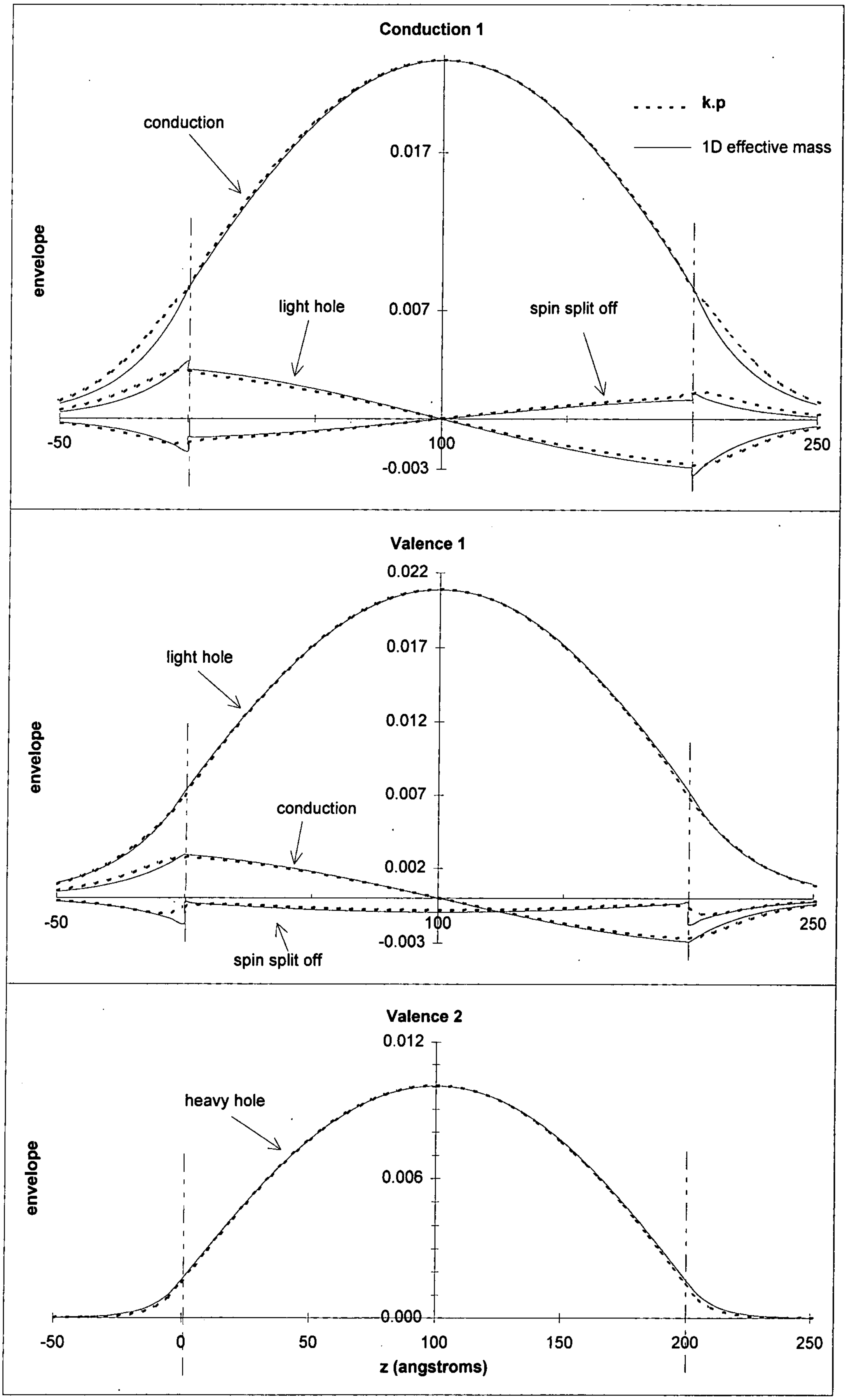

Figure 8: *Real part of envelope functions for the lowest conduction and two highest valence subbands at* $k_{\parallel}=0$ *calculated using 1D effective mass and* ***k.p*** *models.*

in the conventional approximations [61]. The exponential terms correspond to photon emission and absorption respectively. The transition rates are determined by Fermi's Golden Rule, which states that the probability per unit time that a perturbation of the form $\mathbf{H}``e^{\pm i\omega t}$ induces a transition from state i with energy E_i to state f with energy E_f is

$$\rho_{i\to f} = \frac{2\pi}{\hbar}\left|\left\langle f\left|\frac{|e|}{2m}\mathbf{A}_0\cdot\mathbf{p}\right|i\right\rangle\right|^2 \delta\left(E_f - E_i \mp \hbar\omega\right) \tag{116}$$

where $\mathbf{A}_0 = A_0\,\mathbf{e}$, and $\mathbf{e}$ is a unit vector in the direction of the electric field. The rate at which optical transitions occur in semiconductors is obtained by calculating the squared optical matrix element

$$M^2 = \left|\langle i|\mathbf{e}\cdot\mathbf{p}|f\rangle\right|^2 \tag{117}$$

The optical matrix element between the quantum well states ψ_i and ψ_f is

$$M^2 = \left|\int_{-\infty}^{z1}\psi_f^*\mathbf{e}\cdot\mathbf{p}\psi_i d^3\mathbf{r} + \int_{z1}^{z2}\psi_f^*\mathbf{e}\cdot\mathbf{p}\psi_i d^3\mathbf{r} + \int_{z2}^{+\infty}\psi_f^*\mathbf{e}\cdot\mathbf{p}\psi_i d^3\mathbf{r}\right|^2 \tag{118}$$

where z_1 and z_2 are the left and right heterointerfaces respectively, and

$$\psi_i = \sum_m \sum_n A_m F_{mn}\, e^{i\mathbf{k}_m\cdot\mathbf{r}}\,|u_n\rangle \tag{119}$$

and

$$\psi_f = \sum_l \sum_j A_l F_{lj}\, e^{i\mathbf{k}_l\cdot\mathbf{r}}\,|u_j\rangle \tag{120}$$

This form of the wave function was introduced in Section (2.4). Each of the three integrals in eq.(124) can be written as

$$I = \int_{z=a}^{z=b}\sum_l\sum_j\sum_m\sum_n A_l^* F_{lj}^* e^{-i\mathbf{k}_l^*\cdot\mathbf{r}} u_j^*(\mathbf{r})\mathbf{e}\cdot\mathbf{p}\, A_m F_{mn} e^{i\mathbf{k}_m\cdot\mathbf{r}} u_n(\mathbf{r})\, d^3\mathbf{r}$$

$$= \sum_{ljmn} C_{ljmn} \int_{z=a}^{z=b} e^{i(\boldsymbol{k}_m - \boldsymbol{k}_l^*)\cdot \boldsymbol{r}} \left[\hbar \, \boldsymbol{k}_m^e u_j^*(\boldsymbol{r}) \, u_n(\boldsymbol{r}) + u_j^*(\boldsymbol{r}) \boldsymbol{e} \cdot \boldsymbol{p} \, u_n(\boldsymbol{r}) \right] d^3 \boldsymbol{r} \tag{121}$$

where $\boldsymbol{k}_m{}^e$ is the component of $\boldsymbol{k}_m$ along the electric field vector. Integrating over the *x*-*y* plane

$$I = (Area)\, \delta_{k_{\|m} k_{\|l}} \sum_{ljmn} C_{ljmn} \left[\hbar \, \boldsymbol{k}_m^e \delta_{jn} + \langle u_j | \boldsymbol{e} \cdot \boldsymbol{p} | u_n \rangle \right] \int_{z=a}^{z=b} e^{i(k_{zm} - k_{zl}^*) z} \, dz \tag{122}$$

where

Area = area of *x*-*y* plane integrated over

$$\int_{-\infty}^{z_1} e^{i(k_{zm} - k_{zl}^*) z} \, dz = \frac{e^{\left(\frac{-i}{2} (k_{zm} - k_{zl}^*) w \right)}}{i(k_{zm} - k_{zl}^*)}$$

$$\int_{z_1}^{z_2} e^{i(k_{zm} - k_{zl}^*) z} \, dz = w \frac{\sin\left(\frac{w}{2} (k_{zm} - k_{zl}^*) \right)}{\frac{w}{2} (k_{zm} - k_{zl}^*)}$$

$$\int_{z_2}^{+\infty} e^{i(k_{zm} - k_{zl}^*) z} \, dz = \frac{e^{\left(\frac{i}{2} (k_{zm} - k_{zl}^*) w \right)}}{i(k_{zm} - k_{zl}^*)} \tag{123}$$

and w is the well width. The integrals for each of the three quantum well regions (left barrier, well and right barrier) can be determined from the respective ***k.p*** envelope functions and hence the squared optical matrix element is calculated from eq.(118).

2.9 Calculation of the optical absorption coefficient

The absorption coefficient resulting from electronic transitions between a valence state *j* and a conduction state *i* of a quantum well can be written as [6,56]

$$\alpha_{ij}(\hbar\omega) = \int \frac{\pi e^2 \hbar}{m^2 \varepsilon_0 \mu \hbar \omega c L_z} |M_{ij}|^2 (f_v - f_c) \delta(E_{ij} - \hbar\omega) d\boldsymbol{k}_{\|} \tag{124}$$

where

μ = refractive index of the well material

$\hbar\omega$ = photon energy

c = speed of light

L_z = well width

M_{ij} = optical matrix element between bands i and j (function of $\boldsymbol{k}_{\|}$)

E_{ij} = energy separation of states i and j at the same wavevector $\boldsymbol{k}_{\|}$

f_v & f_c = the Fermi occupation factors which are the probabilities that the states of the valence band and conduction band respectively are occupied by an electron at a given energy

ε_0 = permittivity of free space

In general optical absorption is the result of transitions between a number of bands and the absorption coefficient is obtained by summing the right hand side of eq.(124) over all the bands concerned

$$\alpha(\hbar\omega) = \sum_{ij} \alpha_{ij}(\hbar\omega) \tag{125}$$

If it is assumed that the bands are isotropic in the x-y plane, then equations (124) and (125) can be re-written as

$$\alpha(\hbar\omega) = \sum_{ij} \int \frac{\pi e^2 \hbar}{m^2 \varepsilon_0 \mu\hbar\omega c L_z} \left|M_{ij}\right|^2 (f_v - f_c) \delta(E_{ij} - \hbar\omega) \frac{4\pi k_{\|}}{(2\pi)^2} d k_{\|} \tag{126}$$

It is often convenient to change the variable of integration to energy

$$\alpha(\hbar\omega) = \sum_{ij} \int \frac{\pi e^2 \hbar}{m^2 \varepsilon_0 \mu\hbar\omega c L_z} \left|M_{ij}\right|^2 (f_v - f_c) \delta(E_{ij} - \hbar\omega) \rho_{ij} d E_{ij} \tag{127}$$

where

$$\rho_{ij} = \text{the joint density of states} = \frac{k_{\parallel}}{\pi}\left|\frac{d\,k_{\parallel}}{d\,E_{ij}}\right| \tag{128}$$

Equation (127) predicts that transitions only occur when $\hbar\omega = E_{ij}$ and the absorption displays a step like structure. However, experimental data invariably display a series of smoothed peaks with the rounding of the spectral features predominantly ascribed to electron-phonon interactions [57-60,62]. For example a transition of an electron from a valence to a conduction band state (due to the absorption of a photon) leaves an unoccupied state in the valence band. This state can be filled by another valence band electron as it undergoes scattering. Therefore, the hole formed in the valence band has a lifetime associated with it which is determined by the intraband scattering process, and this results in a broadened spectrum. In common with some other workers [57-60,62] this type of scattering is included approximately in our model by replacing the energy delta function by a Lorentzian. The expression for the absorption coefficient is then written as

$$\alpha^{broad}(\hbar\omega) = \sum_{ij}\int_{-\infty}^{+\infty} \frac{\pi e^2 \hbar}{m^2 \varepsilon_0 \mu \hbar\omega c L_z} \left|M_{ij}\right|^2 \left(f_v - f_c\right)\rho_{ij}\frac{L\left(E_{ij}-\hbar\omega\right)}{\pi}\, d\,E_{ij} \tag{129}$$

where

$$L\left(E_{ij}-\hbar\omega\right) = \frac{\Gamma}{\left(E_{ij}-\hbar\omega\right)^2 + \Gamma^2}$$

$$\Gamma = \frac{\hbar}{\tau_{\mathrm{int}\,ra}}$$

and τ_{intra} is the intraband relaxation time. For laser applications, where electrons and holes are injected into the conduction and valence bands respectively, the photon absorption rate can be less than the stimulated emission rate which results in a negative absorption coefficient. Therefore in laser theory it is more usual to define the gain coefficient which is the negative of equation (129).

In summary, this chapter has discussed the methodology for the calculation of quantum well bandstructure and electronic states. The interfacial boundary conditions which result from Burt's exact envelope function theory were calculated and included in the ***k.p*** bandstructure model. The effects of the boundary conditions on the electronic states and bandstructure of a 200 angstrom quantum well with 0.44% tensile strain were examined and compared to those derived from the usual symmetrized Hamiltonian approach. The results compared favourably with only very small energy shifts in the conduction and light hole confined states, and small modifications to the band effective masses at large in-plane wavevector.

The calculation of the electronic states of a quantum well, at zero in-plane wavevector, using the simpler one-dimensional effective mass model was described. The calculated energy eigenvalues and envelope functions at zero in-plane wavevector for a 200 angstrom wide quantum well with 0.44% tensile strain agreed very well with those obtained from the full ***k.p*** model.

The calculation of the optical matrix elements from the ***k.p*** envelope functions was discussed. An expression for the absorption coefficient in terms of the bandstructure and state functions was presented.

References for Chapter Two

[1] E. O. Kane, 'Energy band theory', *Handbook on Semiconductors*, vol. 1, 1982, pp 193-217

[2] E. O. Kane, 'The **k.p** method', *Semiconductors and Semimetals*, pp 75-100 (1966)

[3] E. O. Kane, J. Phys. Chem. Solids **1**, 82 (1956)

[4] E. O. Kane, J. Phys. Chem. Solids **1**, 249 (1957)

[5] P. Lowdin, J. Chem. Phys. **19**, 1396 (1951)

[6] R. Eppenga, M. F. H. Schuurmans and S. Colak, Phys. Rev. B, **36**, 1554 (1987)

[7] J. M. Luttinger and W. Kohn, Phys. Rev. B, **97**, 869 (1955)

[8] G. Dresselhaus, A. F. Kip and C. Kittel, Phys. Rev. B, **98**, 368 (1955)

[9] S. R. White and L. J. Sham, Phys. Rev. Lett., 47, 879 (1981)

[10] D. C. Smith and C. Mailhiot, Phys. Rev. B, **33**, 8345 (1986)

[11] D. C. Smith and C. Mailhiot, Phys. Rev. B, **33**, 8360 (1986)

[12] J. W. Matthews and A. E. Blakeslee, J. Cryst. Growth, **27**, 118 (1974)

[13] J. W. Matthews and A. E. Blakeslee, J. Cryst. Growth, **29**, 273 (1975)

[14] J. W. Matthews and A. E. Blakeslee, J. Cryst. Growth, **32**, 265 (1976)

[15] E. P. O' Reilly, Semicond. Sci. Technol., **4**, 121 (1989)

[16] J. C. Bean, L. C. Feldman, A. T. Fiory, S. Nakahara and I. K. Robinson, J. Vac. Sci. Technol. A, **2**, 436 (1984)

[17] I. J. Fritz, S. T. Picraux, L. R. Dawson, T. J. Drummond, W. D. Laidig and N. G. Anderson, Appl. Phys. Lett., **46**, 967 (1985)

[18] T. J. Andersson, Z. G. Chen, V. D. Kulakovski, A. Uddin and J. T. Vallin, Appl. Phys. Lett, **51**, 752 (1987)

[19] G. L. Bir and G. E. Pikus, Sov. Phys. Solid State, **1**, 1502 (1960)

[20] G. L. Bir and G. E. Pikus, Sov. Phys. Solid State, **3**, 2221 (1961)

[21] G. L. Bir and G. E. Pikus, *Symmetry and Strain-Induced Effects in Semiconductors*, Wiley (1974)

[22] T. B. Bahder, Phys. Rev. B, **41**, 11992 (1990)
(plus erratum in Phys. Rev. B, **46**, 9913 (1992))

[23] T. B. Bahder, Phys. Rev. B, **45**, 1629 (1992)

[24] W. Potz and D. K. Ferry, Superlattices and Microstructures, **3**, 57 (1987)

[25] R. A. Morrow and K. R. Brownstein, Phys. Rev. B, **30**, 678 (1984)

[26] G. Bastard, Phys. Rev. B, **24**, 5693 (1981)

[27] G. Bastard, Phys. Rev. B, **25**, 7584 (1982)

[28] M. Altarelli, Physica **117B & 118B**, 747 (1983)

[29] M. Altarelli, Phys. Rev. B, **28**, 842 (1983)

[30] M. Altarelli, U. Ekenberg and A. Fasolino, Phys. Rev. B, **32**, 5138 (1985)

[31] M. G. Burt, Semicond. Sci. Technol., **2**, 460 (1987)

[32] M. G. Burt, Semicond. Sci. Technol., **3**, 739 (1988)

[33] M. G. Burt, *Bandstructure Engineering in Semiconductor Microstructures*, ed. R. A. Abram & M. Jaros (1988)

[34] M. G. Burt, J. Phys: Condens. Matter, **4**, 6651 (1992)

[35] M. G. Burt, Appl. Phys. Lett., **65**, 717 (1994)

[36] M. G. Burt, Phys. Rev. B, **50**, 7518 (1994)

[37] M. G. Burt, Semicond. Sci. Technol., 2, 460 (1987)

[38] B. A. Foreman, Phys. Rev. B, **48**, 4964 (1993)

[39] B. A. Foreman, Phys. Rev. B, **49**, 1757 (1994)

[40] A. T. Meney, Besire Gonul and E. P. O' Reilly, Phys. Rev. B, 50, 10893 (1994)

[41] S. Nojima, J. Appl. Phys., **31**, L1401 (1992)

[42] A. Brezini and M. Sebbani, Phys. Stat. Sol. (b), **178**, 141 (1993)

[43] A. Brezini and N. Zekri, Solid State Commun., **86**, 613 (1993)

[44] J. P. Loehr and J. Singh, J. Quant. Elect., **27**, 708 (1991)

[45] S. W. Corzine and L. A. Coldren, Appl. Phys. Lett., **59**, 588 (1991)

[46] M. Sugawara, Appl. Phys. Lett., **60**, 1842 (1992)

[47] M. Silver, W. Batty, A. Ghiti and E. P. O' Reilly, Phys. Rev. B, **46**, 6781 (1992)

[48] K. Zitouni, K. Rerbal and A. Kadri, Superl. and Microstr., **13**, 347 (1993)

[49] M. Sugawara, N. Okazaki, T. Fujii and S. Yamazaki, Phys. Rev. B, **48**, 8102 (1993)

[50] D. Ahn, J. Quant. Elect., **30**, 350 (1994)

[51] S. Seki, J. Quant. Elect., **30**, 500 (1994)

[52] M. Ogawa and T. Miyoshi, Jpn.J. Appl. Phys., **34**, 3043 (1995)

[53] R. People and J. C. Bean, Appl. Phys. Lett., **47**, 322 (1985)

[54] E. Kasper, Surface Science, **174**, 630 (1986)

[55] F. Richtmyer, E. Kennard and J. Cooper, *Introd. to Modern Physics* (ed. 6), Tata McGraw-Hill (1986)

[56] G. Sanders and K. Bajaj, Phys. Rev. B, **35**, 2308 (1987)

[57] D. Atkinson, G. Parry and E. Austin, Semicond. Sci. Technol., **5**, 516 (1990)

[58] M. Ogawa and T. Miyoshi, Jpn. J. Appl. Phys., **34**, 4535 (1995)

[59] A. Kucharska and D. J. Robbins, IEEE J. Quant. Elect., **QE26**, 443 (1990)

[60] M. Asada, IEEE J. Quant. Elect., **QE25**, 2019 (1989)

[61] J. Singh, *Semiconductor Optoelectronics*, *Physics and Technology*, McGraw-Hill (1995)

[62] M. P. Houng, Y. H. Wang and C. H. Chu, J. Appl. Phys., **77**, 6338 (1995)

CHAPTER THREE

ASYMMETRIC COUPLED QUANTUM WELL MODULATORS

3.1 Introduction

In this chapter the ***k.p*** method for calculating the bandstructure presented in Chapter 2 is developed to describe the case of coupled quantum wells in an applied electric field. The calculation of the absorption spectra from the bandstructure is also discussed. The model is applied to two structures that could form the basis of intensity modulators for light of wavelength 1.55 μm, and the results are discussed in terms of the electric field dependence of the spatial confinement of the wave function, optical matrix elements and densities of states. The results of experimental studies of two similar structures are discussed briefly. In addition the behaviour of the bandedge energies, wave functions and optical matrix elements are examined using a one-dimensional multi-layer effective mass model, and the results of the simple calculational method are compared with those of the ***k.p*** method.

3.2 Bandstructure of a multi-layer structure in an applied electric field

The effects of an applied electric field can be incorporated into the method of bandstructure calculation described in Chapter 2 by including a potential term into each of the diagonal elements of the bulk Hamiltonian [1-3]. If the field is uniform and applied in the *z* direction the potential term is simply linearly dependent on *z*. The method adopted to solve for the electronic states is to break the well of the system up into a finite number of layers where the potential is taken as constant and equal to the average local value [4,5] as shown in Figure 1. The actual potential profile is approached as the number of layers is increased for a given structure. However, in practice the number of layers is kept to the minimum that provides an acceptable level of accuracy in the wave functions and energy eigenvalues of the electronic states of interest.

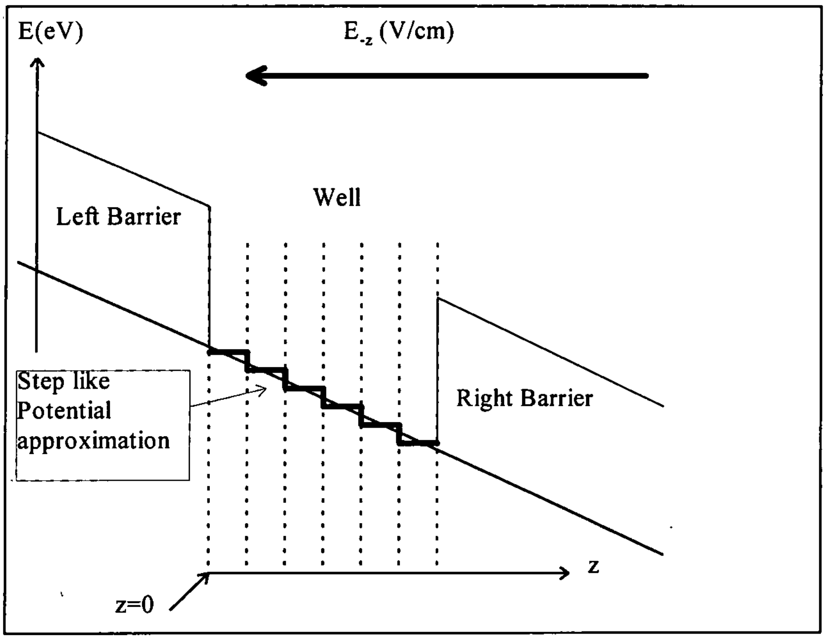

Figure 1: *A quantum well in an applied electric field. The well is broken into a number of equal width layers. The potential in each of the well layers is taken as constant and equal to the average local value.*

The model is simplified further by ignoring the effect of electric field in the barriers, as shown in Figure 2. In general, for small field strengths, this has only a minor effect on the calculated bound states because wave function penetration into the barriers is relatively small. However, it avoids the need to break the barriers into layers and the complications associated with the (normally insignificant) tunnelling through the triangular right barrier.

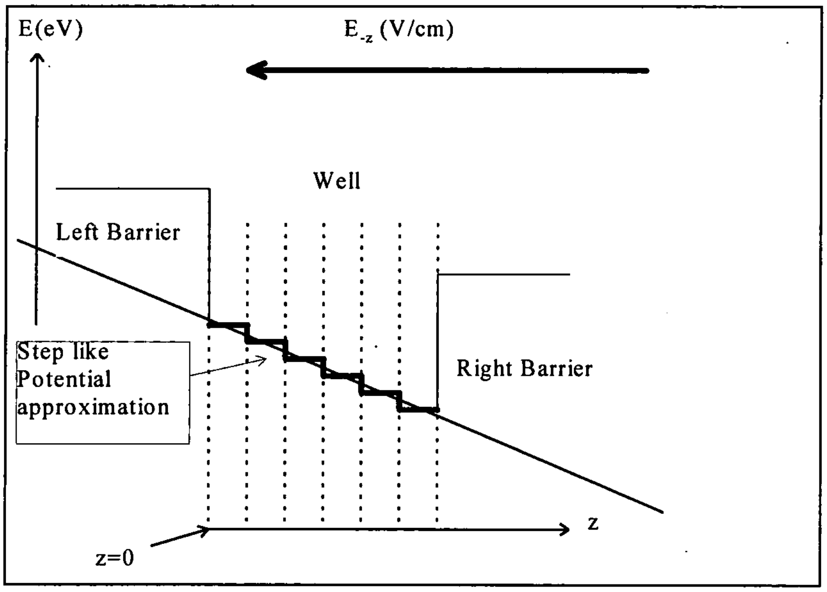

Figure 2: *A quantum well in an applied electric field. The well is broken into a number of equal width layers. The potential in each of the well layers is taken as constant and equal to the average local value. The effect of the electric field in the barriers is ignored.*

The procedure described in Chapter 2 can now be used to seek solutions to the Schrodinger equation for the quantum well system of Figure 2. The bandedge energy in each layer is known and hence *bulk* wave functions can be obtained for the same energy and in-plane wavevector in each layer. Allowed states occur when the wave functions can be matched at all the interfaces in the system while satisfying the boundary condition that the wavefunction goes to zero for $z \rightarrow \pm\infty$. For the left barrier/left well layer interface the boundary conditions can be expressed in matrix form (see eqs.(49) and (52) of Chapter 2) as

$$\begin{bmatrix} F_0^R \\ D_0^R \end{bmatrix} [L] = \begin{bmatrix} F_1^L \\ D_1^L \end{bmatrix} [W_1] \tag{1}$$

(16x8)(8x1) = (16x16)(16x1)

where the subscripts indicate the layer number (0 being the left barrier and 1 being well layer 1) and the superscripts indicate the interface (right or left) for the layer in question. The dimensions of the matrices are indicated beneath the equation. Similarly, the interface conditions for the well layer 1/well layer 2 can be written as

$$\begin{bmatrix} F_1^R \\ D_1^R \end{bmatrix} [W_1] = \begin{bmatrix} F_2^L \\ D_2^L \end{bmatrix} [W_2] \tag{2}$$

(16x16)(16x1) = (16x16)(16x1)

and for the mth interface

$$\begin{bmatrix} F_{m-1}^R \\ D_{m-1}^R \end{bmatrix} [W_{m-1}] = \begin{bmatrix} F_m^L \\ D_m^L \end{bmatrix} [W_m] \tag{3}$$

If the right barrier is the (n+1)th layer the equation for the rightmost interface is

$$\begin{bmatrix} F_n^R \\ D_n^R \end{bmatrix} [W_n] = \begin{bmatrix} F_{n+1}^L \\ D_{n+1}^L \end{bmatrix} [R] \tag{4}$$

(16x16)(16x1) = (16x8)(8x1)

The matrix equations (1)-(3) can be combined and written as

$$\begin{bmatrix} F_0^R \\ D_0^R \end{bmatrix} [L] = \begin{bmatrix} F_1^L \\ D_1^L \end{bmatrix} \begin{bmatrix} F_1^R \\ D_1^R \end{bmatrix}^{-1} \begin{bmatrix} F_2^L \\ D_2^L \end{bmatrix} \cdots\cdots \begin{bmatrix} F_{n-1}^R \\ D_{n-1}^R \end{bmatrix}^{-1} \begin{bmatrix} F_n^L \\ D_n^L \end{bmatrix} [W_n] \tag{5}$$

or

$$\begin{bmatrix} F_0^R \\ D_0^R \end{bmatrix} [L] = \begin{bmatrix} F_{tot} \\ D_{tot} \end{bmatrix} [W_n] \tag{6}$$

Equations (4) & (6) can be split and reconstituted to give

$$\begin{bmatrix} \boldsymbol{F}_0^R & 0 \\ 0 & \boldsymbol{F}_{n+1}^L \end{bmatrix} \begin{bmatrix} \boldsymbol{L} \\ \boldsymbol{R} \end{bmatrix} = \begin{bmatrix} \boldsymbol{F}_{tot} \\ \boldsymbol{F}_n^R \end{bmatrix} [\boldsymbol{W}_n] \tag{7}$$

and

$$\begin{bmatrix} \boldsymbol{D}_0^R & 0 \\ 0 & \boldsymbol{D}_{n+1}^L \end{bmatrix} \begin{bmatrix} \boldsymbol{L} \\ \boldsymbol{R} \end{bmatrix} = \begin{bmatrix} \boldsymbol{D}_{tot} \\ \boldsymbol{D}_n^R \end{bmatrix} [\boldsymbol{W}_n] \tag{8}$$

Combining equations (7) & (8)

$$\begin{bmatrix} \boldsymbol{F}_0^R & 0 \\ 0 & \boldsymbol{F}_{n+1}^L \end{bmatrix} \begin{bmatrix} \boldsymbol{L} \\ \boldsymbol{R} \end{bmatrix} = \begin{bmatrix} \boldsymbol{F}_{tot} \\ \boldsymbol{F}_n^R \end{bmatrix} \begin{bmatrix} \boldsymbol{D}_{tot} \\ \boldsymbol{D}_n^R \end{bmatrix}^{-1} \begin{bmatrix} \boldsymbol{D}_0^R & 0 \\ 0 & \boldsymbol{D}_{n+1}^L \end{bmatrix} \begin{bmatrix} \boldsymbol{L} \\ \boldsymbol{R} \end{bmatrix} \tag{9}$$

Therefore, solutions to the multi-layered structure occur when

$$\det \left[\begin{bmatrix} \boldsymbol{F}_0^R & 0 \\ 0 & \boldsymbol{F}_{n+1}^L \end{bmatrix} - \begin{bmatrix} \boldsymbol{F}_{tot} \\ \boldsymbol{F}_n^R \end{bmatrix} \begin{bmatrix} \boldsymbol{D}_{tot} \\ \boldsymbol{D}_n^R \end{bmatrix}^{-1} \begin{bmatrix} \boldsymbol{D}_0^R & 0 \\ 0 & \boldsymbol{D}_{n+1}^L \end{bmatrix} \right] = 0 \tag{10}$$

This is similar to eq.(57) of Chapter 2 for a single quantum well in the absence of applied field. When eq.(10) is satisfied the wave function coefficients for the barriers can be determined from eq.(9) and for the rightmost well layer from eq.(8). The coefficients for the remaining layers are determined from eqs.(3) to (2) (working backwards from *n* to 1). The wave function for the chosen in-plane wave vector and the energy determined by eq.(10) is then completely specified. It is straightforward to extend the model to describe more wells and barriers, for example a structure with two coupled quantum wells.

The one-dimensional effective mass model, developed in Chapter 2, has been similarly extended to allow the calculation of the electronic states of a multi-layered semiconductor structure in an applied electric field.

3.3 Calculated absorption spectra for asymmetric coupled quantum wells in an applied electric field

High speed intensity modulation of 1.55 μm light, the wavelength at which minimum dispersion and absorption occurs for silica based fibres, is of primary importance for optical communication [43]. Such modulation can be achieved by electric field effects in quantum well structures, and other applications of this technique include self-linearized modulators [44], wavelength selective detectors [45] and optically bistable switches [46]. Here we consider the potential of a double well structure to act as a modulator at 1.55 μm. In many cases, quantum well spatial light modulators are designed so that the lowest transition energy coincides with the photon energy of the light source in the presence of applied field, resulting in absorption. When the applied field is turned off the lowest energy transition shifts to larger energy resulting in little or no absorption of the incident light. Hence, in order to achieve strong modulation, large changes in absorption with electric field at the source wavelength must occur.

Large shifts in the absorption edge wavelength with applied voltage, via the Quantum Confined Stark Effect [2,25-26], offer the possibility of modulation at low device drive voltage. Wide quantum wells manifest such shifts, but the absorption also decreases significantly with electric field because the optical matrix element between the ground conduction and valence states decreases due to their spatial separation [5,8,9,14,38]. However, it has been shown that the introduction of tensile strain into the well material results in a less field sensitive optical matrix element

[11,13]. Asymmetric (parabolic and triangular) quantum wells have also been examined by a number of authors [5,39,40-42]. Coupled identical quantum wells have also demonstrated improved modulator performance compared to the single square quantum well [7,17,54]. Coupled different quantum wells form an asymmetric structure and can manifest large absorption changes either via a strong Stark shift, resulting from the large effective well width, or via an exchange of oscillator strength between the c1-hh1 and normally forbidden c1-hh2 transitions with applied electric field. The latter effect derives from the extended nature of the ground electron wave function and the effective localisation of hh1 and hh2 wave functions to different quantum wells [14,51,55,56,58,62].

In particular GEC-Marconi proposed the following two structures to develop as the optical links for particle sensors in the European Large Hadron Collider Experiment at CERN [6,47].

Structure 1 shown in Figure 3: *n* doped (~ $1\text{x}10^{18}/\text{cm}^3$) *InP* / 1000 Å undoped *InP* /
100 Å unstrained $In_{0.53}Ga_{0.47}As$ / 20 Å *InP* / 60 Å $In_{0.53}Ga_{0.47}As$ /
3000 Å undoped *InP* / *p* doped (~ $1\text{x}10^{18}/\text{cm}^3$) *InP*

Structure 2 shown in Figure 4: *n* doped (~ $1\text{x}10^{18}/\text{cm}^3$) *InP* / 1000 Å undoped *InP* /
60 Å unstrained $In_{0.53}Ga_{0.47}As$ / 20 Å *InP* / 100 Å $In_{0.53}Ga_{0.47}As$ /
3000 Å undoped *InP* / *p* doped (~ $1\text{x}10^{18}/\text{cm}^3$) *InP*

The *n* and *p* type dopings outside the active region result in a bandedge energy difference across the structure of about 1.25 eV which is equivalent to an electric field of approximately 30 kV/cm. The electric field can be modified by the application of external bias to the structure.

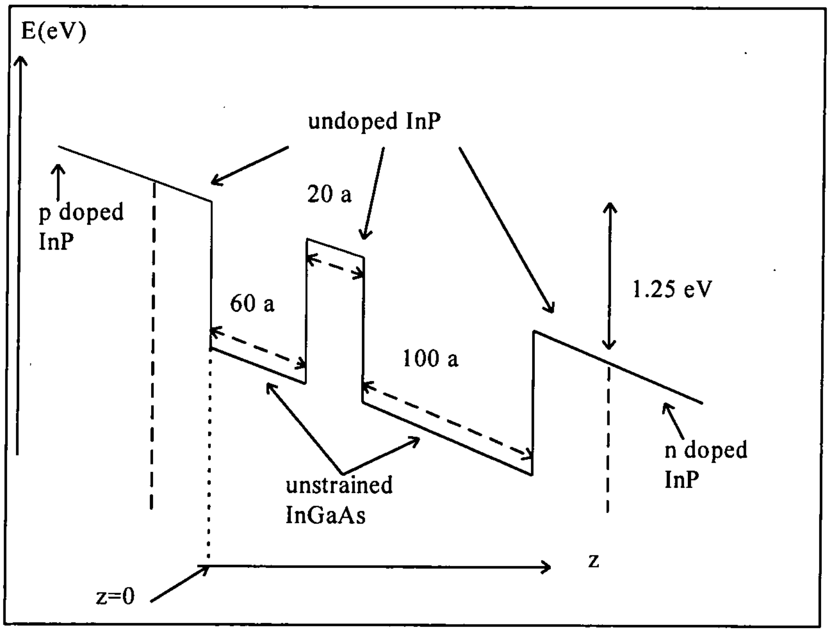

Figure 3: *Structure 1 at zero bias. The n and p type dopings outside the active region result in a band edge energy difference across the structure of 1.25 eV which is equivalent to an electric field of* $3x10^4$ *V/cm.*

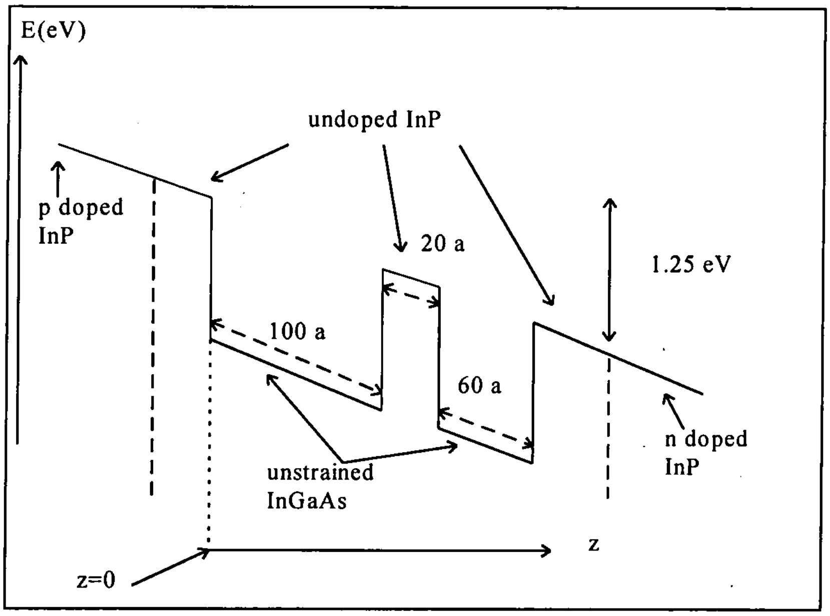

Figure 4: *Structure 2 at zero bias. The n and p type dopings outside the active region result in a band edge energy difference across the structure of 1.25 eV which is equivalent to an electric field of* $3x10^4$ *V/cm.*

Each structure was divided into nine layers (20 angstroms wide) for the purposes of calculating the electronic states using the method described in Section 3.2. The bandstructure was calculated for three different internal electric fields namely 30, 72 and 150 kV/cm, equivalent to 0, 1.75 and 5 V reverse bias respectively. The material parameters and the band offsets used to calculate the bandstructure are shown in Appendix 2. Room temperature absorption spectra were calculated for each structure using eq.(129) from Chapter 2. A broadening energy $\Gamma = 3$ meV was used for all spectral calculations [17,33,59,60]. The calculated spectra for Structures 1 and 2 are shown in Figure 6.

At zero bias an absorption shoulder appears for both structures at a wavelength of approximately 1.51 μm. For both structures the feature shifts to longer wavelengths with increasing bias, and the magnitude of the absorption coefficient decreases with increasing bias [1,2,7-14]. The wavelength shift of the absorption shoulder versus applied bias is depicted in Figure 5.

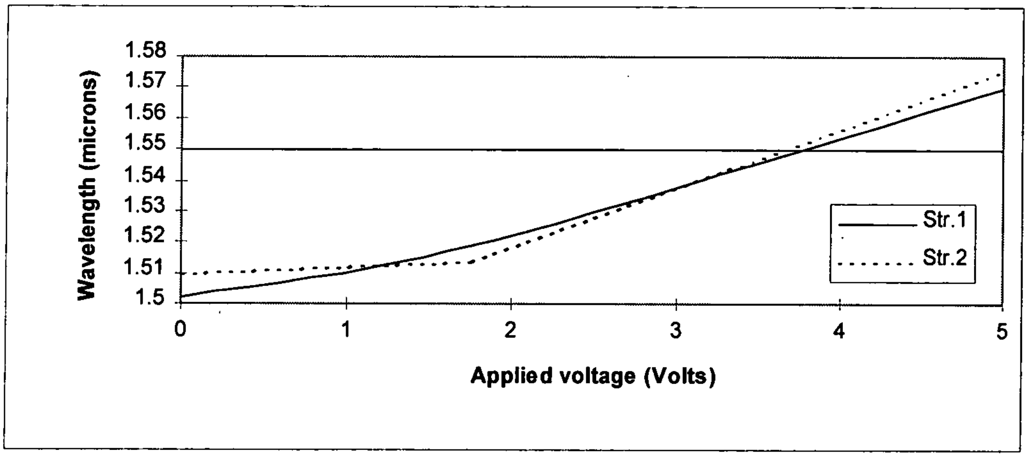

Figure 5: *The calculated wavelength shift of the absorption shoulder for Structures 1 and 2 versus applied field.*

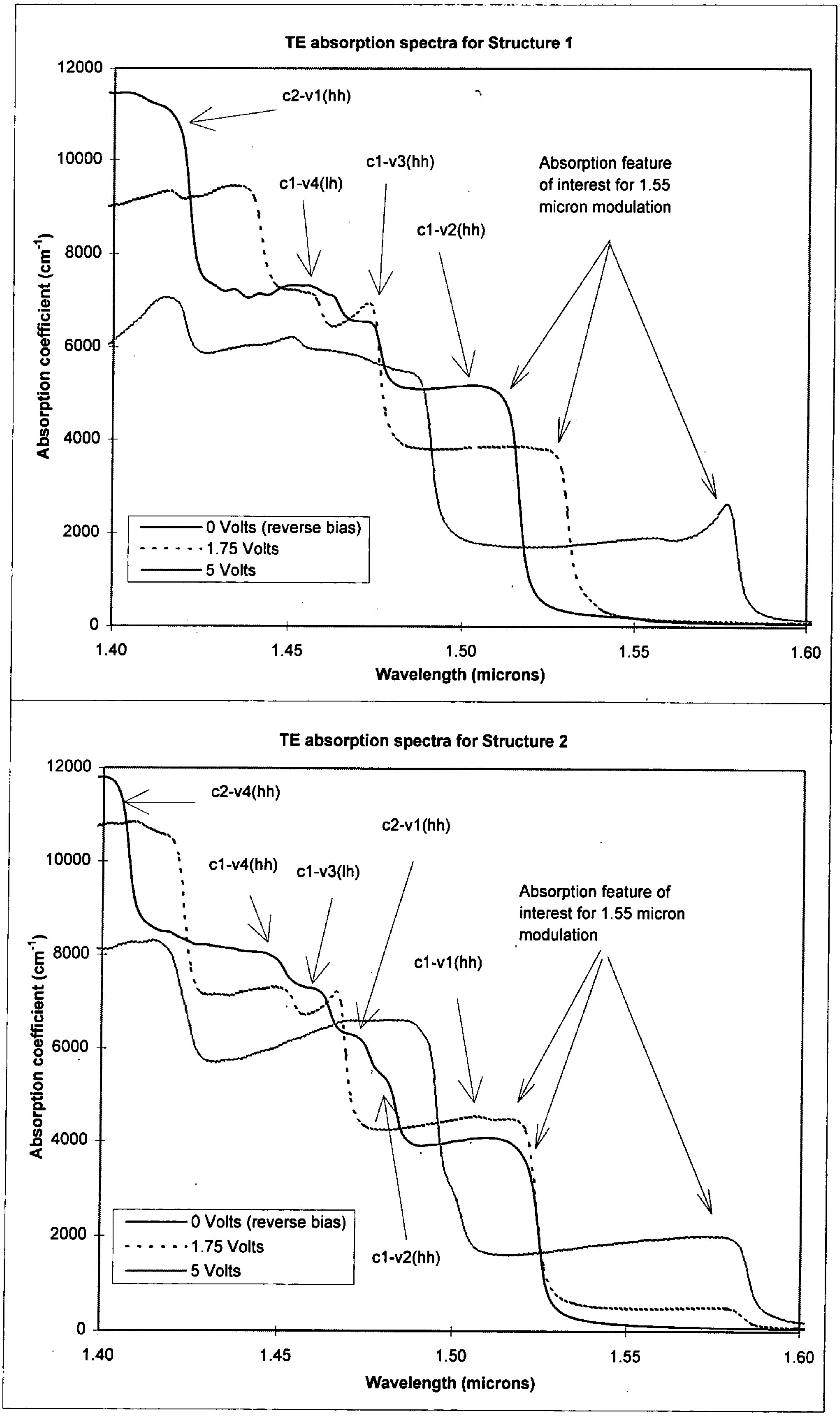

Figure 6: *Room temperature absorption spectra, calculated from the bandstructure and optical matrix elements generated using the* ***k.p*** *model, for Structures 1 and 2 for three values of applied bias.*

The absorption shoulder is at 1.55 μm at a bias of 3.7 V in both structures. Figure 7 shows the absorption coefficient as a function of bias at 1.55 μm. At 3.7 V the absorption coefficient is in excess of 10^3 cm^{-1} and is approximately 10% larger for Structure 2. At 5 V the absorption is virtually identical for both structures and has increased by a factor of 10 compared to the zero bias value.

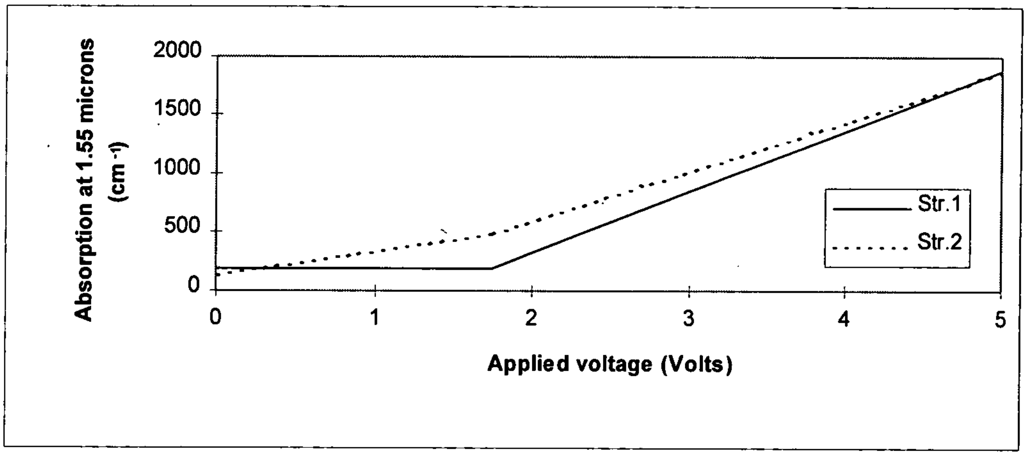

Figure 7: *The calculated change in the absorption coefficient at 1.55 μm for Structures 1 and 2 versus applied field.*

Both structures provide a potential modulation mechanism for light at 1.55 μm. At 3.7 V the absorption at 1.55 μm has increased by a factor 6 for Structure 1 and by a factor of 9 for Structure 2. Structure 2 has a better low voltage performance but the responses are virtually indistinguishable at 5 V.

In subsequent sections this behaviour is examined in terms of bandstructure, wave functions, optical matrix elements and joint densities of states.

3.4 Bandstructure and wave functions for Structures 1 and 2

The bandstructure and wave functions, for the three applied voltages, were calculated using the method described in Section (3.2). The four lowest conduction subbands, for Structures 1 and 2, are shown in Figure 8. At $k_{\|}=0$ the subbands exist in degenerate pairs but split for $k_{\|}\neq 0$ due to the lack of inversion symmetry in the quantum well structure. The splitting is small (~ 12 meV at $k_{\|}=0.07$ $\mathring{A}^{-1}$ with 5 V bias) and the discussion below considers the subbands as (near degenerate) pairs. The shift in the subband energies with increasing electric field are shown in Figure 9. As the applied electric field is increased the band energies decrease due to the tilting of the bandedge apparent in Figures 3 and 4 - this is the quantum confined stark effect (QCSE) [2,25,26].

The energy separation of the two subbands, for Structure 1, increases with increasing field. This can be understood by reference to Figure 10 and noting that the states of the lower conduction subband pair (c1) are localised in the wider (100 angstrom) well whilst those of the second subband pair (c2) are largely localised in the narrower (60 angstrom) well. The shift in energy, which is approximately porportional to the well width in question, is larger for c1 resulting in an increased energy separation of the two subbands with increasing field. The shift in energy for c1 in Figure 9 is essentially linear across the full range of applied voltage whilst the energy variation of c2 has a change in slope at approximately 1.5 V due to the field induced reduction of the 20 angstrom barrier between the layers and the resulting lower confinement.

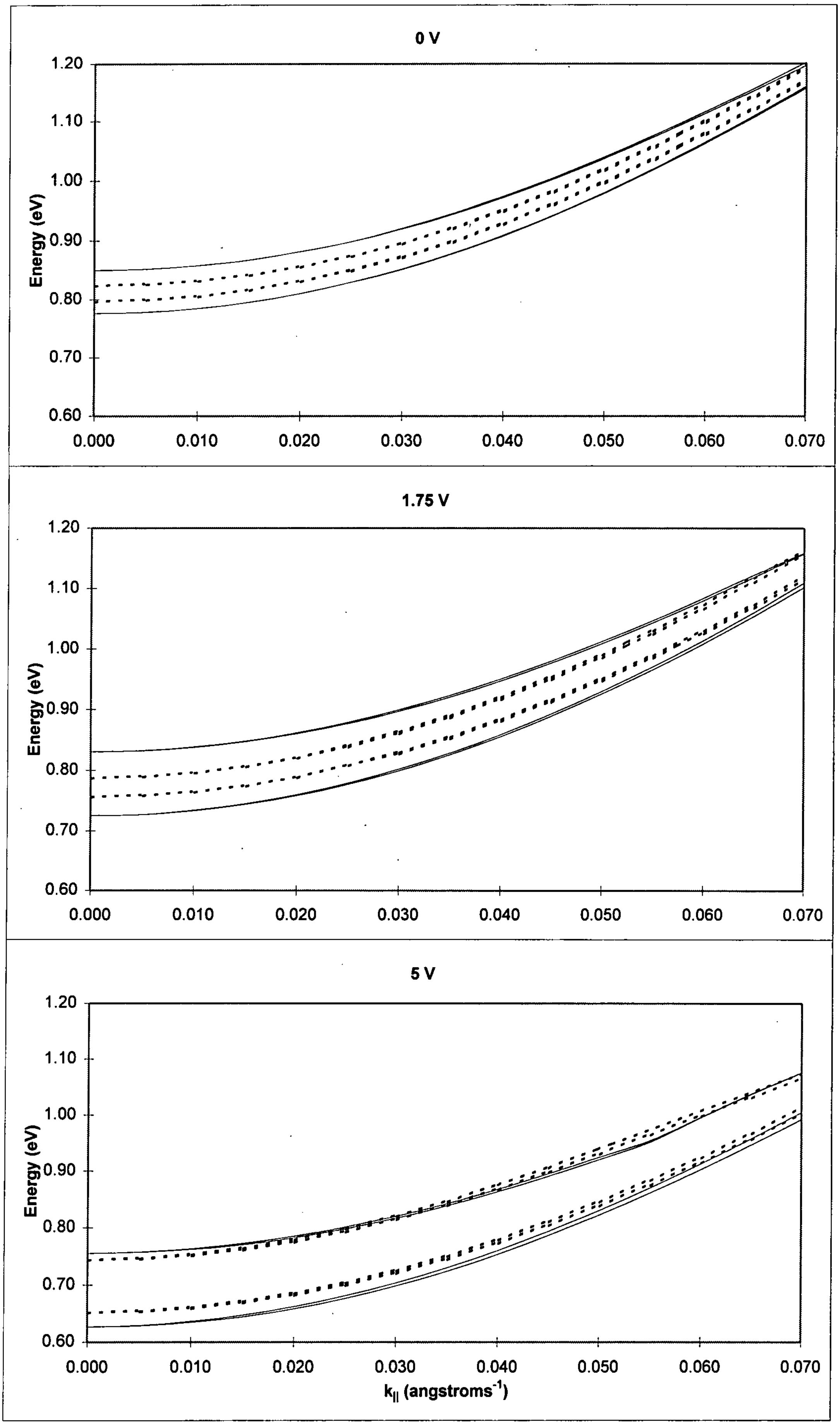

Figure 8: *Conduction bandstructure for Structures 1 (solid lines) and 2 (dotted lines) calculated using the* ***k.p*** *model for three values of applied bias.*

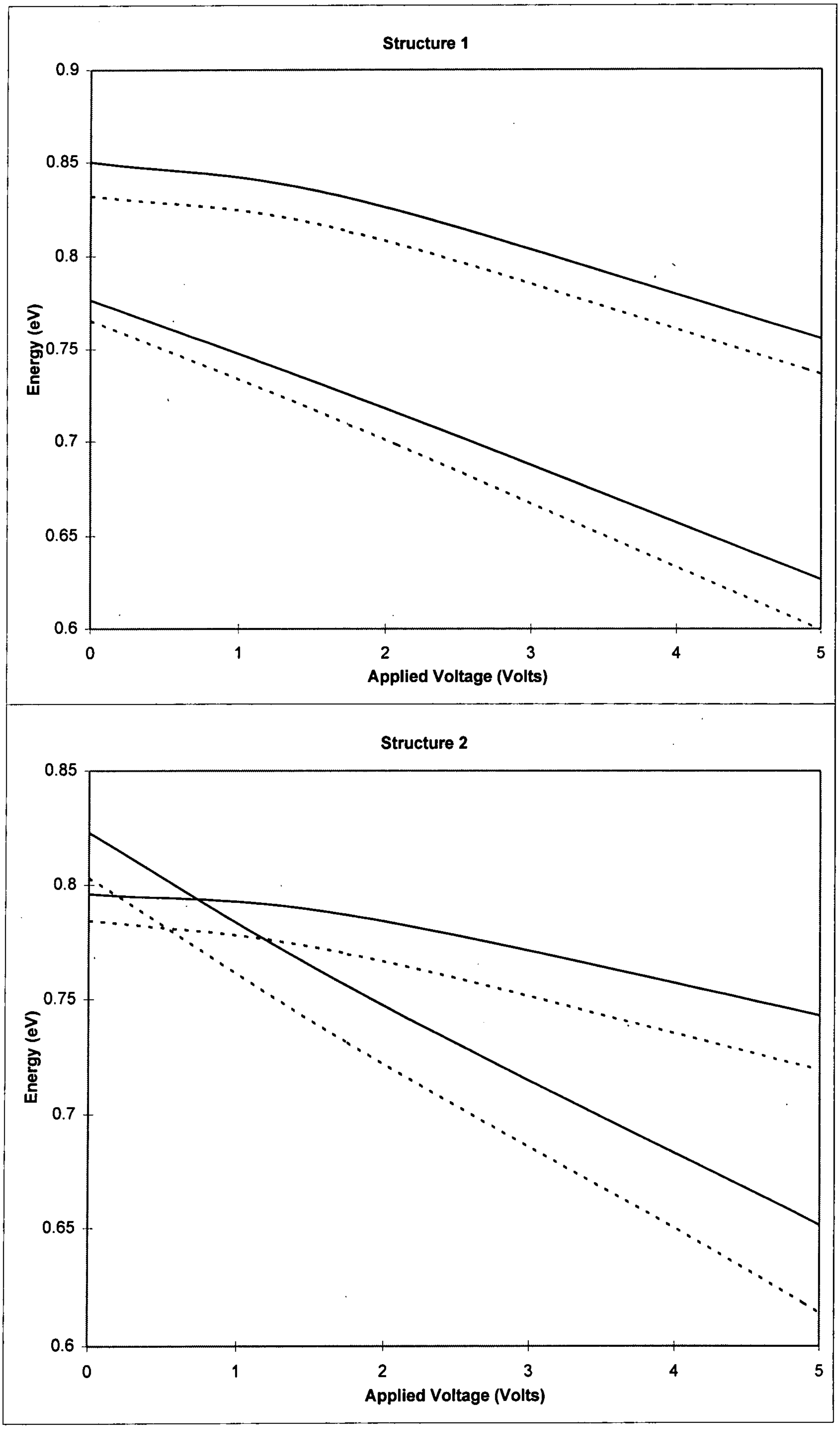

Structure 1

Structure 2

Figure 9: *Shift in conduction subband energies with increasing bias at $k_{||}=0$, for* ***k.p*** *(solid lines) and one-dimensional effective mass results (dotted lines) versus applied bias.*

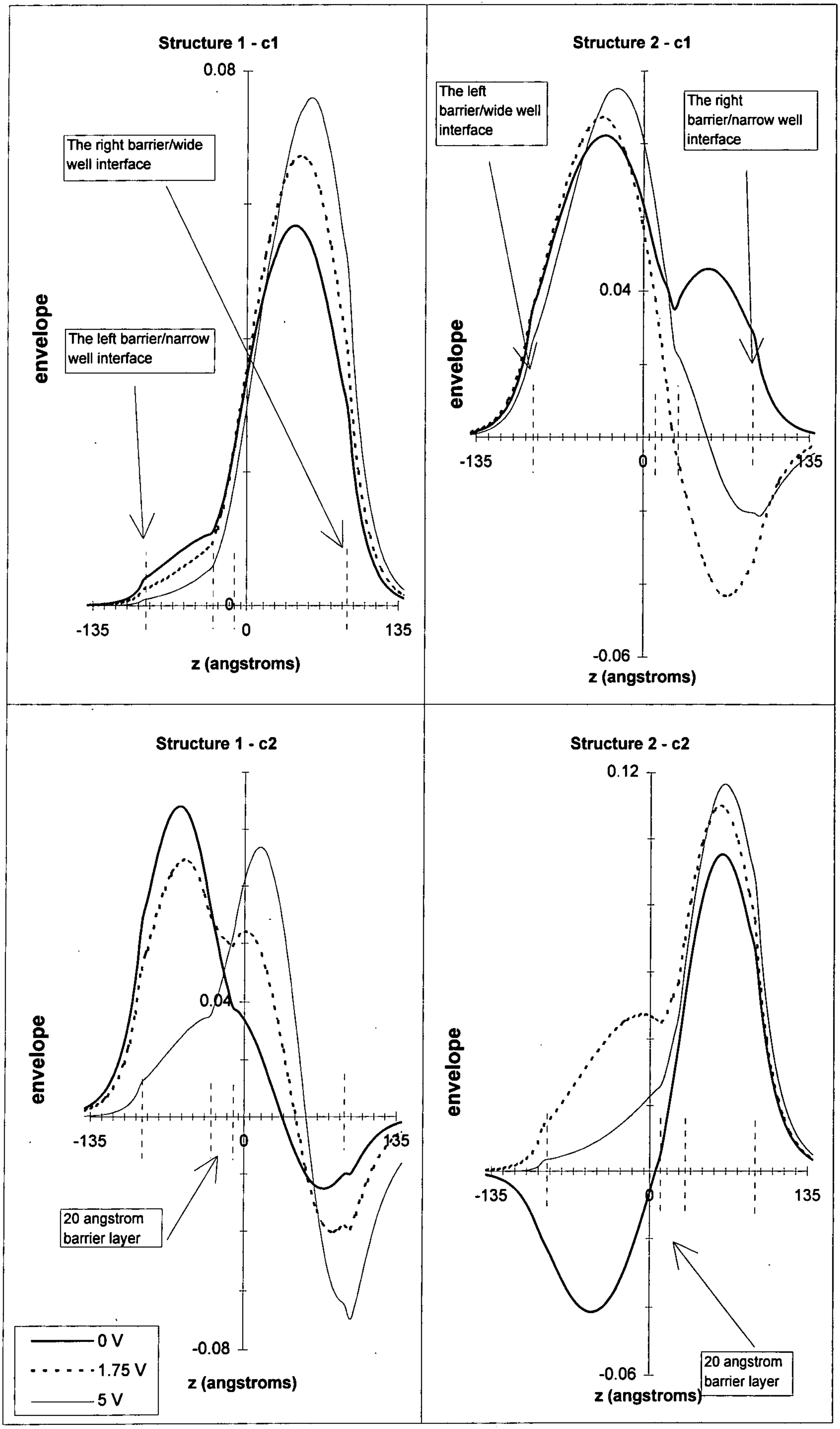

Figure 10: *Evolution of the two lowest conduction envelope functions (real part), for Structures 1 and 2 at* $k_{||}=0$*, with increasing bias calculated using the* ***k.p*** model.

The shift in energy is now due to barrier penetration as well as the tilting of the band edge. As the applied field is increased further the shift in energy of c2 begins to resemble that of c1 since c2 penetrates further into the wider well and begins to behave as the first excited state of this well [4,14,16,17,18]. The shifts in subband energies calculated using the one-dimensional effective mass model show good agreement with the results obtained from the ***k.p*** model and are also depicted in Figure 9. The electric field induced change in the envelope functions for c1 and c2, calculated using the ***k.p*** and the one-dimensional effective mass models, are depicted in Figures 10 and 11 respectively and show good agreement.

The two lowest conduction subband pairs for Structure 2 are shown in Figure 8. As for Structure 1 the conduction subbands decrease in energy with increasing field. However, at approximately 0.75 V, the energy of c2 (mainly localised in the narrow well) falls below c1 (mainly localised in the wide well). The energy separation between c1 and c2 increases for further increases in electric field. This behaviour is shown in Figure 9. The lowest energy subband, c1, has a change in slope at approximately 1.5 V due to the field induced reduction of the 20 angstrom barrier between the layers and the resulting lower confinement. The one-dimensional effective mass results show similar behaviour and are also depicted in Figure 9. The envelope functions for c1 and c2 are shown in Figure 10. At zero bias c1 and c2 have similar energies and both envelope functions are delocalised across the structure, although c1 is slightly more confined in the wide well and c2 in the narrow well. In essence, c1 is the symmetric state and c2 the anti-symmetric state of the near resonant pair. At 1.75 V, the conduction states still show resonance behaviour but since they have changed their relative energy positions c1 is now anti-symmetric whilst c2 is symmetric. At 5 V, the resonance effect is lost and c1 has a strong tail in the narrow well while still mainly confined to the wide well. c2 is still strongly localised in the narrow well. The one-dimensional effective mass envelope functions for c1 and c2 are shown in Figure 11 and are in good agreement with those calculated using the ***k.p*** model (see Figure 10).

Figure 12 shows the valence bandstructure at three values of applied bias for Structure 1. As with the conduction band the lack of inversion symmetry means that degenerate pairs of subbands at $k_{\|}=0$ are split elsewhere. Again the subbands are considered in (near degenerate) pairs in the discussion below. The bandedge energies are pushed down in energy (corresponding to an increase in hole energy) with increasing applied electric field and the overall separation of the bands increases [1,2,7,18]. The evolution of the band structure is complicated by the fact that both heavy hole and light hole bands are present and each state is either confined in the narrow or the wide well. In Table 1 the character of each band and its localisation (narrow well (L) or wide well (R)) is specified. The energy shift induced by the electric field for states localised in the narrow well is generally smaller than for those localised in the wider well, therefore the bands cross as the electric field is increased. In the absence of electric field the highest valence subband (that is the one with the lowest hole energy) would be of heavy hole character and localised in the wide well, but the built-in field at zero bias is sufficient to move this below the heavy hole

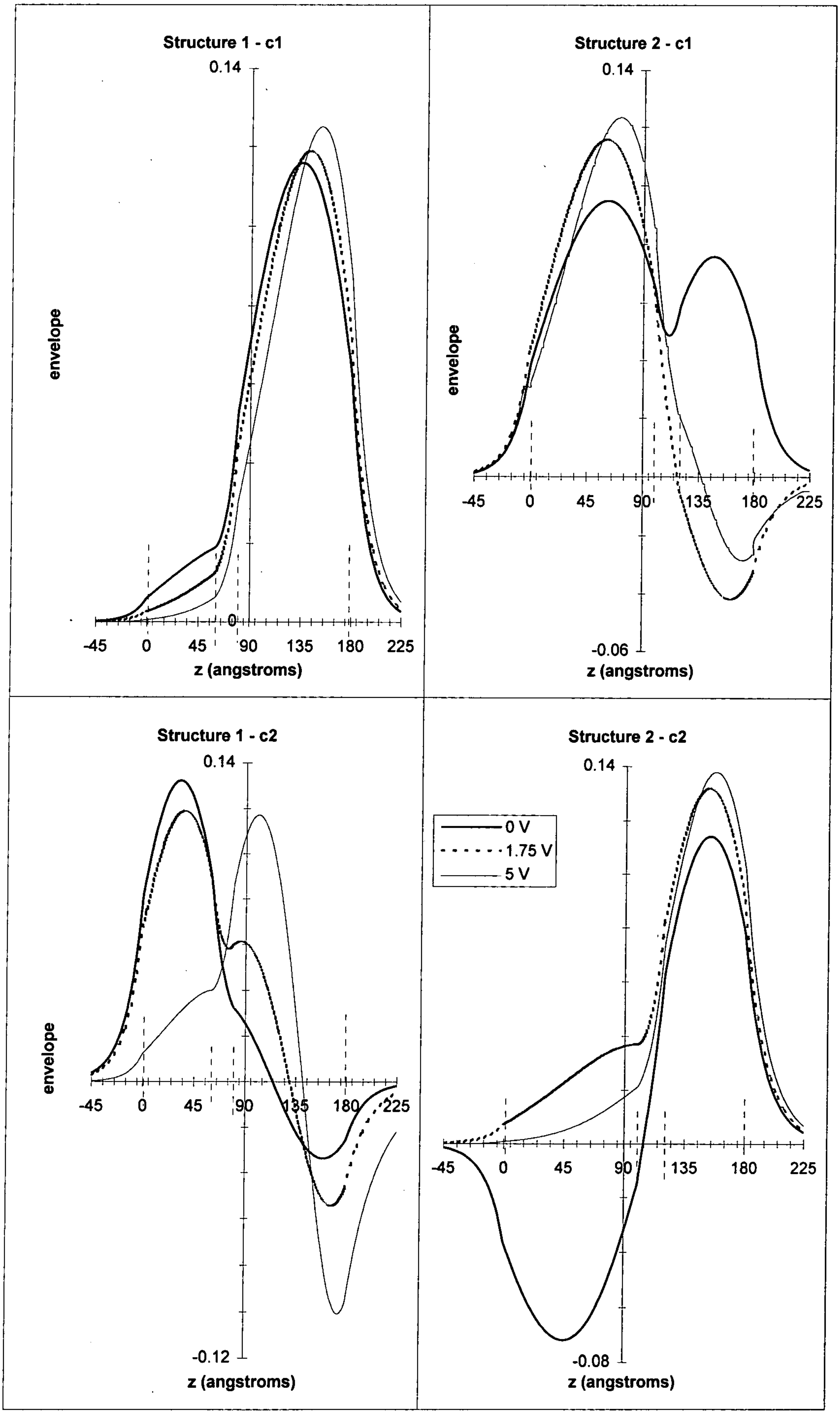

Figure 11: *Evolution of the two lowest conduction envelope functions (real part), for Structures 1 and 2 at* $k_{||}$*=0, with increasing bias calculated using the one-dimensional effective mass model.*

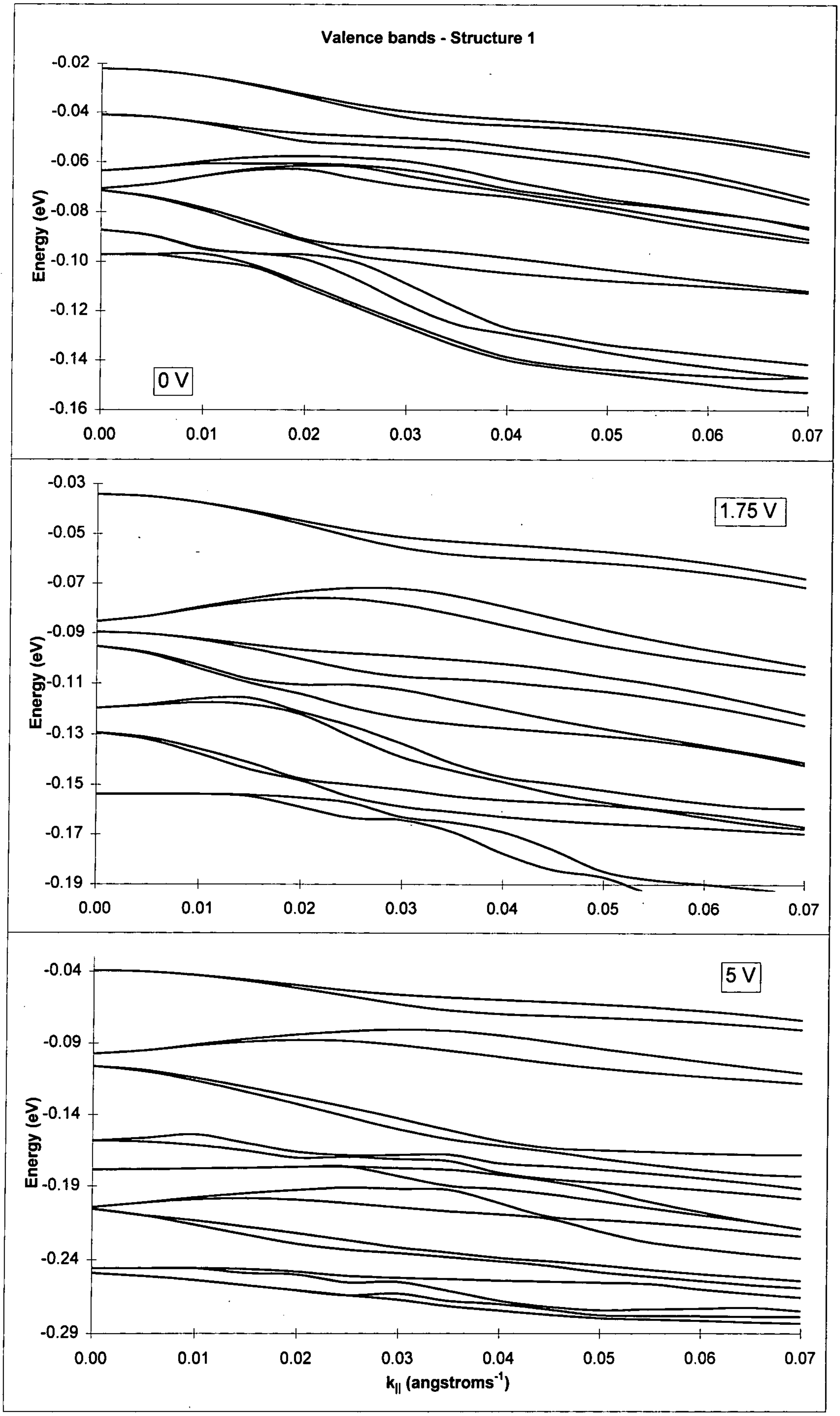

Figure 12: *Valence bandstructure for Structure 1 for three values of applied bias, calculated using the* ***k.p*** *model.*

subband localised in the narrow well. The movement of the subbands with increasing electric field is shown in Figure 13. It is immediately apparent that there are two distinct sets of curves, each broadly exhibiting similar behaviour.

0 Volts	1.75 Volts	5 Volts
1 - heavy hole (L)	1	1
2 - heavy hole (R)	3	4
3 - heavy hole (R)	5	7
4 - light hole (R)	6	6
5 - heavy hole (L)	2	2
6 - light hole (L)	4	3
7 - heavy hole (R)	7	8

Table 1: *The entries are interpreted as v1 (at 0 V) remains as highest valence subband for all values of applied bias considered, whereas v2 (at 0 V) becomes the third highest valence subband at 1.75 V and the fourth highest at 5 V.*

Three subband pairs show very little change in energy with increasing field and are found to be the states confined to the narrow well (v1, 5 & 6 in the zero bias column of Table 1). The other subband pairs show a much larger shift in energy with increasing field and the relevant states are confined in the wide well (v2, 3, 4 & 7). These four subband pairs exhibit very similar shifts, irrespective of character, with increasing electric field although subband pairs v3 & 4 cross at 5 V. Figure 13 also shows the shift in subband energies with increasing bias calculated using the one-

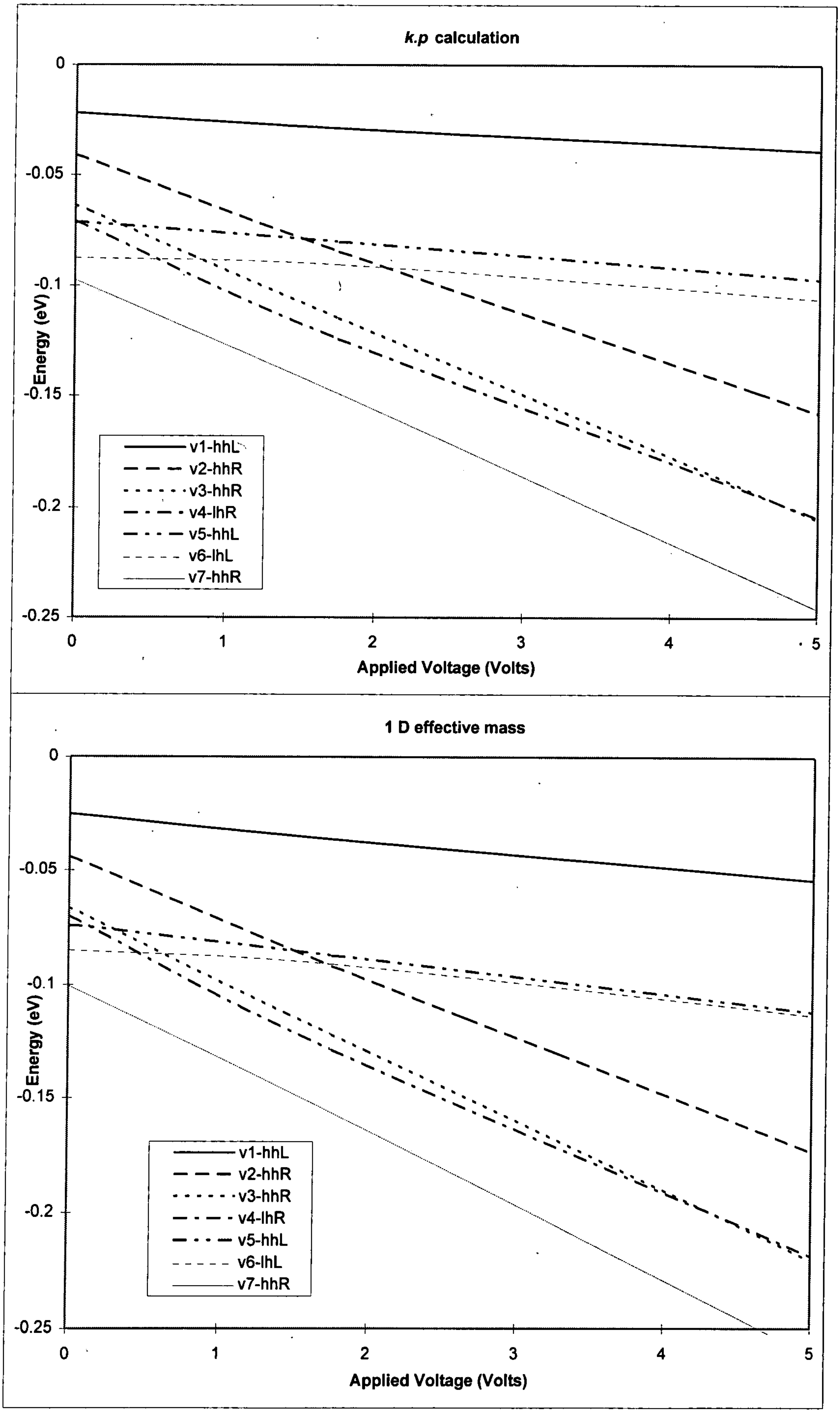

k.p calculation

1 D effective mass

Figure 13: *Shift in valence subband energies with increasing bias for Structure 1, calculated using the* ***k.p*** *and one-dimensional effective mass models.*

dimensional effective mass model. These exhibit almost identical behaviour compared to those calculated using the ***k.p*** model.

Figure 14 shows the evolution of the main character envelope functions for the three highest valence subbands with increasing bias which have been calculated using the ***k.p*** model at $k_{\parallel}$=0. These three envelope functions essentially remained confined in their respective wells, and only lean to the left with increasing bias. Figure 15 shows the same three envelope functions calculated using the one-dimensional effective mass model.

The valence bandstructure for Structure 2 is shown in Figure 16. Table 2 shows the character of each band and its localisation (wide well (L) or narrow well (R)).

0 Volts	1.75 Volts	5 Volts
1 - heavy hole (L)	1	1
2 - heavy hole (L)	2	2
3 - light hole (L)	3	3
4 - heavy hole (R)	5	6
5 - heavy hole (L)	4	4

Table 2: *The entries are interpreted as v1 (at 0 V) remains as highest valence subband for all values of applied bias considered, whereas v4 (at 0 V) becomes the fifth highest valence subband at 1.75 V and the sixth highest at 5 V.*

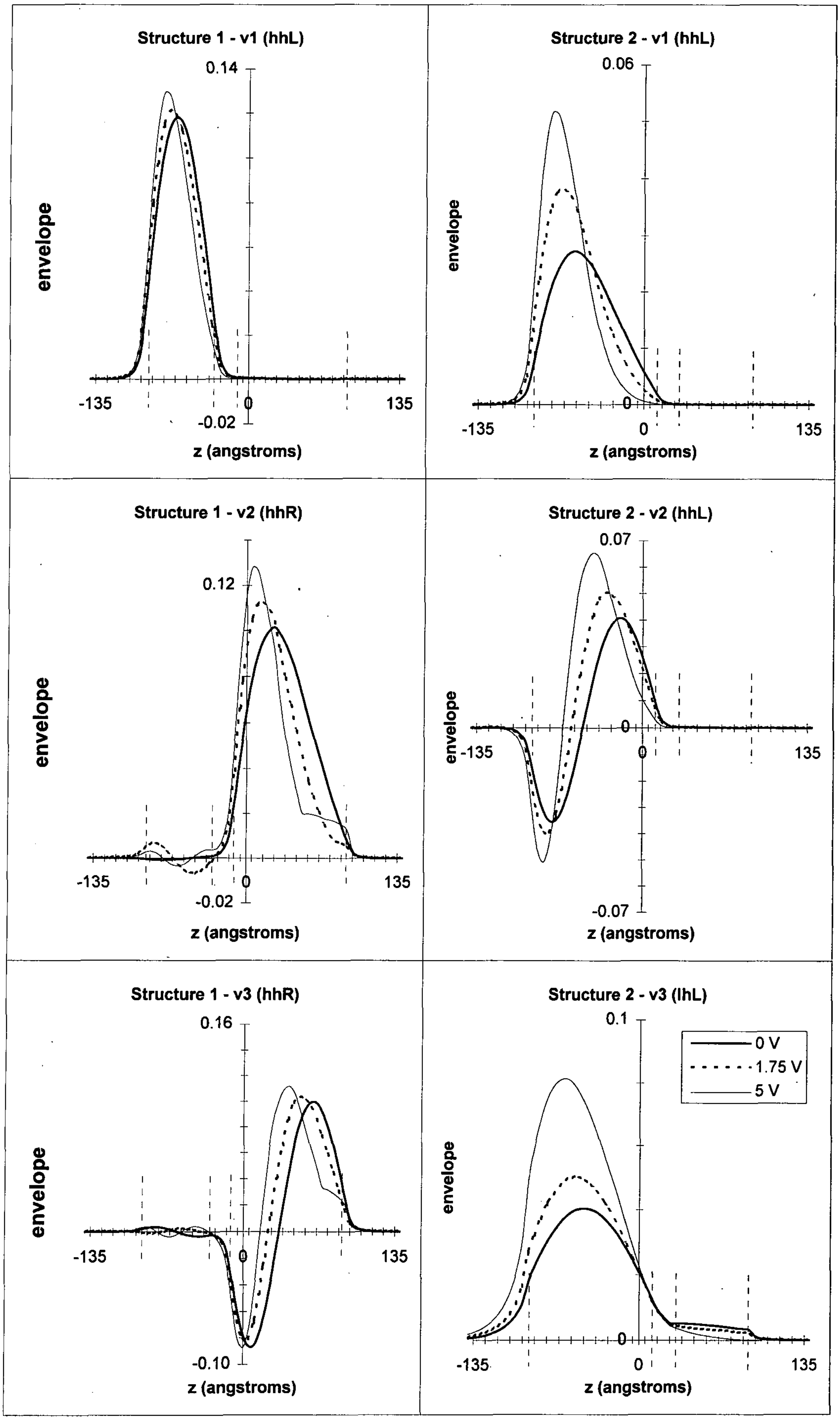

Figure 14: *Evolution of the three highest valence envelope functions (real part) at* $k_{||}=0$*, for Structures 1 and 2, with increasing bias as calculated using the* ***k.p*** *model.*

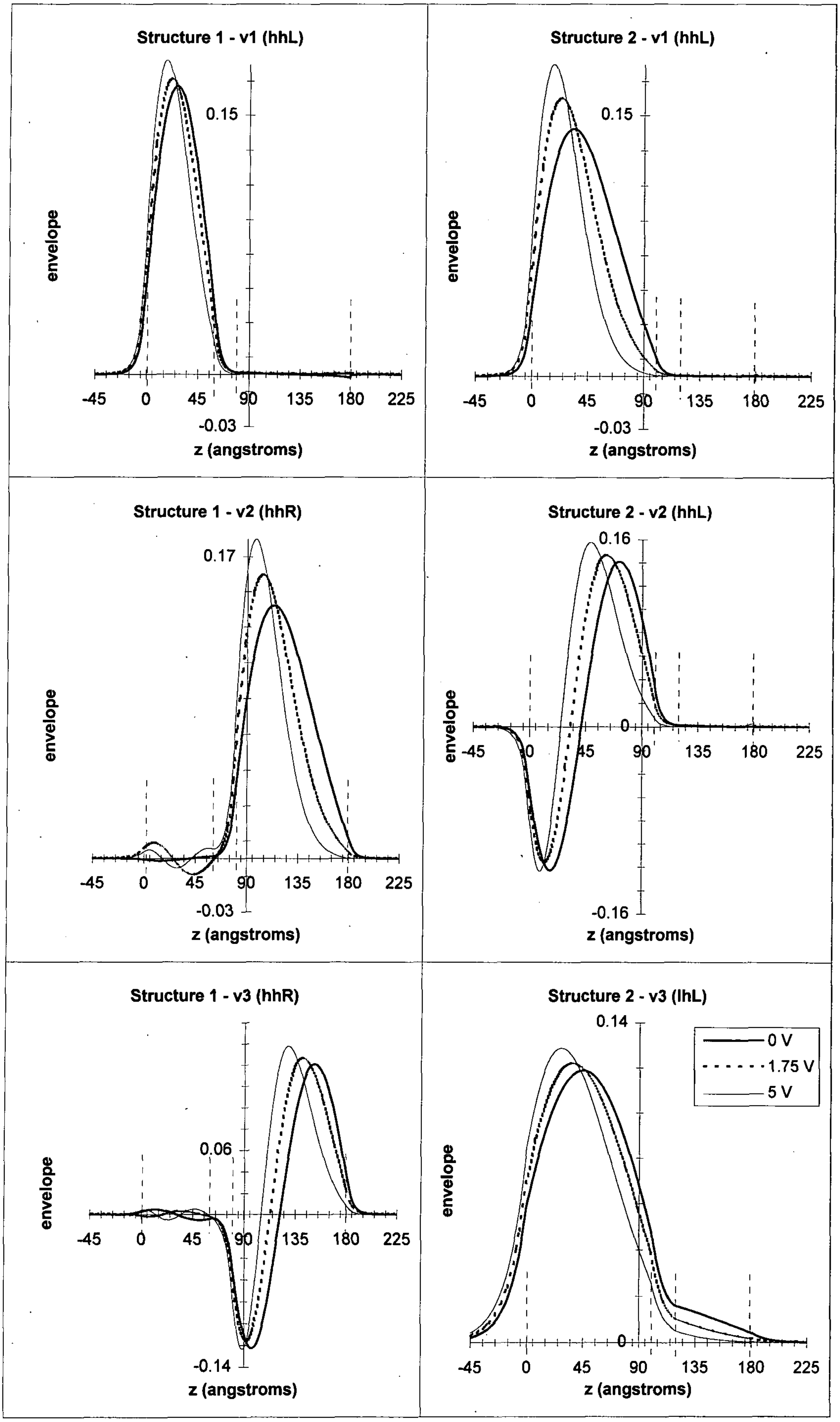

Figure 15: *Evolution of the three highest valence envelope functions (real part) at $k_{||}$=0, for Structures 1 and 2, with increasing bias calculated using the one-dimensional effective mass model.*

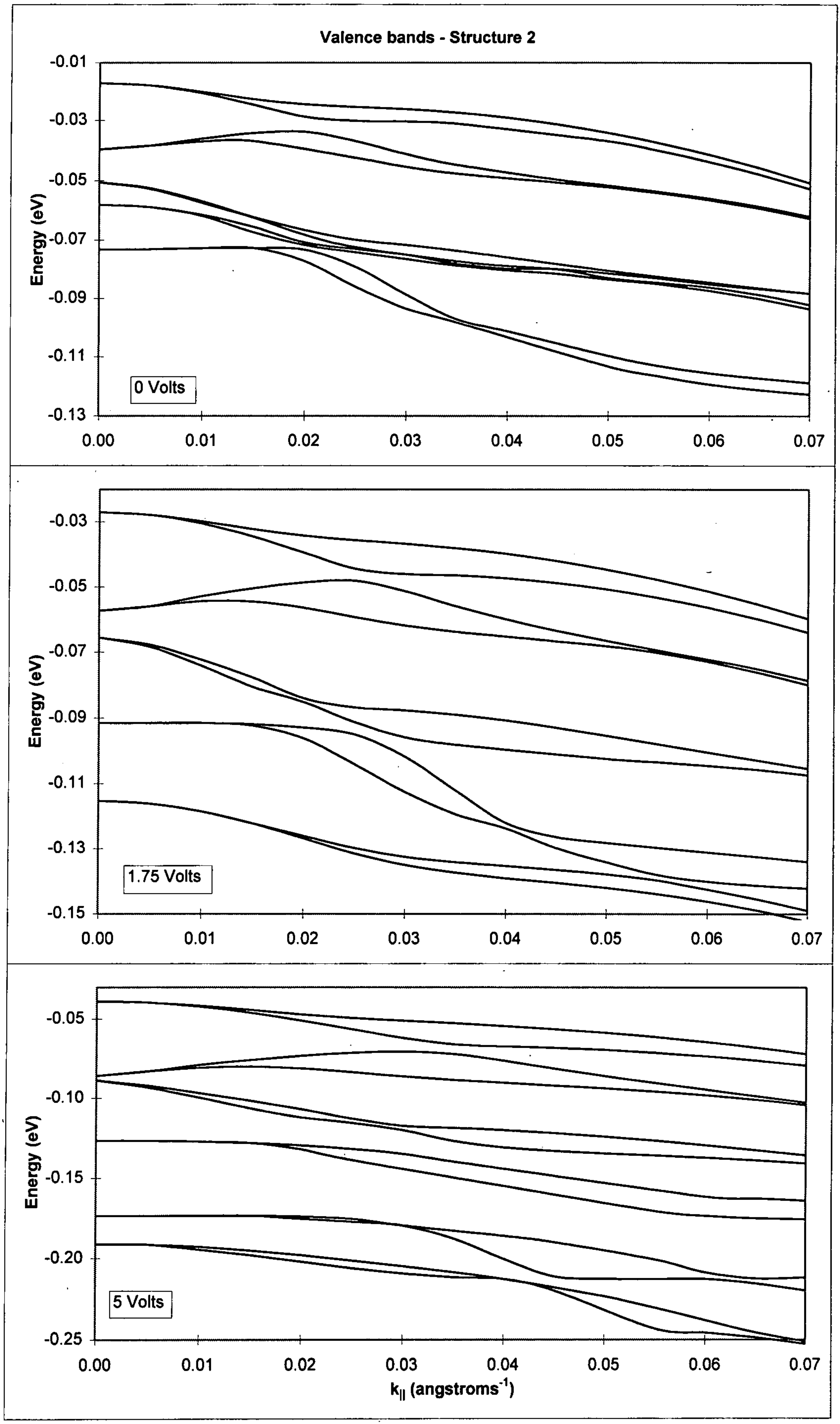

Figure 16: *Valence bandstructure for Structure 2 for three values of applied bias, calculated using the* ***k.p*** *model.*

The shift in the subband energies at zero in-plane wavevector is shown in Figure 17. As for Structure 1, there are two distinct sets of curves each broadly exhibiting similar behaviour. The subband pairs that show little energy shift with increasing bias (v1, 2, 3 & 5) have states localised in the wide well, whereas those that show large shifts (v4) have states localised in the narrow well. The shift in subband energies calculated using the one-dimensional effective mass model is also shown in Figure 17 and shows good agreement with those calculated using the ***k.p*** model.

Figure 14 shows the evolution of the main character envelope functions for the three highest valence subbands with increasing bias which have been calculated using the ***k.p*** model at $k_{||}$=0. Unlike the equivalent states for Structure 1, these show a more pronounced shift with increasing bias. All three envelope functions, depicted in Figure 14, are localised in the wide well, and increasing bias causes a more pronounced shift to the left of this well.

3.5 Optical matrix elements for Structures 1 and 2

Figure 18 shows the variation with applied voltage in the squared magnitude of the optical matrix elements between states at $k_{||}$=0 calculated using the ***k.p*** model for Structure 1. The matrix elements are for TE mode of the radiation (electric field polarized in the plane of the well) and the magnitude squared is averaged over the four transitions between degenerate pairs of states at $k_{||}$=0.

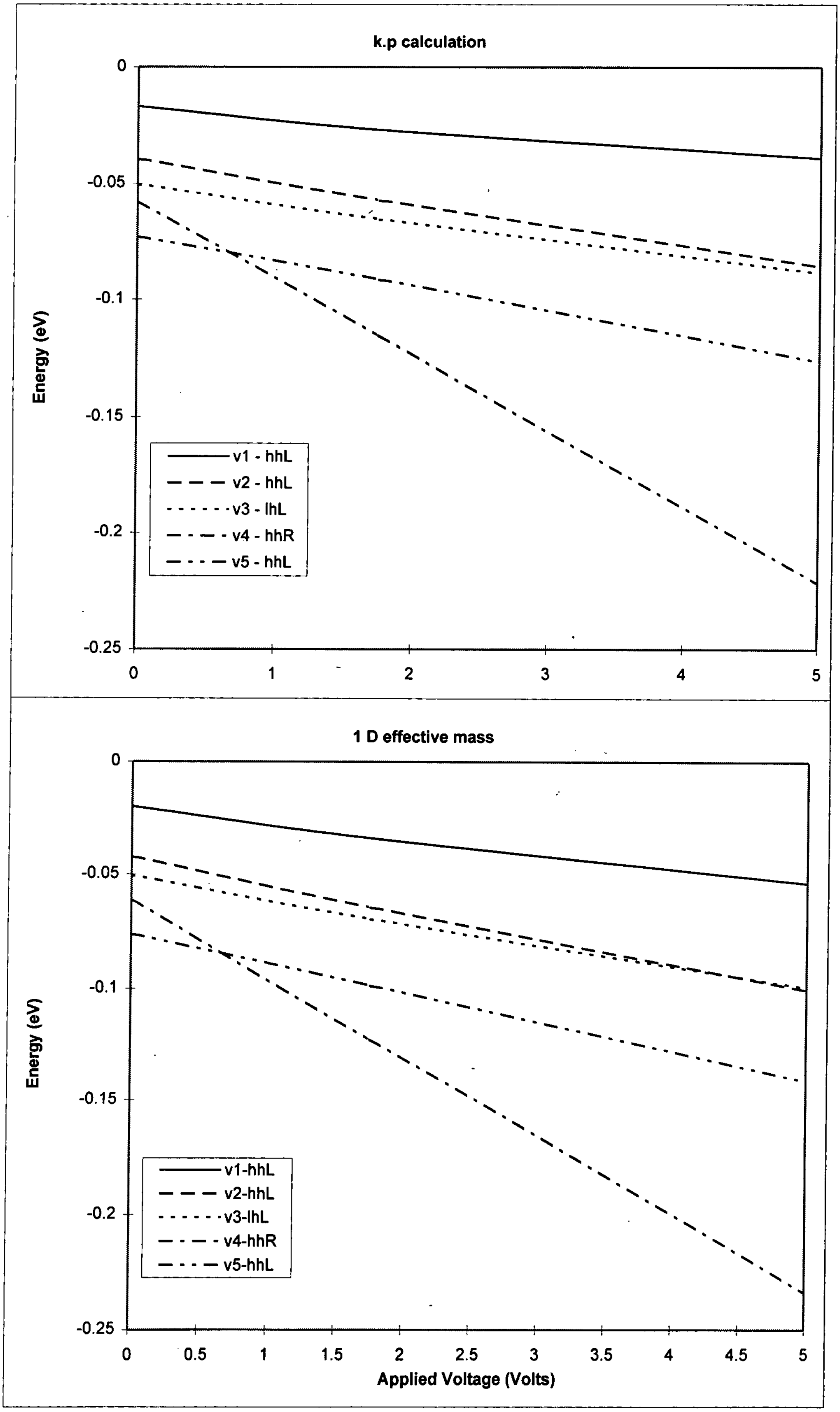

Figure 17: *Shift in valence subband energies with increasing bias for Structure 2, calculated using the* ***k.p*** *and one-dimensional effective mass models.*

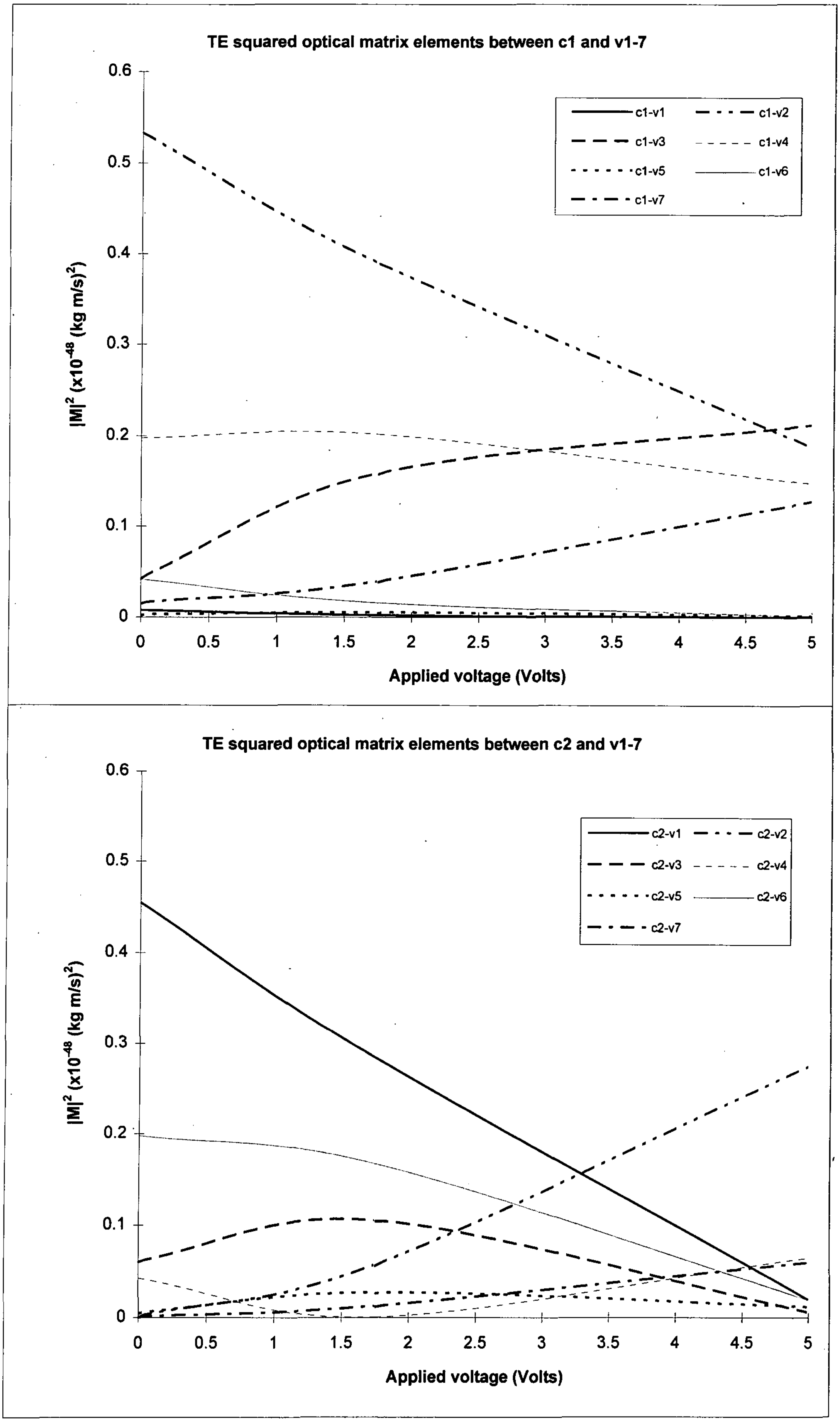

Figure 18: *The variation of the TE squared optical matrix elements with applied bias for Structure 1 calculated using the* ***k.p*** *envelope functions at* $k_{||}=0$.

At zero bias the matrix elements between c1 and v1-7 broadly fall into three behavioural groups. The largest matrix elements, c1-v2(hh) and c1-v4(lh), are between conduction and valence states confined in the wide well and are parity allowed. These matrix elements decrease with increasing bias due to increasing localisation on opposite sides of the well of the conduction and valence states. The matrix elements for c1-v1 and c1-v5 are small since the valence states are confined in the narrow well whilst conduction state is confined to the wide well. The overlap of the conduction and valence states is also reduced by increased bias. The matrix elements for c1-v3 and c1-v7 are small, despite being localised in the wide well, since these transitions are parity forbidden. However, these matrix elements increase with bias [8-9,20-24,28] which can be understood with reference to Figures 10 and 14. The conduction state, c1, localises to the right of the wide well with increasing bias whilst the valence state, v3, localises to the left of the wide well. The envelope function overlap between these two states begins to resemble a parity allowed transition with increasing bias resulting in an increase of the matrix element.

The matrix elements between c2 and v1-7 behave in a similar manner to those between c1 and v1-7 and also show the three behavioural groups. Figure 19 shows the variation with applied voltage in the squared magnitude of the optical matrix elements between states at $k_{\|}=0$ calculated using the one-dimensional effective mass model, and shows good agreement between the ***k.p*** and effective mass models at $k_{\|}=0$.

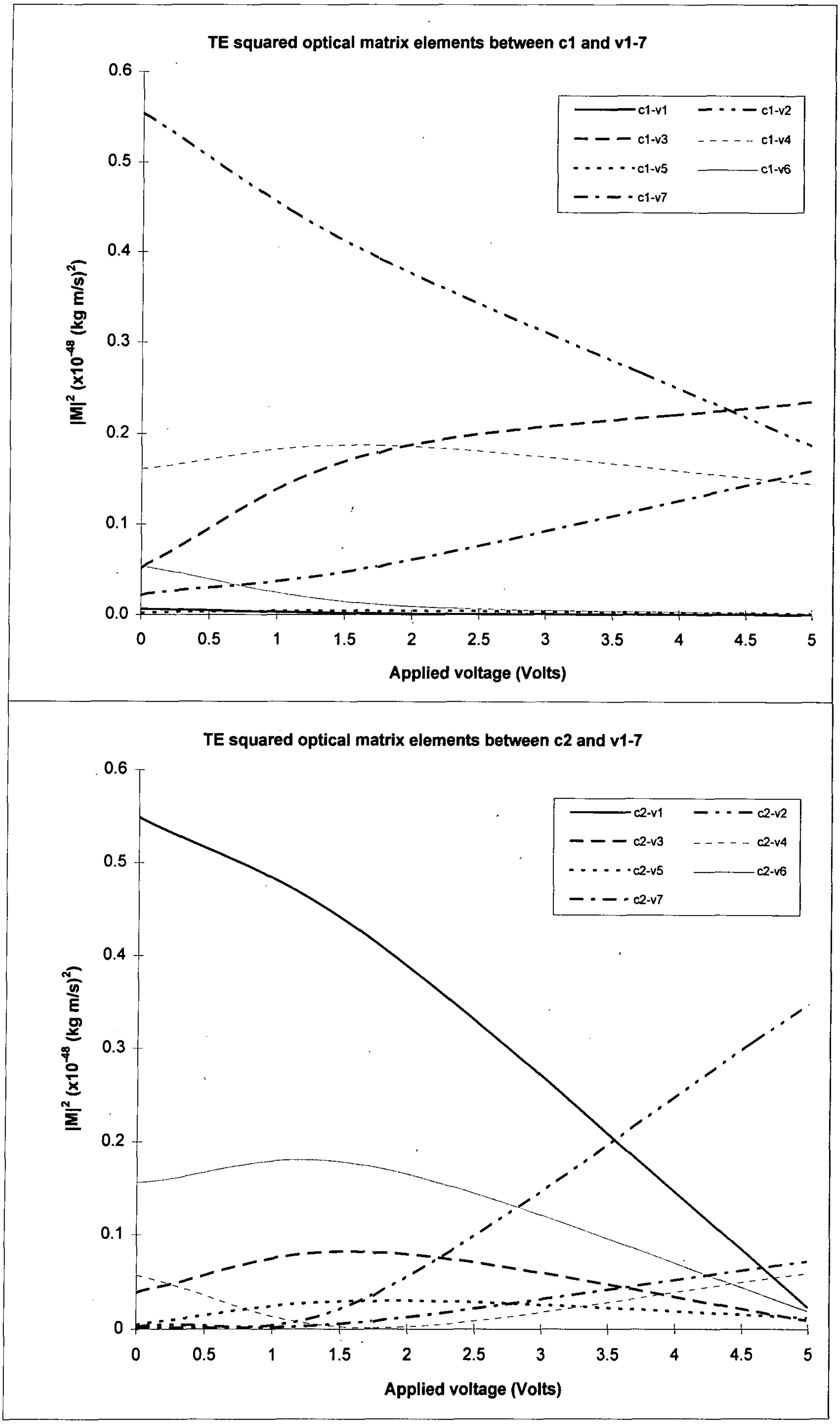

Figure 19: *The variation of the TE squared optical matrix elements with applied bias for Structure 1 calculated using the one-dimensional effective mass envelope functions at* $k_{||}=0$.

Figure 20 shows the variation with applied voltage in the squared magnitude of the optical matrix elements between states at $k_{||}=0$ calculated using the ***k.p*** model for Structure 2. At zero bias the matrix elements between c1 and v1-5 broadly fall into three behavioural groups, as already seen for Structure 1. The matrix elements for c1-v1 and c1-v3 are large at zero bias since they are localised in the wide well. They decrease with increasing bias due to localisation to different sides of the well. The matrix element for c1-v4 is small since c1 is generally localised in the wide well whilst v4 is localised in the narrow well. This matrix element also decreases with increasing bias. The matrix elements for c1-v2 and c1-v5 are parity forbidden and are small at zero bias. However, these matrix elements increase with increasing bias for the same reason as described for similar parity forbidden transitions for Structure 1.

The matrix elements between c2 and v1-5 are shown in Figure 20. The matrix element c2-v4 is the only significant transition and remains almost constant for the full range of applied bias considered. As shown in Figure 10 the part of envelope function c2 residing in the narrow well does not shift much with increasing bias. The envelope function for v4 remains strongly confined in the narrow well and it also does not shift appreciably with increasing bias resulting in an almost constant overlap between the respective envelope functions. The remaining matrix elements are small since the v1,2,3 & 5 envelope functions are localised in the wide well, whilst c2 is localised in the narrow well. The overlap between these valence states and c2 is small at zero bias and decreases with increasing bias. Figure 21 shows the matrix elements calculated using the one-dimensional effective mass envelope functions. These agree

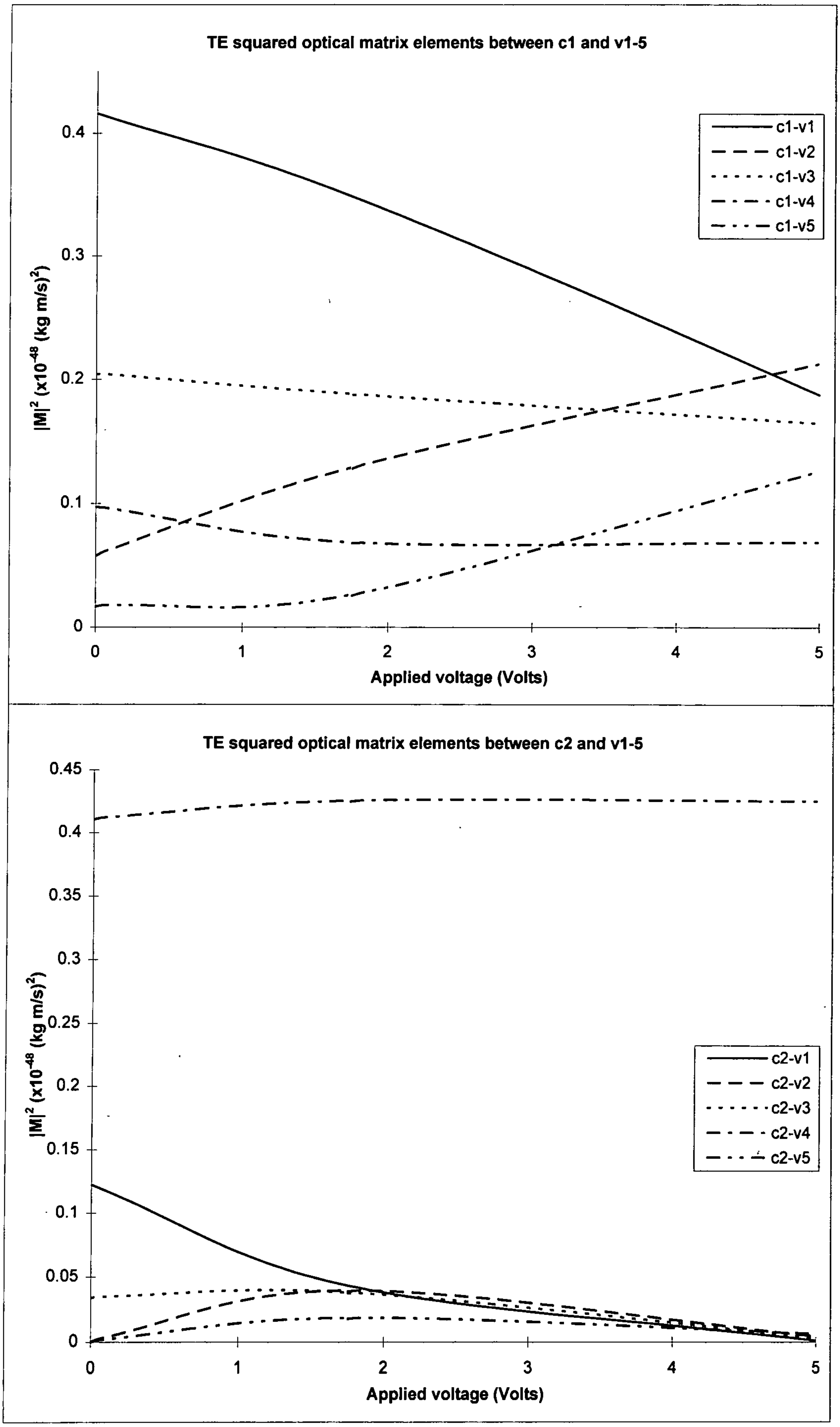

Figure 20: *The variation of the TE squared optical matrix elements with applied bias for Structure 2 calculated using the* ***k.p*** *envelope functions at* $k_{||}$*=0.*

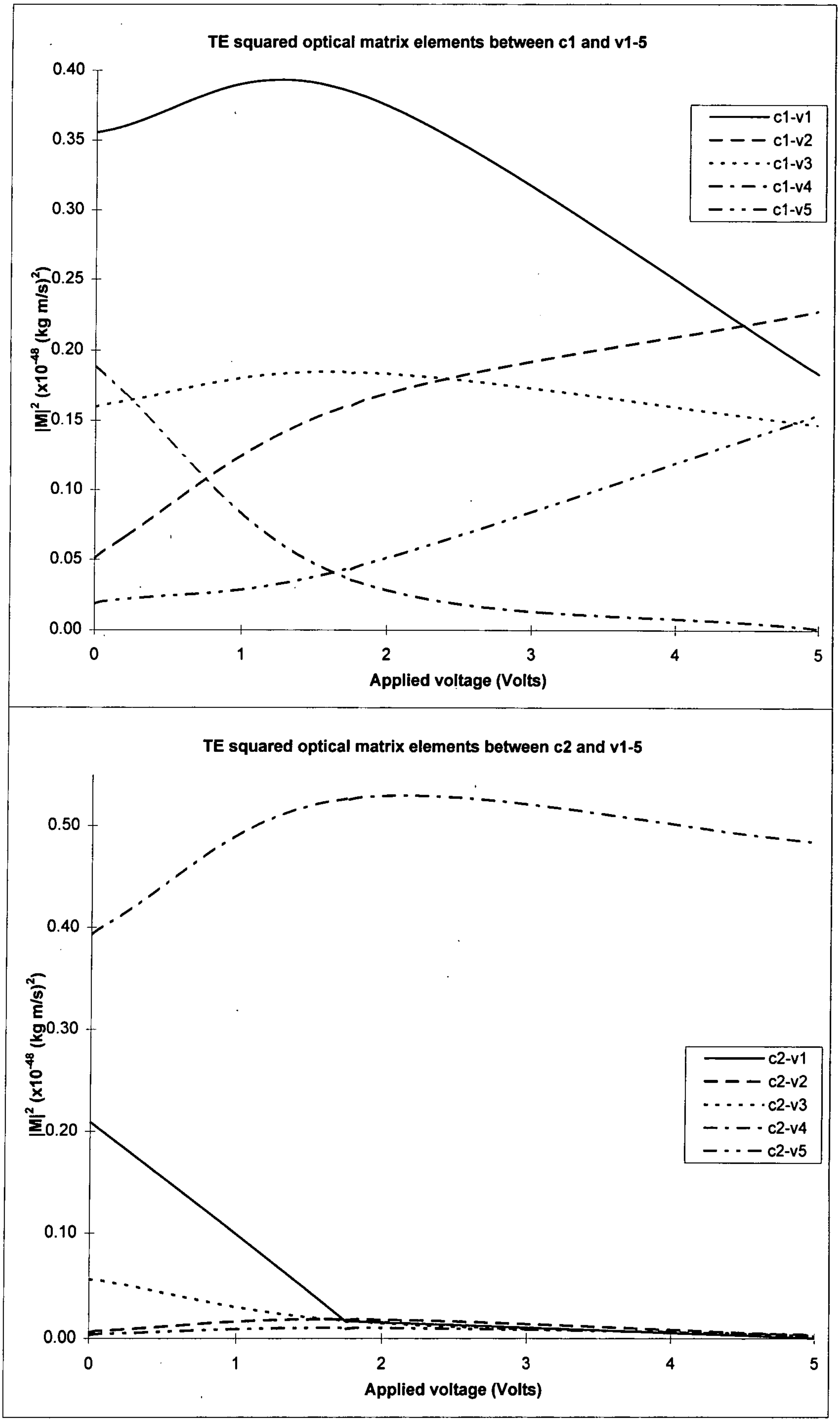
TE squared optical matrix elements between c1 and v1-5

TE squared optical matrix elements between c2 and v1-5

Figure 21: *The variation of the TE squared optical matrix elements for Structure 2 calculated using the one-dimensional effective mass envelope functions at $k_{||}=0$.*

well with the optical matrix elements calculated using the ***k.p*** envelope functions at $k_{||}=0$.

3.6 Joint densities of states for Structures 1 and 2

The joint density of states was calculated, using the ***k.p*** model, for the Structure 1 band pairing c1-v2 at three values of applied bias and is shown in Figure 22 (see Section (2.9), Chapter 2). The values plotted are the average of the four possible singly degenerate pairings of the two subband pairs. The joint density of states close to the band edge increases with increasing bias. This increase is due to the change in effective mass of both the conduction and valence subbands with increasing bias. The conduction subbands become heavier with increasing bias, whilst the behaviour of the valence subbands is complicated by strong band mixing and changes in their relative position to the other subbands. At 5 V there is a singularity in the joint density of states at approximately $k_{||}=0.005\,\mathring{A}^{-1}$, which is a result of a turning point of the subband v2a (the upper of the spin split pair) which is 'electron-like' close to $k_{||}=0$ [27] (see Figure 12). At large in-plane wavevectors, the joint density of states tends to a constant value at zero bias with only a small shift to higher values with increasing bias.

The joint density of states was calculated, using the ***k.p*** model, for the Structure 2 band pairing c1-v1 at three values of applied bias and are also shown in Figure 22. The joint density of states close to the bandedge increases with increasing bias. At

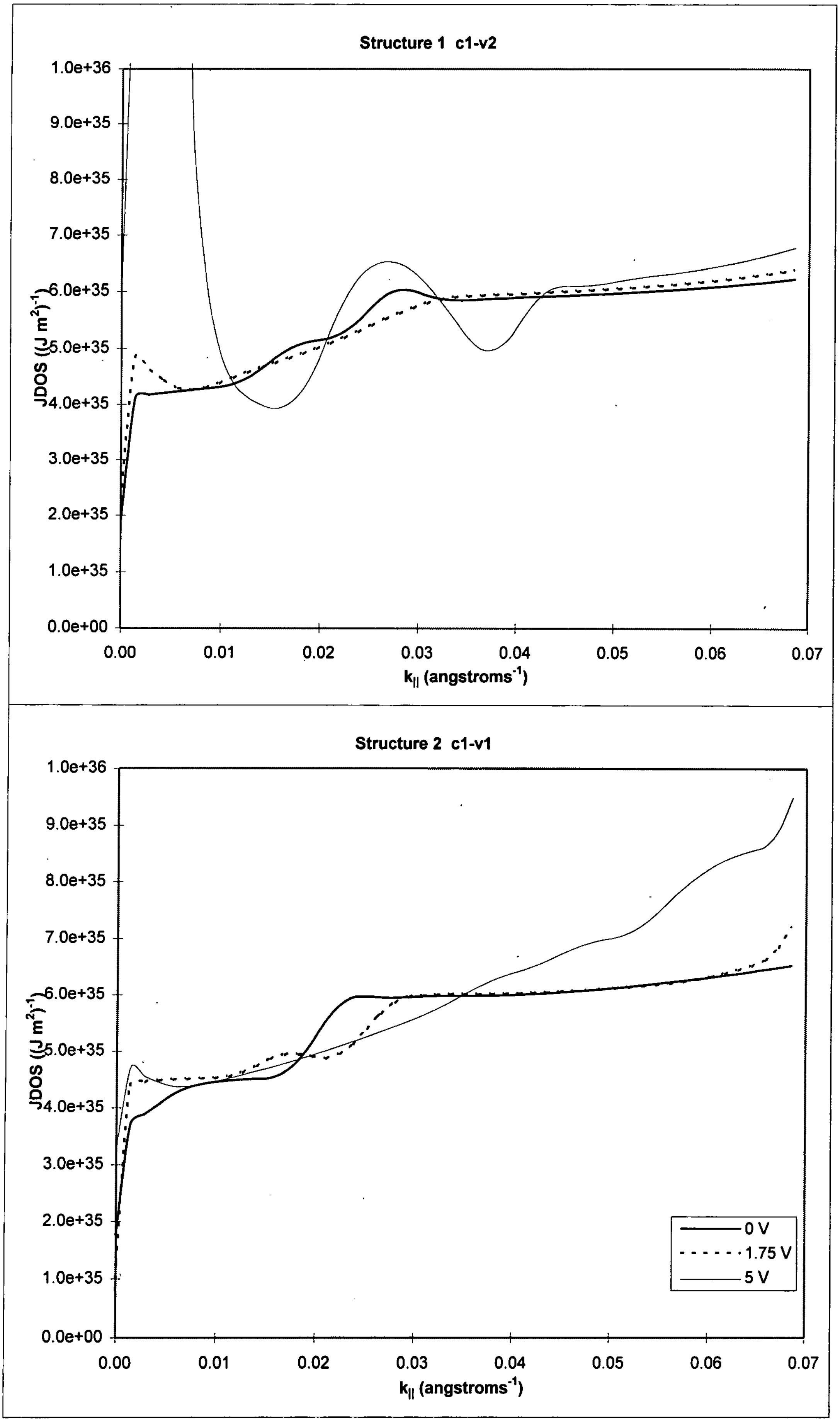

Figure 22: *The average joint density of states for the transitions c1-v2 (Structure 1) and c1-v1 (Structure 2) for three values of applied bias.*

large in-plane wavevectors, the joint density of states tends to a constant value at zero bias. The joint density of states increases significantly with increasing bias for in-plane wavevectors greater than $k_{\|}$=0.035 $\mathring{A}^{-1}$.

3.7 Discussion of the calculated absorption spectra for Structures 1 and 2

The calculated absorption spectra for Structures 1 and 2 for three values of applied bias are shown in Figure 6. At zero bias both structures at zero bias are predicted to have little or no absorption at a wavelength of 1.55 μm (see Figure 7). However for both structures with a bias close to 3.7 V the long wavelength absorption shoulder has shifted to 1.55 μm, resulting in a significant increase in absorption at this wavelength. The transition responsible for this absorption shoulder is c1-v2 for Structure 1 and c1-v1 for Structure 2. For both structures the states associated with the conduction and valence subbands in question are localised in the wide well (see Figures 10 and 14). Figure 23 shows the shift in wavelength for these two transitions with increasing bias calculated using the ***k.p*** and the one-dimensional effective mass models. The behaviour of the two transitions with applied bias shown in Figure 23 is very similar to that of the long wavelength absorption shoulder in Figure 5. The c1-v2 transition for Structure 1 shows a linear shift to longer wavelengths with increasing bias, whilst the c1-v1 transition for Structure 2 shows a reduction at low bias before a near-linear shift to longer wavelengths. The latter behaviour is a result of the c1 subband, which is in near-resonance with the c2 at zero bias, and is pushed above the c2 subband at approximately 0.75 V. The resonance is lost for larger applied bias resulting in the linear shift in the transition wavelength.

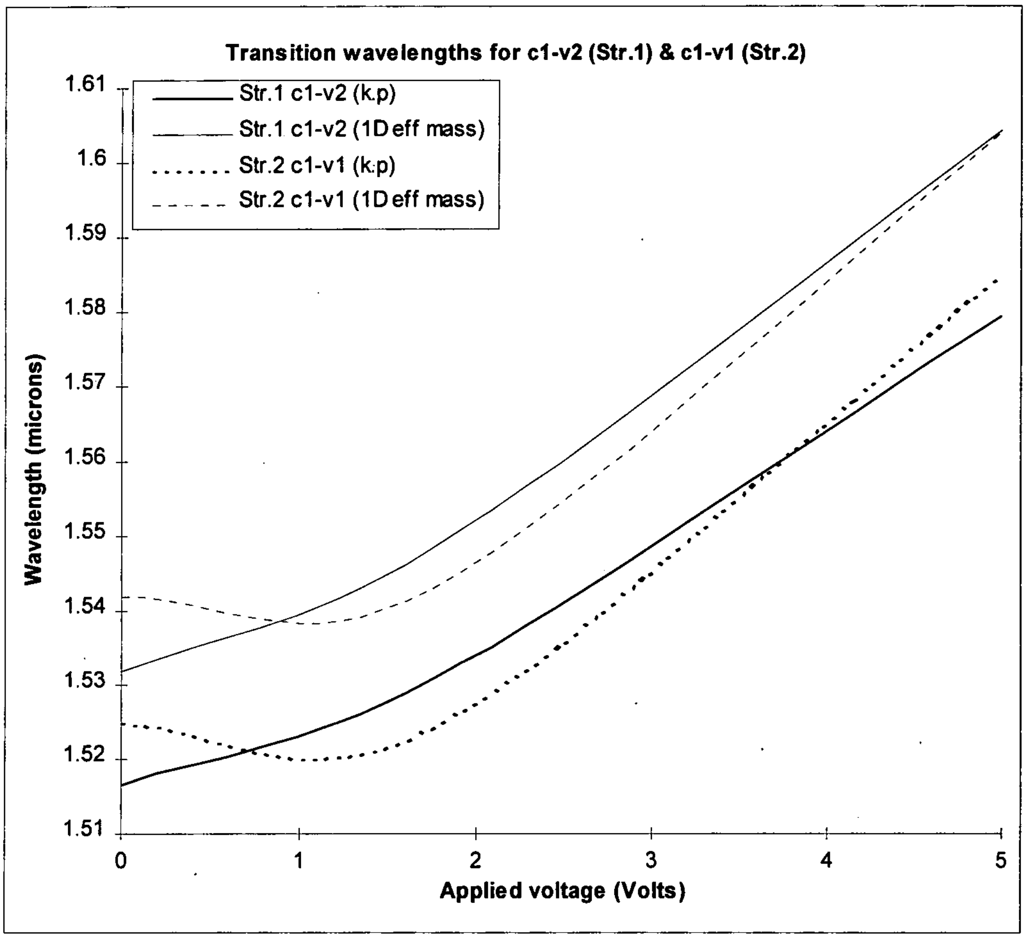

Figure 23: *The shift in transition wavelength for c1-v2 (Str.1) and c1-v1 (Str.2) with increasing bias calculated using the* ***k.p*** *and the one-dimensional effective mass models.*

The magnitude of the absorption shoulder in Figure 6 for Structure 1 at zero bias is larger than the corresponding feature for Structure 2. This is a direct result of the larger optical matrix element for the c1-v2 transition of Structure 1 compared to the c1-v1 transition of Structure 2 (as apparent in Figures 18 and 20). Note, figure 22 shows that the joint densities of states for these two transitions are similar.

At 1.75 V, the absorption shoulder for Structure 1 has shifted to longer wavelengths and the magnitude of the absorption has decreased. The optical matrix element for the c1-v2 transition suggests that the absorption shoulder should be smaller but is mitigated to some extent by the general increase in the joint density of states at 1.75 V for the transition. The absorption shoulder for Structure 2 at 1.75 V does not shift to longer wavelength compared to its zero bias value due to the field behaviour of the c1-v1 transition shown in Figure 23. Whilst the absence of a significant wavelength shift is expected from the calculations, the optical matrix elements for the transition suggest that the absorption should have declined significantly. The increase in the joint density of states at 1.75 V does not by itself account for the overall increase in absorption. However, analysis of Figures 9 and 17, which describe the shift in conduction and valence subband energies with increasing bias, show that the two transitions c2-v2 and c2-v3 at 1.75 V occur at the same wavelength as the transition c1-v1. Whilst the optical matrix elements for these two transitions are only about one tenth of the matrix element for the c1-v1 transition, the combined effect is to increase the absorption by approximately 13% at this wavelength.

At 5 V, the absorption shoulder for Structures 1 and 2 has shifted beyond 1.55 μm. The absorption magnitude of this feature is larger for Structure 1. This is principally due to the large joint density of states close to the bandedge seen in Figure 22 for c1-v2. The transitions c2-v2 and c2-v3 no longer contribute strongly to the absorption shoulder of Structure 2 since they have been swept to much longer wavelengths at 5 V, and indeed their respective optical matrix elements are essentially zero.

3.8 Comparison between theory and experiment

In the previous sections, the calculated absorption spectra for Structures 1 and 2 at three values of applied bias have been discussed. The structures were originally proposed by GEC-Marconi as possible candidates for the particle sensor optical links for the European Large Hadron Collider Experiment at CERN. An attempt was made to grow the two structures by metal organic vapour phase epitaxy (MOVPE), and room temperature photocurrent spectra under applied bias were measured [6,47].

It was found using transmission electron microscopy that the grown structures had deviated from the target design. Measurements showed that the active region of Structure 1 was

> *n* doped region / 110 Å *InGaAs* / 25 Å *InP* / 50-65 Å *InGaAs* / *p* doped region

compared to the target

> *n* doped region / 100 Å *InGaAs* / 20 Å *InP* / 60 Å *InGaAs* / *p* doped region.

The measurements of the active region for Structure 2 gave

> *n* doped region / 65 Å *InGaAs* / 25 Å *InP* / 110 Å *InGaAs* / *p* doped region

compared to the target

> *n* doped region / 60 Å *InGaAs* / 20 Å *InP* / 100 Å *InGaAs* / *p* doped region.

In addition, the ternary well material was found to be $In_{0.55}Ga_{0.45}As$ which results in a small compressive strain of 0.12%.

Despite the differences in well widths and well material it is instructive to compare the calculated spectra for the target structures with the measured spectra for the grown structures. Figure 24 shows the comparison for Structure 1 for three values of applied bias. Whilst the experimental spectra are shifted to longer wavelengths compared to the calculated ones, there is a general similarity between them. Each spectrum shows an absorption shoulder at long wavelengths (1.51 and 1.61 μm for the calculated and measured spectra respectively at zero bias). This feature shifts to longer wavelengths and the absorption magnitude decreases with increasing bias for both spectra. The calculated absorption shoulder shifts to 1.58 μm at 5 V (a shift of 0.07 μm), and to 1.69 μm in the measurements (a shift of 0.08 μm). The difference in wavelength shift with increasing bias is a direct result of the difference in the wide well widths between the target and grown structures (100 and 110 angstroms respectively). As shown earlier in Figures 9 and 13, the shift in the subband energies with increasing bias is dependent on which well the associated states are localised in. The wider the well the larger is the wavelength shift with bias. Therefore, it is expected that the calculated absorption shoulder for a 110 angstrom wide well would shift to longer wavelengths by a further 10% or approximately 0.08 μm at 5 V, in good agreement with measured value for the grown Structure 1.

A one-dimensional effective mass calculation was carried out for the the grown Structure 1 for the three applied bias values. These results show that the energy separation of the c1-v2 transition at zero bias decreases by 22 meV, which pushes the calculated absorption shoulder out to 1.55 μm. It has already been demonstrated in

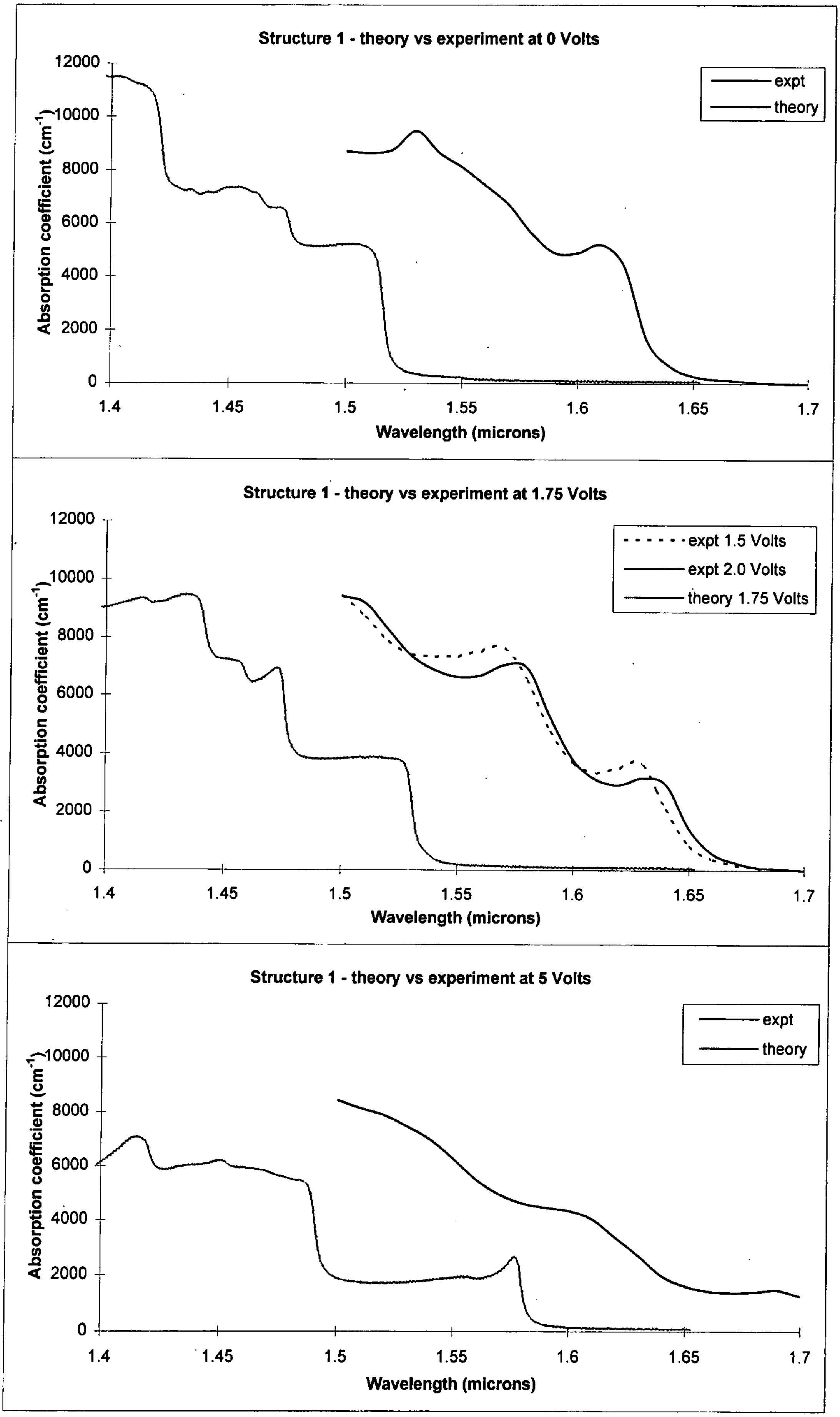

Figure 24: *Comparison between calculated and measured absorption spectra (at room temperature) for Structure 1 for three values of applied bias.*

this Chapter that the one-dimensional effective mass model shows excellent agreement with the ***k.p*** model in predictions of the field dependent behaviour of the conduction and valence subband energies and the optical matrix elements. Hence the energy shift of the c1-v2 transition resulting from the wider structure can be used with reasonable confidence to predict the additional wavelength shift of the absorption shoulder in question. At 1.75 and 5 V, the calculated absorption shoulder shifts to 1.58 and 1.63 μm respectively.

In addition, the bulk bandgap for unstrained *InGaAs* was calculated to be 0.764 using the method proposed by Krijn [35] (see Appendix 2) which is 14 meV larger than the generally accepted value of 0.75 eV (at room temperature). Without attempting to determine the exact effect this reduced energy bandgap has on the bandstructure, the general effect will be to reduce the c1-v2 energy separation by 14 meV. Combining this energy shift with those calculated for the wider grown structure for the c1-v2 transition, suggests that the absorption shoulder of interest appears at 1.58 μm at 0 V, 1.60 μm at 1.75 V and at 1.66 μm at 5 V. Whilst the agreement between the calculated and measured spectra is still not perfect, the majority of the wavelength shift for the grown structure has been accounted for.

The remaining energy difference between the calculated and the measured spectra is approximately 13 meV for the three bias values considered. Gershoni *et al* [1] showed that their computed spectra for an *InGaAs*/*InP* superlattice in an externally applied electric field were shifted to lower energies by 10 meV compared to the experimentally measured spectra for a range of electric fields similar to ours. The authors believed that this energy difference might be attributable to excitonic effects. The other possibility is the fact that the experimentally determined spectra [61] are based on photocurrent measurements (as for the GEC-Marconi results), whilst the spectra predicted by Gershoni *et al* were for absorption. Photocurrent excitation spectra also include contributions from transport as well as carrier collection efficiency, which may depend on the carrier energy and field strength. The formation of different electric field domains, due to screening by residual carriers [48], may also contribute to the complexity of the experimental data, and some uncertainty in determining the electric field strength/voltage relationship for the device.

The optical matrix element for c1-v2 at 5 V, for the grown Structure 1, calculated using the one-dimensional effective mass envelope functions is smaller than the corresponding matrix element for the target structure by 11%. This accounts, in part, for the smaller absorption magnitude of the corresponding feature in the measured spectrum, compared to the calculated.

Figure 25 shows the comparison between the calculated and measured spectra for Structure 2 at three values of applied bias. As for Structure 1, the two spectra generally show the same features, but the measured spectrum is shifted to longer wavelengths. A one-dimensional effective mass calculation for the transition of interest was carried out for the grown structure which showed that the calculated absorption shoulder shifts to 1.56 μm at 0 V, 1.57 μm at 1.75 V and 1.63 μm at 5 V.

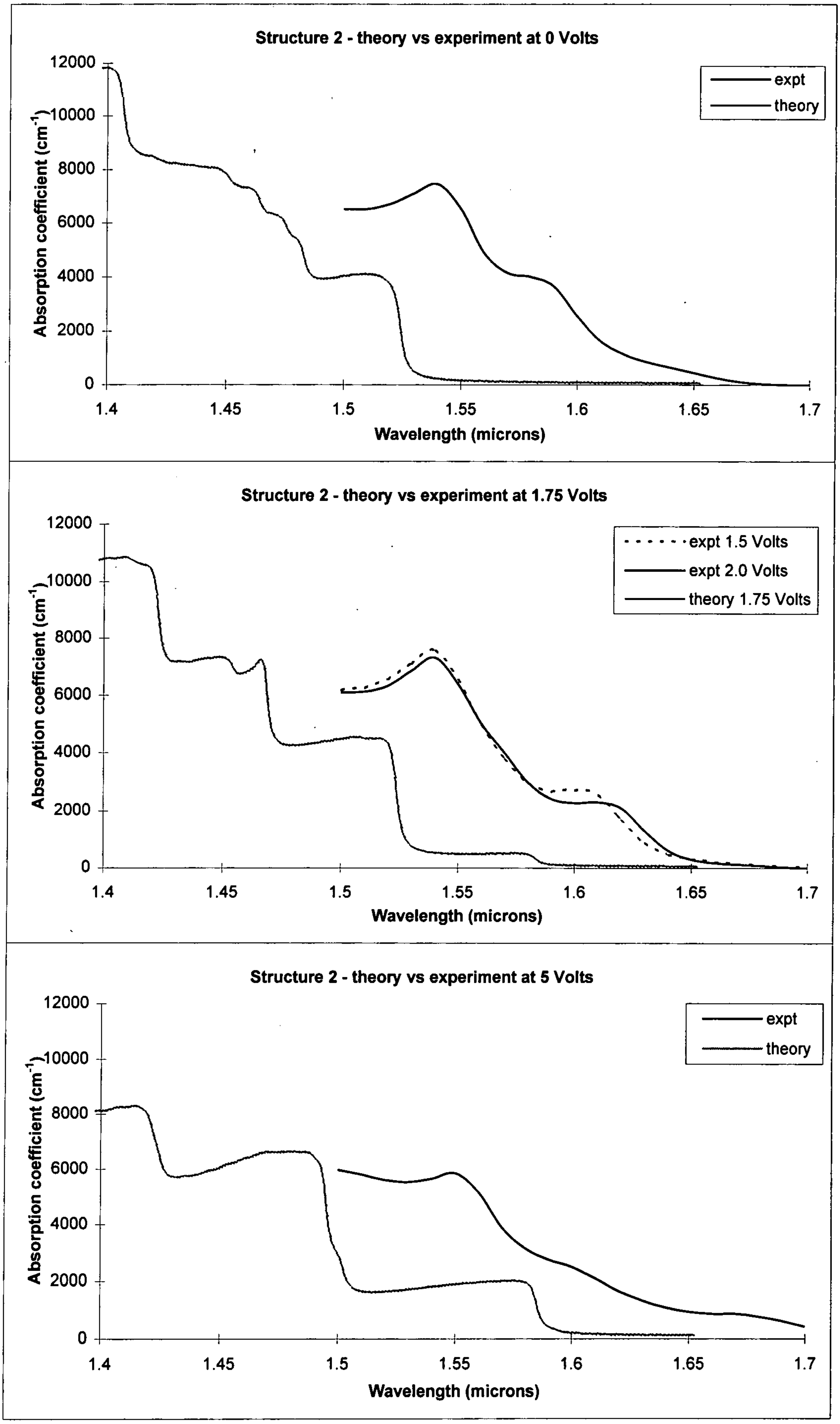
Structure 2 - theory vs experiment at 0 Volts

Structure 2 - theory vs experiment at 1.75 Volts

Structure 2 - theory vs experiment at 5 Volts

Figure 25: *Comparison between calculated and measured absorption spectra (at room temperature) for Structure 2 for three values of applied bias.*

When the energy shift due to the bulk bandgap estimation is included, the absorption shoulder moves to 1.59 μm at 0 V, 1.6 μm at 1.75 V and 1.66 μm at 5 V. The calculated spectra for Structure 2 are shifted to lower energy by approximately 9 meV (at 5 V) compared to the measured spectra.

The optical matrix element for c1-v1 at 5 V, for the grown Structure 2, calculated using the one-dimensional effective mass envelope functions is smaller than the corresponding matrix element for the target structure by 18%. This accounts, in part, for the smaller absorption magnitude of the corresponding feature in the measured spectrum, compared to the calculated.

To conclude, the poor intensity modulation performance of the grown structures for light at a wavelength of 1.55 μm is a result of the increased width of the active region, coupled with a slightly strained well material compared with the target structures. The confidence gained from the comparison between the calculated and measured spectra suggest that the proposed structures may perform significantly better as 1.55 μm light modulators. However, when the 14 meV shift due to the bulk bandgap overestimate is applied to the calculated spectra, the base of the absorption shoulder for Structure 1 at zero bias appears at 1.55 μm. Application of a small bias should result in a large increase in absorption at 1.55 μm. On the other hand for Structure 2, the absorption shoulder appears at 1.55 μm. Application of bias will result only in a small change in absorption at 1.55 μm, although it is worth pointing out that application of a small forward bias may result in a large decrease in absorption at this wavelength. Measured spectra suggest that the calculated results should be shifted to lower energy by approximately 10 meV to be realistic, however the authors [1] suggest that this shift is possibly an artefact of photocurrent measurements and may not exist (or at least be smaller) for direct light absorption measurements.

Summary

A multilayered ***k.p*** model was presented which allows the calculation of the electronic states and bandstructure for coupled quantum wells in an externally applied electric field.

This model was used to calculate the bandstructure and the optical matrix elements for two asymmetric coupled quantum well structures which were proposed by GEC-Marconi as possible candidates for intensity modulators for light at a wavelength of 1.55 μm.

The conduction and valence energy eigenvalues, envelope functions and optical matrix elements for the same two structures were also calculated, at $k_{\|}=0$, using a simpler one-dimensional effective mass model. The results from the two models compared favourably for both structures for applied voltages ranging from 0 to 5 V.

The ***k.p*** bandstructure and optical matrix elements were used to calculate the electric field dependent absorption spectra for the two structures. The results were discussed in terms of bandstructure, localisation of the conduction and valence states, optical matrix elements and joint densities of states. The calculated results showed that for both structures the absorption of light at a wavelength of 1.55 μm was small at zero bias. At 3.7 V, the absorption at 1.55 μm increases by a factor of 6 for Structure 1 and 9 for Structure 2. These results suggest that the two proposed structures show promise for light intensity modulators operating at 1.55 μm.

Two similar structures were grown by GEC-Marconi and photocurrent spectra (at room temperature) were measured for bias values ranging from 0 to 5 V. The grown structures deviated from the target dimensions and the well material was also found to be nominally strained. Nevertheless, a comparison between the calculated spectra and the measured spectra shows good agreement as regards spectral features and behaviour with increasing bias. The appearance of the absorption edge at longer wavelengths for both grown structures was reconciled with recourse to a one-dimensional effective mass calculation. These results showed that the absorption edge for both structures shifted to longer wavelengths. For the three applied voltages considered the calculated spectra for Structures 1 and 2 appear at a higher photon energy compared to the measured spectra. This shift has been observed by Gershoni *et al* [1]. The results suggest that Structure 1 shows the better potential as an intensity modulator for light at a wavelength of 1.55 μm.

References for Chapter Three

[1] M. Pistol and D. Gershoni, Phys. Rev. B, **50**, 11738 (1994)

[2] G. Sanders and K. Bajaj, Phys. Rev. B, **35**, 2308 (1987)

[3] R. Beresford, Semicond. Sci. Technol., **8**, 1957 (1993)

[4] J. Zang and M. Rustgi, Infrared Phys., **33**, 175 (1992)

[5] G. Sanders and K. Bajaj, J. Appl. Phys., **68**, 5348 (1990)

[6] J. Thompson, A. J. Moseley, D. J. Robbins, N. Carr and M. Q. Kearley, MOVPE workshop (extended abstracts), Gent (1995)

[7] M. N. Islam, R. L. Hillman, D. A. B. Miller, D. S. Chemla, A. C. Gossard and J. H. English, Appl. Phys. Lett., **50**, 1098 (1987)

[8] A. Dimoulas, K. P. Giapis, J. Leng, G. Halkias, K. Zekentes & A. Christou, J. Appl. Phys., **72**, 1912 (1992)

[9] A. Dimoulas, J. Leng, K. P. Giapis, A. Georgakilas, G. Halkias & A. Christou, Applied Surface Science, **63**, 191 (1993)

[10] T. Aizawa, K. G. Ravikumar, S. Suzaki, T. Watanabe and R. Yamauchi, J. Quant. Elect., **30**, 585 (1994)

[11] B. N. Gomatam, N. G. Anderson, F. Agahi, C. F. Musante and K. M. Lau, Appl. Phys. Lett., **62**, 3473 (1993)

[12] S. Chelles, R. Ferreira, P. Voisin, A. Ougazzaden, M. Allovon and A. Carenco, Appl. Phys. Lett., **64**, 3530 (1994)

[13] T. Tutken, B. J. Hawdon, M. Zimmerman, I. Queisser, A. Hangleiter, V. Harle and F. Scholz, Appl. Phys. Lett., **64**, 403 (1994)

[14] R. W. Martin, J. Thompson, A. J. Moseley, D. J. Robbins, N. Carr, M. Q. Kearley & J. E. Metcalf, Instit. Phys. Conf. Ser., **155**, 775 (1996)

[15] D. Miller, Opt. Eng., **26**, 368 (1987)

[16] Y. M. Huang, C. F. Wang and C. F. Lien, J. Quant. Elect., **31**, 1717 (1995)

[17] D. Atkinson, G. Parry & E. J. Austin, Semicond. Sci. Technol., **5**, 516 (1990)

[18] G. Bastard & J. Brum, J. Quant. Elect., **QE 22**, 1625 (1986)

[19] R. Ferreira and G. Bastard, Solid-State Electronics, **37**, 851 (1994)

[20] K. Yamanaka, T. Fukunaga, N. Tsukada, K. L. I. Kobayashi and M. Ishii, Appl. Phys. Letts., **48**, 840 (1986)

[21] P. W. Yu, G. D. Sanders, K. R. Evans, D. C. Reynolds, K. K. Bajaj, C. E. Stutz and R. L. Jones, Appl. Phys. Letts., **54**, 2230 (1989)

[22] I. J. Fritz, T. M. Brennan, J. R. Wendt and D. S. Ginley, Appl. Phys. Letts., **57**, 1245 (1990)

[23] S. Nojima, Y. Kawamura, K. Wakita and O. Mikami, J. Appl. Phys., **64**, 2795 (1988)

[24] K. Satzke, G. Weiser, W. Stolz and K. Ploog, Phys. Rev. B, **43**, 2263 (1991)

[25] D. A. B. Miller, D. S. Chemla, T. C. Damen, A. C. Gossard, W. Wiegmann, T. H. Wood and C. A. Burrus, Phys. Rev. Letts., **53**, 2173 (1984)

[26] D. A. B. Miller, D. S. Chemla, T. C. Damen, A. C. Gossard, W. Wiegmann, T. H. Wood and C. A. Burrus, Phys. Rev. B, **32**, 1043 (1985)

[27] M. Ogawa & T. Miyoshi, Jpn. J. Appl. Phys., **34**, 4535 (1995)

[28] B. Zhu & Y. Chang, Phys. Rev. B, **50**, 11932 (1994)

[29] R. Winkler & U. Rossler, Phys. Rev. B, **48**, 8918 (1993)

[30] E. O. Kane, J. Phys. Chem. Solids, **1**, 82 (1956)

[31] A. Tackeuchi, A. P. Heberle, W. W. Ruhle, K. Kohler and S. Muto, Jpn. J. Appl. Phys., **34**, L543 (1995)

[32] R. Eppenga, M. Schuurmans & S. Colak, Phys. Rev. B, **36**, 1554 (1987)

[33] A. Kucharska & D. J. Robbins, IEEE J. Quant. Elect., **QE26**, 443 (1990)

[34] M. Asada, IEEE J. Quant. Elect., **QE25**, 2019 (1989)

[35] M. Krijn, Semicond. Sci. Technol., **6**, 27 (1991)

[36] Numerical Data and Functional Relationships in Science and Technology, edited by O. Madelung, New Series, Group III, Vols. 17a & 22a (Springer, Berlin, 1982,1987)

[37] G. Bastard, E. E. Mendez, L. L. Chang and L. Esaki, Phys. Rev. B, **28**, 3241 (1983)

[38] R. W. Martin, S. L. Wong, R. J. Nicholas, K. Satzke, M. Gibbon & E. J. Thrush, Semicond. Sci. Technol., **8**, 1173 (1993)

[39] G. D. Sanders and K. K. Bajaj, Appl. Phys. Lett., **68**, 930 (1989)

[40] T. Tutken, B. J. Hawdon, M. Zimmermann, A. Hangleiter, V. Harle & F. Sholz , Appl. Phys. Lett., **63**, 1086 (1993)

[41] N. Susa & T. Nakahara, Appl. Phys. Lett., **60**, 2324 (1992)

[42] W. Chen and T. G. Andersson, Semicond. Sci. Technol., **7**, 828 (1992)

[43] T. H. Wood, C. A. Burrus, D. A. B. Miller, D. S. Chemla, T. C. Damen, A. C. Gossard and W. Weigman, IEEE J. Quant. Electron., **QE21**, 117 (1985)

[44] D. A. B. Miller, D. S. Chemla, T. C. Damen, T. H. Wood, C. A. Burrus, A. C. Gossard and W. Wiegmann, and Opt. Lett., **9**, 567 (1984)

[45] T. H. Wood, C. A. Burrus, A. H. Gnauck, J. M. Wiesenfeld, D. A. B. Miller, D. S. Chemla and T. C. Damen, Appl. Phys. Lett., **47**, 190 (1985)

[46] D. A. B. Miller, D. S. Chemla, T. C. Damen, A. C. Gossard, W. Wiegmann, T. H. Wood and C. A. Burrus, Appl. Phys. Lett., **45**, 13 (1984)

[47] A. J. Moseley, J. Thompson, M. Q. Kearley, D. J. Robbins & M. J. Goodwin, Electron. Lett., **26**, 914 (1990)

[48] R. E. Cavvichi, D. V. Lang, D. Gershoni, A. M. Sergent, H. Temkin & M. B. Panish, Phys. Rev. B, 38, 13474 (1988)

[49] T. W. Kim and C. O. Kim, J. Mat. Sci. Letts, **15**, 450 (1996)

[50] T. W. Kim, Solid State Comm., **94**, 939 (1995)

[51] S. J. Kim, Y. T. Oh, S. K. Kim, T. W. Kang and T. W. Kim, J. Appl. Phys., **77**, 2486 (1995)

[52] S. J. Rhee, J. C. Oh, Y. M. Kim, H. S. Ko, W. S. Kim, D. H. Lee, J. C. Woo and K. H. Yoo, Institute of Physics Conf. Series, **136**, 415 (1994)

[53] Y. M. Huang and C. H. Lien, J. Appl. Phys., **76**, 3181 (1994)

[54] M. K. Chin, J. Appl. Phys., **76**, 518 (1994)

[55] Y. M. Huang, C. H. Lien and T. F. Lei, J. Appl. Phys., **74**, 2598 (1993)

[56] J. A. Trezza, M. C. Larson, S. M. Lord and J. S. Harris, J. Appl. Phys., **74**, 1972 (1993)

[57] B. Olejnikova, Semicond. Sci. Tech., **8**, 525 (1993)

[58] N. Susa, J. Appl. Phys., **73**, 932 (1993)

[59] Y. Arakawa and A. Yariv, J. Quant. Elect., **QE-21**, 1666 (1985)

[60] M. P. Houng, Y. H. Wang and C. H. Chu, J. Appl. Phys., **77**, 6338 (1995)

[61] I. Bar-Joseph, C. Klingshirn, D. A. B. Miller, D. S. Chemla, U. Koren and B. I. Miller, Appl. Phys. Lett., **50**, 1010 (1987)

[62] P. A. Chen, L. Y. Chang and C. Juany, J. Appl. Phys., **74**, 7294 (1993)

CHAPTER FOUR

POLARIZATION INSENSITIVE AMPLIFIERS

4.1 Introduction

Optical amplifiers are key devices in the operation of optical transmission systems, with applications in wavelength conversion, switching, signal processing as well as simple amplification. Multi-quantum well based devices satisfy most of the required attributes of a suitable amplifier such as high gain, optical output power and wide bandwidth, low noise, and energy consumption/drive current, and also offer the possibility to be integrated into photonic integrated circuits. However, in most multi-quantum well structures the gain is highly polarization sensitive due to a) different cross-sectional lengths of the optically active region along the plane of the well and along the growth direction, and b) the nature of the highest valence subband.

The first characteristic a) leads to a difference in optical confinement factors, Γ_{TE} and Γ_{TM} , for TE and TM modes respectively. These factors can be equalised by using a thick active layer [35-37], a large optical cavity [38-39] or by returning to a bulk structure [40-42, 44-45]. The second characteristic b) dictates the polarization of the generated photons. In thin unstrained or compressively strained wells the highest valence subband is heavy hole in character but in a well with sufficient tensile strain the highest valence subband is light hole in character. This is important because of the effect on the bandedge density of states but also because the different optical matrix elements squared for the possible modes as shown in Table 1 [6,13].

Mode	Matrix element squared	
	c - hh	c - lh
TE	$\frac{1}{2}$	$\frac{1}{6}$
TM	0	$\frac{2}{3}$

Table 1: *The relative values of the optical matrix elements squared for the different modes and transitions.*

In principle, polarization insensitivity can be realised by balancing the respective gain characteristics and optical confinement factors for TE and TM modes in an appropriate structure. A number of approaches have been used to try to achieve this, notably 1) a single tensile well [1-6], 2) a combination of compressive and tensile wells [19-27, 31-32], 3) tensile barriers and unstrained wells [14-17], and 4) tensile barriers and compressive wells [28-30, 33].

In this work the possibility of a polarization insensitive gain is investigated for two types of structure, namely a single tensilely strained well and a structure with a stepped well active region which comprises two layers, one with tensile and one with compressive strain. Room temperature gain calculations for both TE and TM modes have been carried out, the polarization dependence in the 1.55 μm wavelength region of the spectrum is discussed, and design criteria are considered.

4.2 The origin of polarization sensitivity in a quantum well structure

In thin unstrained and compressively strained quantum wells the highest valence subband is heavy hole in character. In the ***k.p*** model discussed in Chapter 2 this subband is decoupled from all other subbands at $k_{\parallel} = 0$ and is made up of the bulk zone centre states u_2 and u_6 (of Table 1, Chapter 2). It follows that electron transitions from a conduction subband state to a heavy hole state only produce photons with electric field vector polarized in the plane of the well (TE polarized). To a first approximation the coupling of the conduction band states to the light hole and spin split-off bands can be neglected and then the conduction subband states are made up of u_1 and u_5 zone centre states. In this approximation a calculation of the squared optical matrix element near $k_{\parallel}=0$ yields [6,13]

$$|\mathrm{M_{TE}}|^2 = \frac{1}{2}\left|\langle s|p_x|x\rangle\right|^2 \tag{1}$$

In tensilely strained wells the highest valence subband can be light hole in character and the dominant components near $k_{\parallel} = 0$ derive from the u_3 and u_7 zone centre states. If the smaller contributions from the conduction and spin split-off states are neglected, electron transitions from a conduction subband state to a light hole state produce photons with electric field vectors polarized in the well plane (TE) and the growth (TM) directions. The squared optical matrix element for the TE and TM transitions close to $k_{\parallel} = 0$ are [6,13]

$$|M_{TE}|^2 = \frac{1}{6}\left|\langle s|p_x|x\rangle\right|^2 \qquad (2)$$

$$|M_{TM}|^2 = \frac{2}{3}\left|\langle s|p_x|x\rangle\right|^2 \qquad (3)$$

Away from $k_{\|}=0$ substantial band mixing occurs in all subbands and the approximations made in the previous discussion are no longer valid. However it is generally the case that TE gain is dominant in unstrained and compressively strained quantum wells, whilst TM gain is dominant for tensilely strained quantum wells.

The above arguments suggest that a structure which is sufficiently strained (for example ~ 0.2% tensile for *InGaAs*) such that the lowest heavy hole and light hole bands occur at the same energy would produce similar numbers of TE and TM polarized photons. However, the gain is also dependent on the joint densities of states and whilst it is possible to determine a structure with both the lowest heavy hole and light hole subbands occurring at the same energy, the effective masses (and hence the joint densities of states) are very different. The light hole subband mass is normally much larger than that for the heavy hole resulting in a larger density of states and hence larger TM gain [47-49]. A further complication is caused by the different power confinement factors for the two modes, with Γ_{TE} being larger than Γ_{TM} (by a factor of ~1.2). Therefore, the design of a structure that will yield equal net TE and TM gain requires a balancing of all these factors.

One approach to the problem is to choose a structure where the lowest light hole and heavy hole subbands are close in energy, and the energy separation between these and the first conduction subband is less than 0.8 eV (≡ 1.55 μm). The TE and TM gains decrease in different ways above the bandedge and with suitable choice of materials , strain and well width the gain curves can be arranged to cross at or close to 0.8 eV. Whilst this can be achieved there are problems. First, the crossover point (photon energy of polarization insensitivity) moves with increasing device drive current due to the shift in the quasi-Fermi levels with increasing carrier density and bandgap narrowing. Second, there will always be a difference between the TE and TM gain on either side of the crossover point. Whilst the former can be overcome by designing the structure such that the crossover point occurs at 0.8 eV at a drive current that produces the required optical gain, the latter determines the wavelength stability of the amplifier. If the difference between the TE and TM gain changes rapidly around the crossover point, light with a slightly different wavelength will experience a significantly different gain for each polarization state. Therefore, a further requirement is for the gain slopes for both modes to be similar.

4.3 Gain calculation

The broadened spectral gain for the structure in question is calculated using the expression

$$g^{broad}(\hbar\omega) = \sum_{ij} \int_{-\infty}^{+\infty} \frac{\pi e^2 \hbar}{m^2 \varepsilon_0 \mu \hbar \omega c L_z} \left| M_{ij} \right|^2 \left(f_c - f_v \right) \rho_{ij} \; \frac{L\left(E_{ij} - \hbar\omega \right)}{\pi} \, dE_{ij} \tag{4}$$

where all the symbols have been defined in association with eqs. (124) - (129) of Chapter 2. Note that the gain coefficient is the negative of the absorption coefficient (defined in eq.(129) of Chapter 2). The full width half maximum of the Lorentzian broadening function, L, is taken as 6 meV as used by Yariv *et al* [50-53]. The Fermi occupation factors, f_c and f_v, for the conduction and valence bands states at energies E_c and E_v are defined by

$$f_c(E_c) = \frac{1}{\exp[(E_c - F_c)/k_B T] + 1} \tag{5}$$

$$f_v(E_v) = \frac{1}{\exp[(E_v - F_v)/k_B T] + 1} \tag{6}$$

where, F_c and F_v are the relevant quasi-Fermi levels.

The conduction quasi-Fermi level is calculated from the total density of injected electrons (n) using the relation

$$n = \frac{1}{L_z}\sum_i \int_{\Delta E_i}^{+\infty} f_c(E)\rho_i(E)dE = \frac{1}{\pi L_z}\sum_i \int_0^{k_0} \frac{kdk}{1+\exp[(E_i(k) - F_c)/k_B T]} \tag{7}$$

whilst the valence quasi-Fermi level is calculated from the total density of injected holes (p) by

$$p = \frac{1}{L_z}\sum_j \int_{-\infty}^{\Delta E_j} (1 - f_v(E))\rho_j(E)dE = \frac{1}{\pi L_z}\sum_i \int_0^{k_0} \frac{kdk}{1+\exp[(F_v - E_j(k))/k_B T]} \tag{8}$$

where i and j are the subband labels, ρ_i the subband densities of states and ΔE_i the subband edge energies. The integrations over the magnitude of the two dimensional wavevector, k, are evaluated numerically with the upper limit of the range restricted to a cut off value, k_0, above which the probability of a conduction/valence subband being occupied by an electron/hole is negligible. The condition of charge neutrality ($n = p$) is used in all the calculations.

4.4 A single tensilely strained quantum well

The first structure examined, which we will refer to as Structure 1, was a 200 angstrom 0.44% tensilely strained single quantum well in which the well material $In_{0.47}Ga_{0.53}As$ is sandwiched between two layers of $In_{0.74}Ga_{0.26}As_{0.57}P_{0.43}$ (lattice matched to InP). The material parameters used to calculate the bandstructure are shown in Appendix 1. The calculated conduction and valence bandstructures, together with the band character, are given in Figure 1.

Figure 2 (top) shows the calculated TE and TM gain spectra at room temperature for a range of carrier densities (optical confinement effects and bandgap narrowing not included). For all carrier densities and wavelengths considered, the TM gain is considerably larger than TE gain, due to the large optical matrix elements between c1 to v1 (lh), and c2 to v4 (lh) and the large joint densities of states [47-49]. Here the subbands are labelled according to the definition proposed in Section (3.4) of Chapter 3. The TM peaks occur at approximately 1.55 & 1.43 μm respectively. The two features occurring at 1.51 & 1.43 μm in the TE spectra are primarily a result of the transitions c1 to v2 (hh) and c2 to v3 (hh).

The calculated net gain including optical confinement and bandgap narrowing is also shown in Figure 2 (bottom). The mode optical confinement factors were estimated from the refractive indices calculated using the formulae of sec.(14.6.2) of reference [8] and the method from reference [9-10]. This calculation was based on the structure

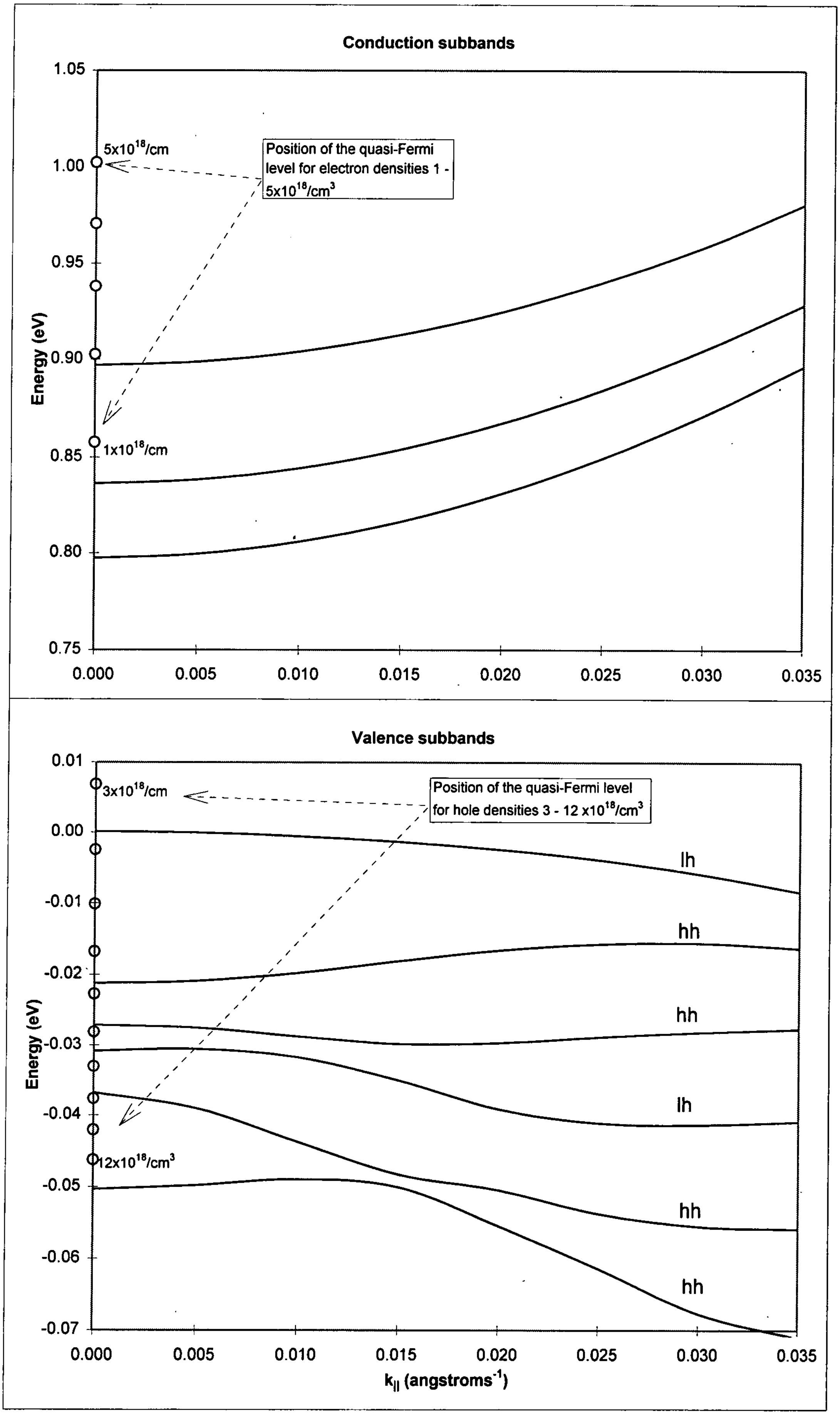

Figure 1: *Bandstructure for Structure 1, calculated using the* ***k.p*** *model. The structure is symmetric which results in the conduction and valence subbands being doubly degenerate.*

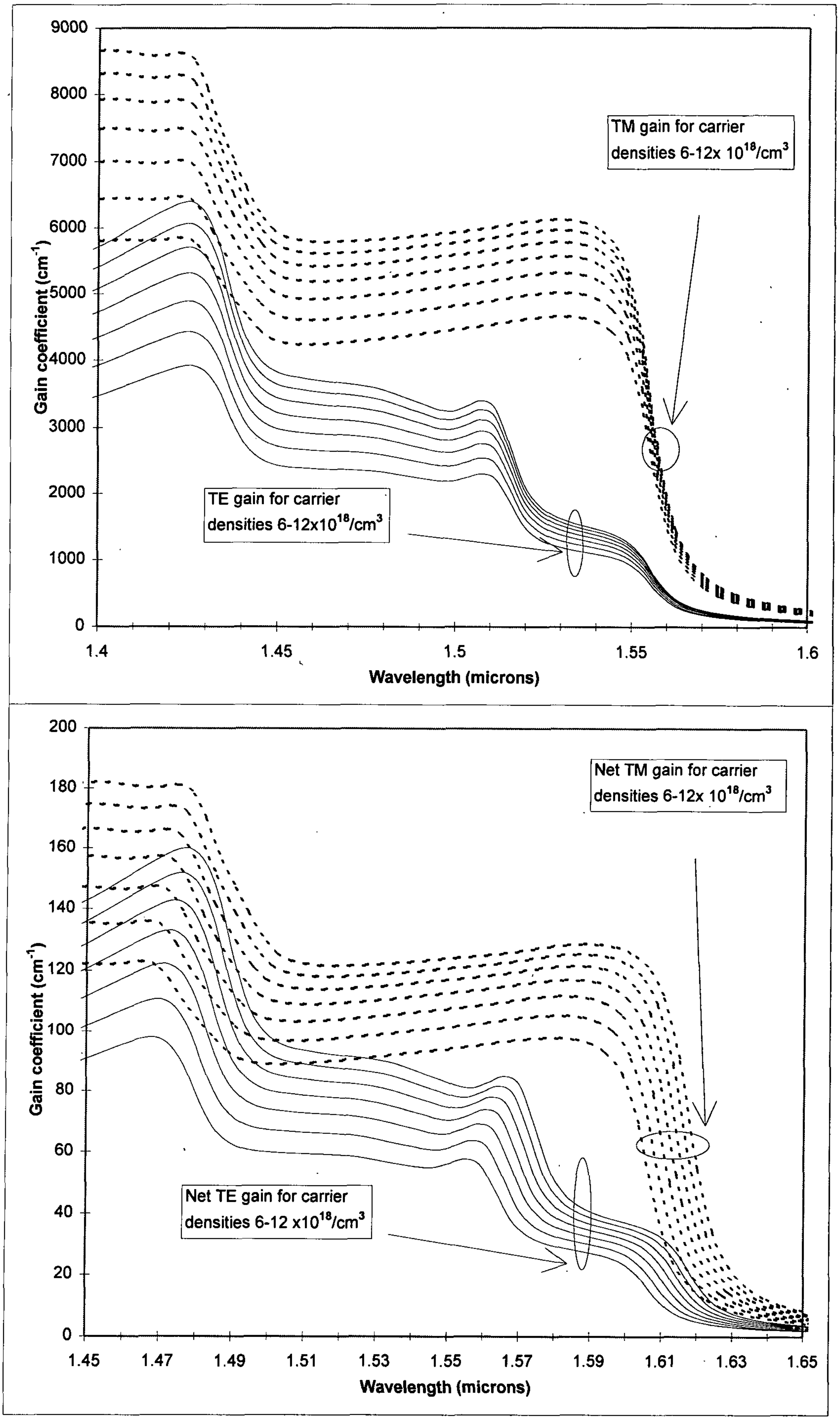

Figure 2: *The calculated room temperature TE and TM gains for Structure 1. The bottom figure includes optical confinement effects and bandgap narrowing whereas the top figure does not.*

InP / 500 Å $In_{0.74}Ga_{0.26}As_{0.57}P_{0.43}$ / 200 Å $In_{0.47}Ga_{0.53}As$ / 500 Å $In_{0.74}Ga_{0.26}As_{0.57}P_{0.43}$ / InP which yielded the values 0.025 & 0.021 for the TE and TM power confinement factors respectively. Bandgap narrowing was incorporated using data from [11] (see Appendix 3). The TE and TM gain curves do not cross for the wavelength range considered, but the difference between the two modes is at a minimum between 1.47 & 1.50 μm. This is also the region where both the TE and TM gains reach maxima.

Figure 3 shows the calculated net TE and TM gains (in decibels) [12] for both modes and the difference between the gains (in decibels) for a carrier density of $12\text{x}10^{18}/\text{cm}^3$ for three different optical cavity lengths. The gain scales linearly with increasing cavity length [12] but the injection current required to achieve a particular gain will increase with increasing cavity length [28]. Therefore, the gain difference between the two modes, which is a minimum at a wavelength of 1.485 μm, can be forced below 1 dB by choosing a cavity length of 125 μm or less. However, the use of a smaller cavity length also results in a reduction of device gain which is now approximately 10 dB at this wavelength. The polarization sensitivity for this device length is 2 dB or less between the wavelengths of 1.42 & 1.56 μm. If the cavity length is increased to 375 μm, the gain achievable at 1.485 μm is now approximately 27 dB but the sensitivity is just slightly below 3 dB. Some authors have examined structures using a smaller amount of tensile strain [1-5, 7], but the wavelength at which the best polarization insensitivity occurs is still less than 1.55 μm.

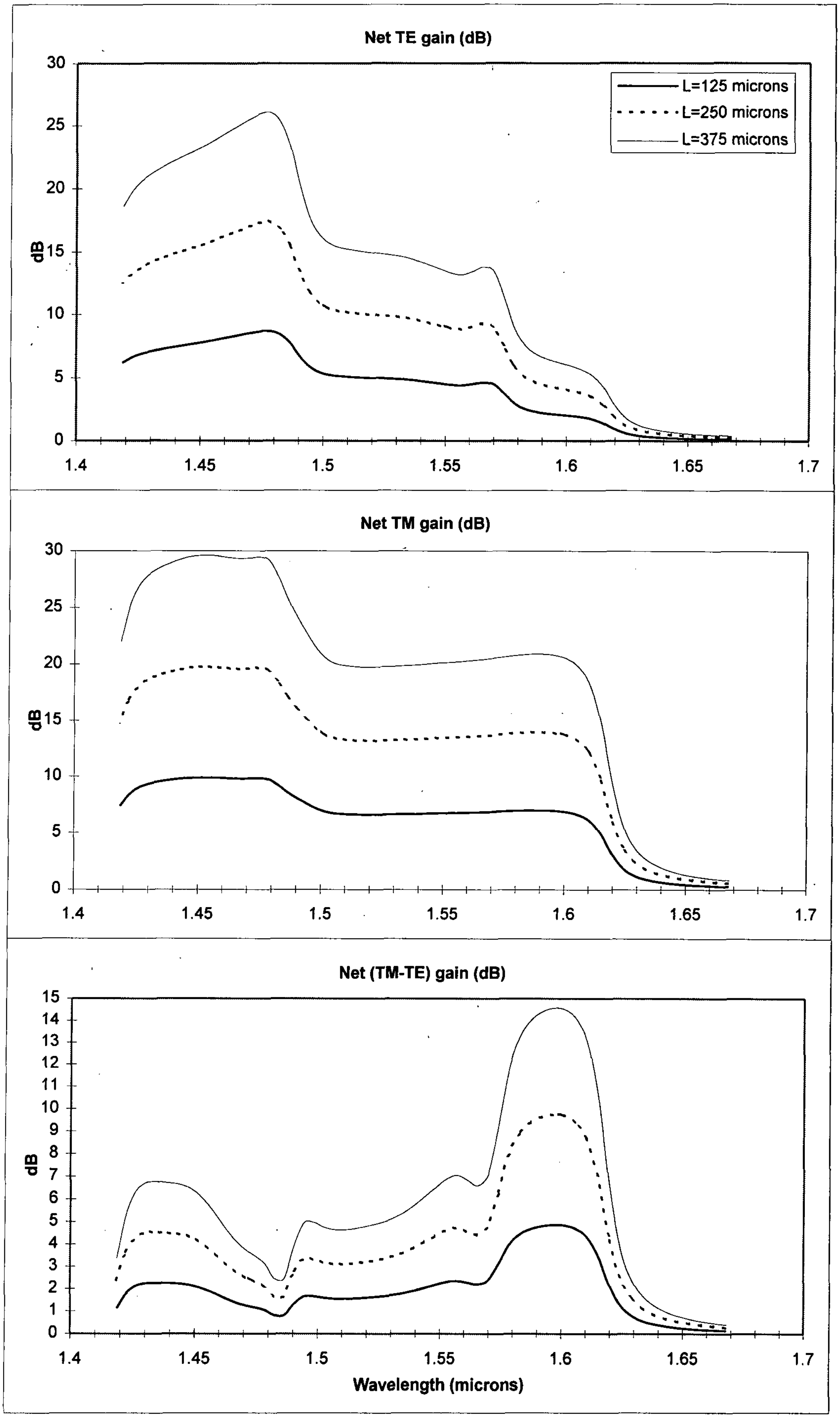

Figure 3: *The calculated net TE, TM and (TM-TE) gain at room temperature for Structure 1 for three device lengths at a carrier density of $12x10^{18}/cm^3$.*

In conclusion a reduction in polarization sensitivity has been demonstrated but neither this work nor that of other workers has produced a design for a single tensilely strained *InGaAs* quantum well which can satisfy the key amplifier requirements of high gain and low polarization sensitivity in the 1.55 μm wavelength region of the spectrum.

4.5 A stepped well active region which comprises two layers of opposite strain

The second type of structure examined had a stepped well active region consisting of two layers of opposite strain [28-30, 33].

The first structure of this type, which we will refer to as Structure 2, had 70 angstroms of 0.9% tensilely strained $In_{0.41}Ga_{0.59}As$ and 80 angstroms of 1.1% compressively strained $In_{0.79}Ga_{0.21}As_{0.8}P_{0.2}$ as the active region sandwiched between two layers of *InP*. Figure 4 shows the strained conduction and valence band line-ups.

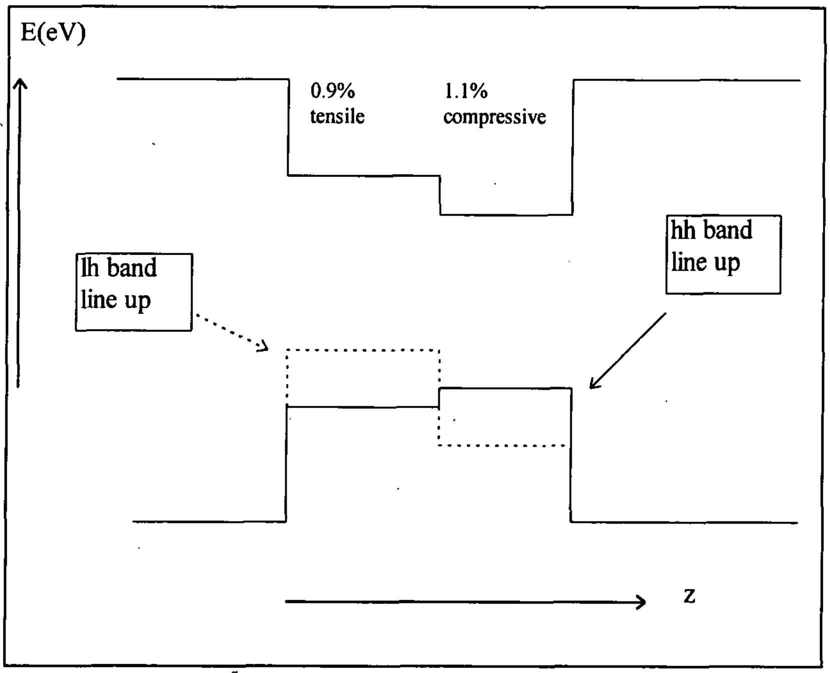

Figure 4: *Shows the strained conduction, heavy and light hole bandedge line-ups for Structure 2*

Figure 5 shows the bandstructure calculated using the ***k.p*** model. The material parameters are given in Appendix 4. Note that the spin degeneracy of the subbands found in symmetric wells is lifted away from $k_{||}=0$ in this structure.

The dominant envelope functions for the two lowest conduction and three highest valence subband states at $k_{||}=0$ are shown in Figure 6. The envelope function for the conduction subband, c1, exhibits some distortion from the form characteristic of a symmetric well as a result of the step at the tensile and compressive layer interface illustrated in Figure 4. However, the most significant differences are in the valence subband states. The valence states v1 & 2 are heavy hole in character and are strongly confined to the compressive material where the heavy hole bandedge is highest in Figure 4. The envelope function for the highest light hole subband, v3, exhibits some distortion from the typical symmetric well form as a result of the step at the tensile and compressive layer interface. However, the dominant envelope functions associated with c1 and v3 are generally delocalised across both the tensile and compressive layers.

Figure 7 (top) shows the calculated TE and TM gains at room temperature for a range of carrier densities (no optical confinement effects or bandgap narrowing included). The TE peaks at 1.55 and 1.43 μm are due to the transitions c1 to v1 and c2 to v1 respectively. The TM peak at 1.43 μm is due to the transition c1 to v3. For all carrier densities considered (n=4, 6, 8, 10, 12 & $20\text{x}10^{18}/\text{cm}^3$) the TE and TM gain spectra are closest or cross at approximately 1.44 μm. This crossover wavelength does not

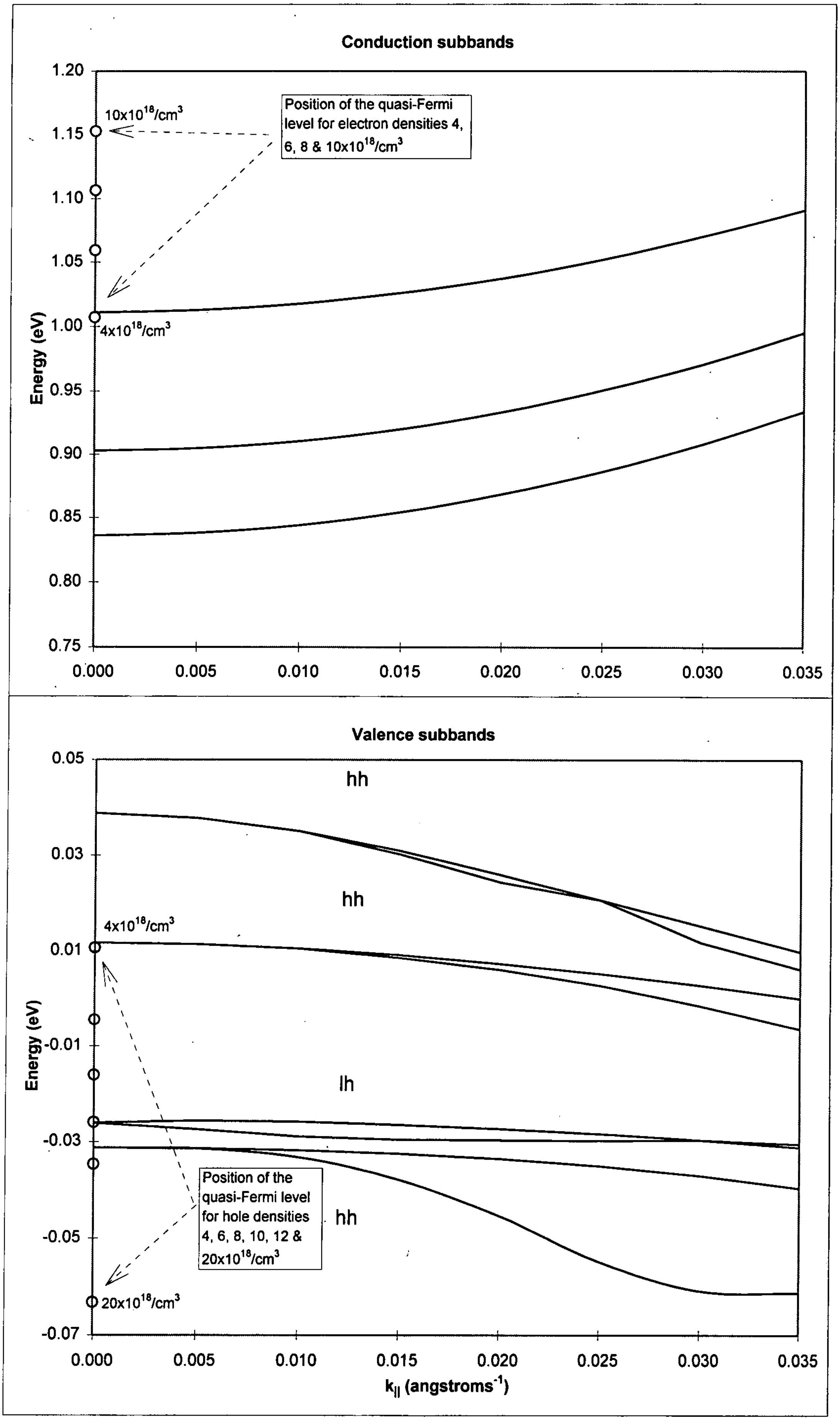

Figure 5: *Bandstructure for Structure 2, calculated using the* ***k.p*** *model. The structure is asymmetric which results in the double degeneracy of the subbands being lifted for* $k_{||}>0$.

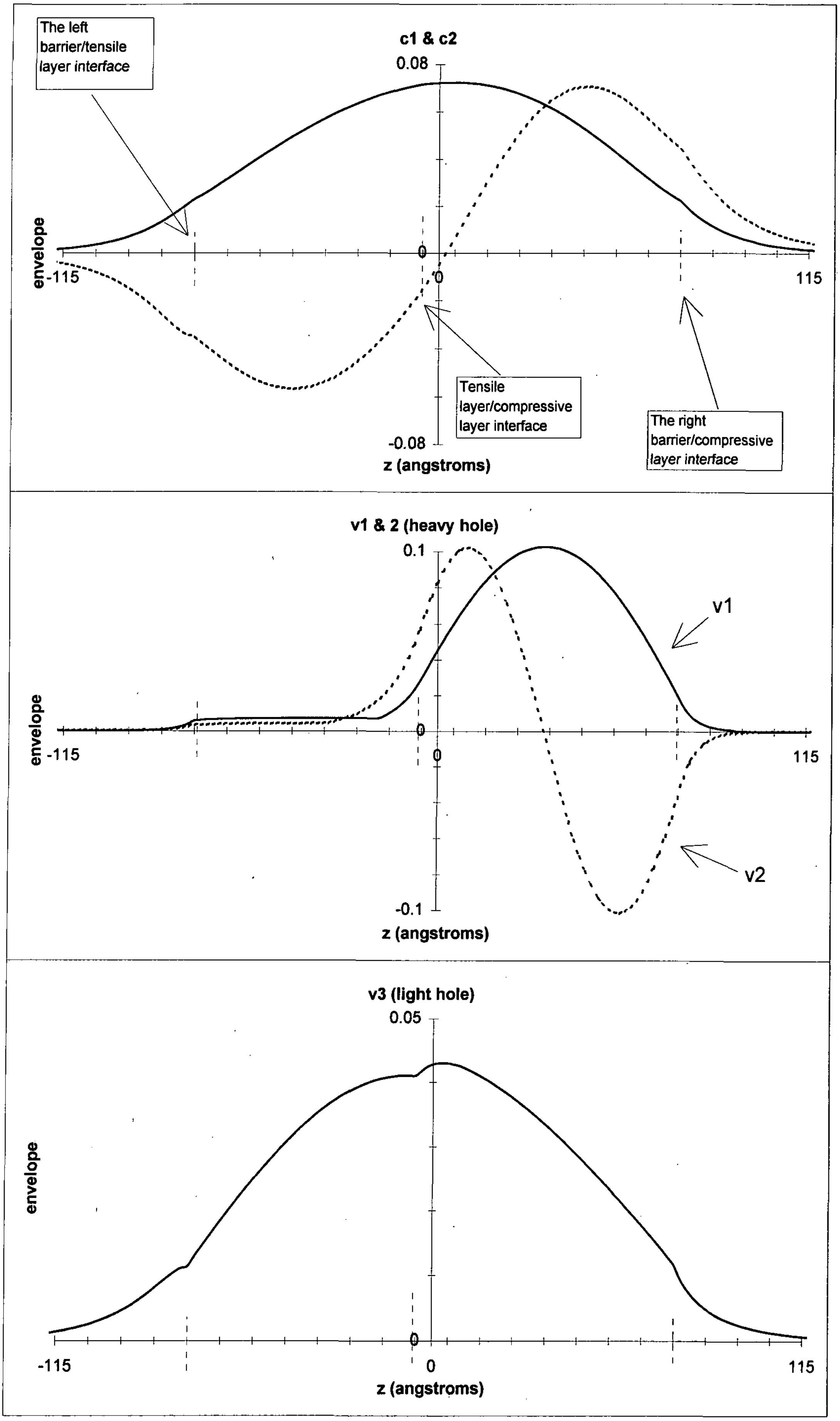

Figure 6: *Shows the envelope functions (real part) at $k_{\|}=0$ for the two lowest conduction and the three highest valence subbands calculated using the* ***k.p*** *model for Structure 2.*

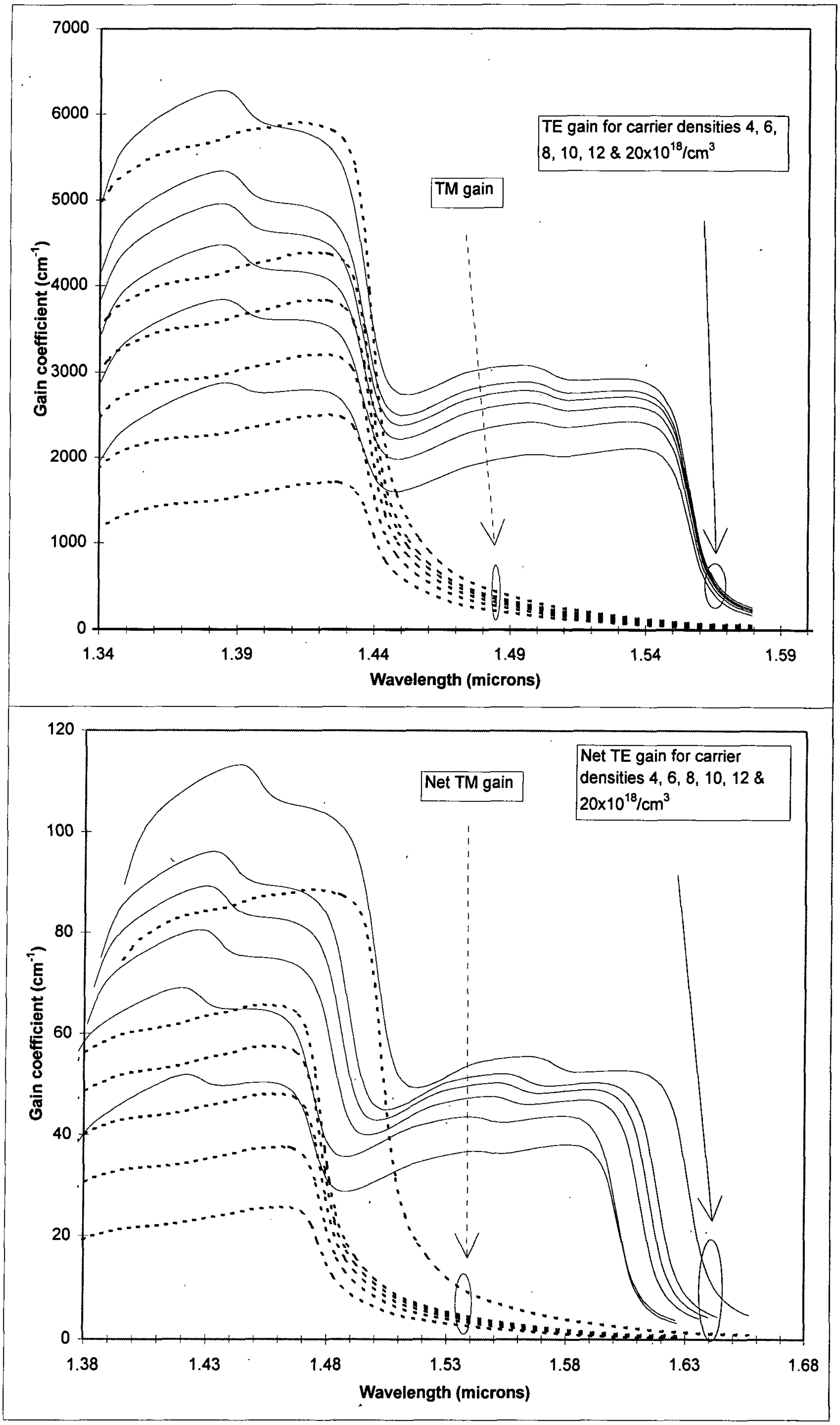

Figure 7: *The calculated room temperature TE and TM gains for Structure 2. The bottom figure includes optical confinement effects and bandgap narrowing whereas the top figure does not.*

shift much with increasing carrier density. The TE gain is generally larger than the TM gain for the wavelength region considered. However, for carrier densities above $12\text{x}10^{18}/\text{cm}^3$, the magnitude of the TM gain at 1.43 μm approaches that of the TE peak at the same wavelength, resulting in a secondary crossover at approximately 1.405 μm.

To estimate the net gain the power confinement factors were calculated using the results of references [8-10], and found to be 0.018 and 0.015 for the TE and TM modes respectively. Bandgap narrowing was included using the carrier density dependent values in Appendix 3. Figure 7 (bottom) shows the calculated net gain for a range of carrier densities. The wavelength of minimum sensitivity has shifted from 1.44 to 1.48 μm for carrier densities below $12\text{x}10^{18}/\text{cm}^3$, and to approximately 1.5 μm for larger carrier densities.

Figure 8 shows the calculated net TE, TM and TE-TM gain (in decibels) for a range of cavity lengths for a carrier density of $12\text{x}10^{18}/\text{cm}^3$. The maximum TE and TM gains occur between 1.40 and 1.49 μm. The point of minimum polarization sensitivity which occurs at 1.49 μm is also close to the wavelength region of maximum gain. However, in order to keep the polarization sensitivity below 1 dB at 1.49 μm, the device length must be less than 250 microns. This results in a maximum achievable gain of less than 10 dB for both modes at the wavelength of minimum sensitivity. The difference between the TE and TM gain also increases significantly for wavelengths above and below 1.49 μm.

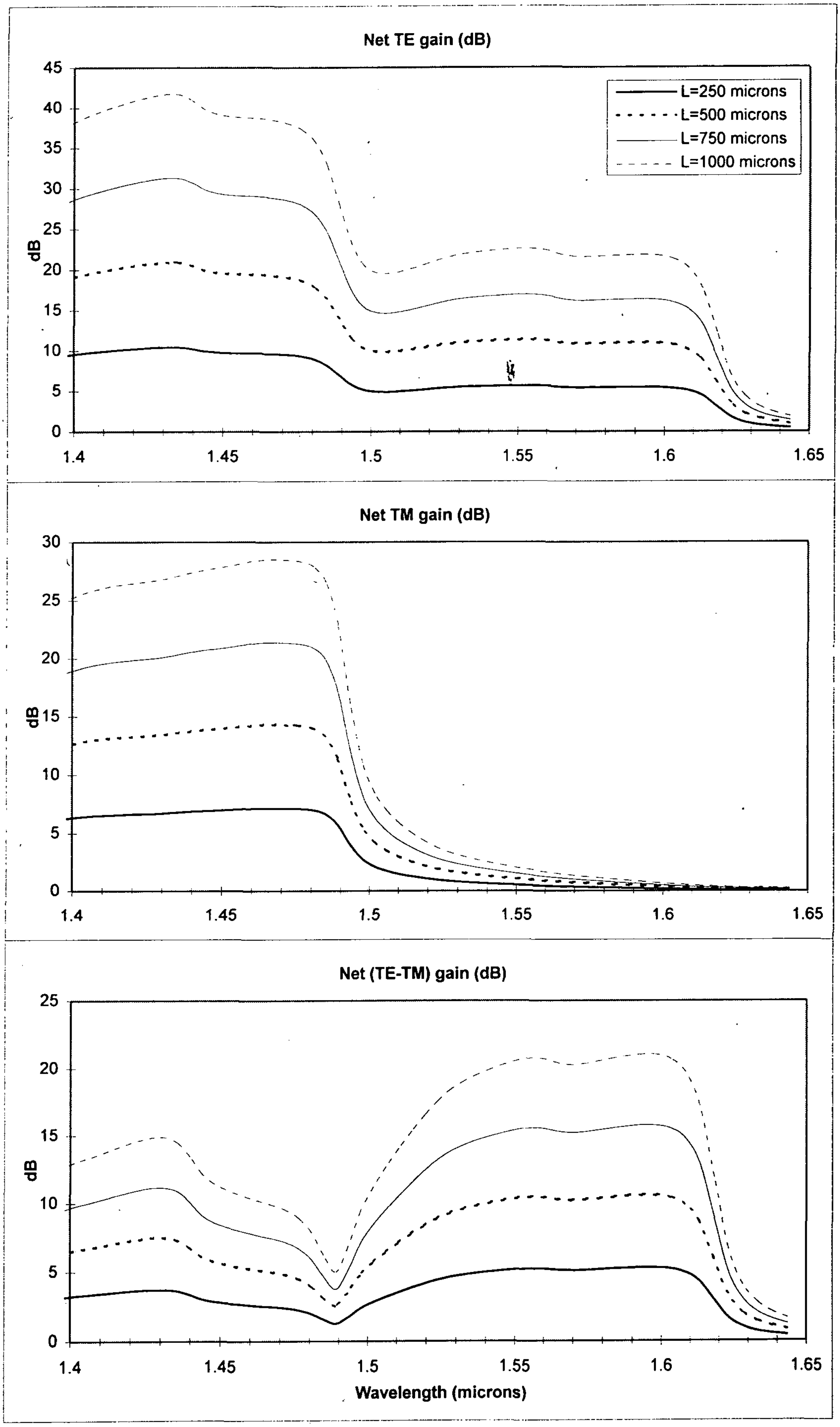

Figure 8: *The calculated net TE, TM and (TE-TM) gain at room temperature for Structure 2 for four device lengths at a carrier density of 12x10^{18}/cm^{3}.*

The second structure of the opposite strain type, which we will refer to as Structure 3, comprised 150 angstroms of 1% tensilely strained $In_{0.39}Ga_{0.61}As$ and 50 angstroms of 1.2% compressively strained $In_{0.8}Ga_{0.2}As_{0.8}P_{0.2}$ as the active region sandwiched between two layers of InP barriers. The bandedge alignments are similar to those in Figure 4. Figure 9 shows the calculated bandstructure. The material parameters are given in Appendix 5.

Figure 10 shows the relevant envelope functions at $k_{\|}=0$ for the two lowest conduction and three highest valence subbands. Again, the essential features of the behaviour can be understood in terms of the bandedge profile of the structure (Figure 4).

Figure 11 (top) shows the calculated TE and TM gains at room temperature for a range of carrier densities (no optical confinement effects or bandgap narrowing included). The TM gain dominates for wavelengths less than 1.48 μm. The TE peak at 1.47 μm is due to the transition c2 to v1, whilst the shoulder at 1.56 μm is due to the transition c1 to v1. The TM peak at 1.47 μm is due to the transition c1 to v2. The wavelength of minimum polarization sensitivity occurs between 1.47 and 1.48 μm, and does not shift greatly with increasing carrier density. The power confinement factors were calculated using references [8-10], and found to be 0.016 and 0.013 for the TE and TM modes respectively. The net gain as a function of carrier density is shown in Figure 11 (bottom). The wavelength of minimum polarization sensitivity is

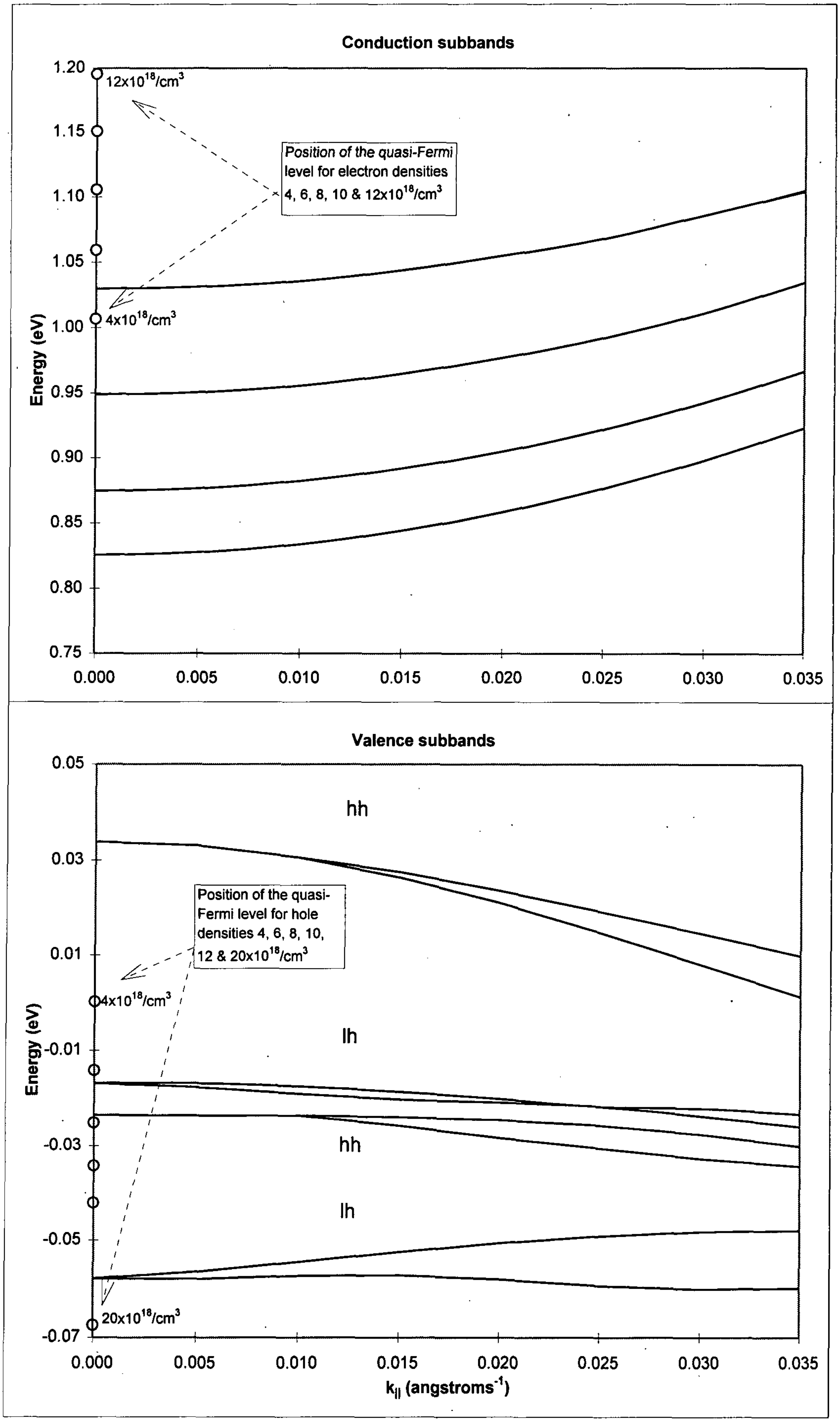

Figure 9: *Bandstructure for Structure 3, calculated using the* ***k.p*** *model. The structure is asymmetric which results in the double degeneracy of the subbands being lifted for* $k_{||}>0$.

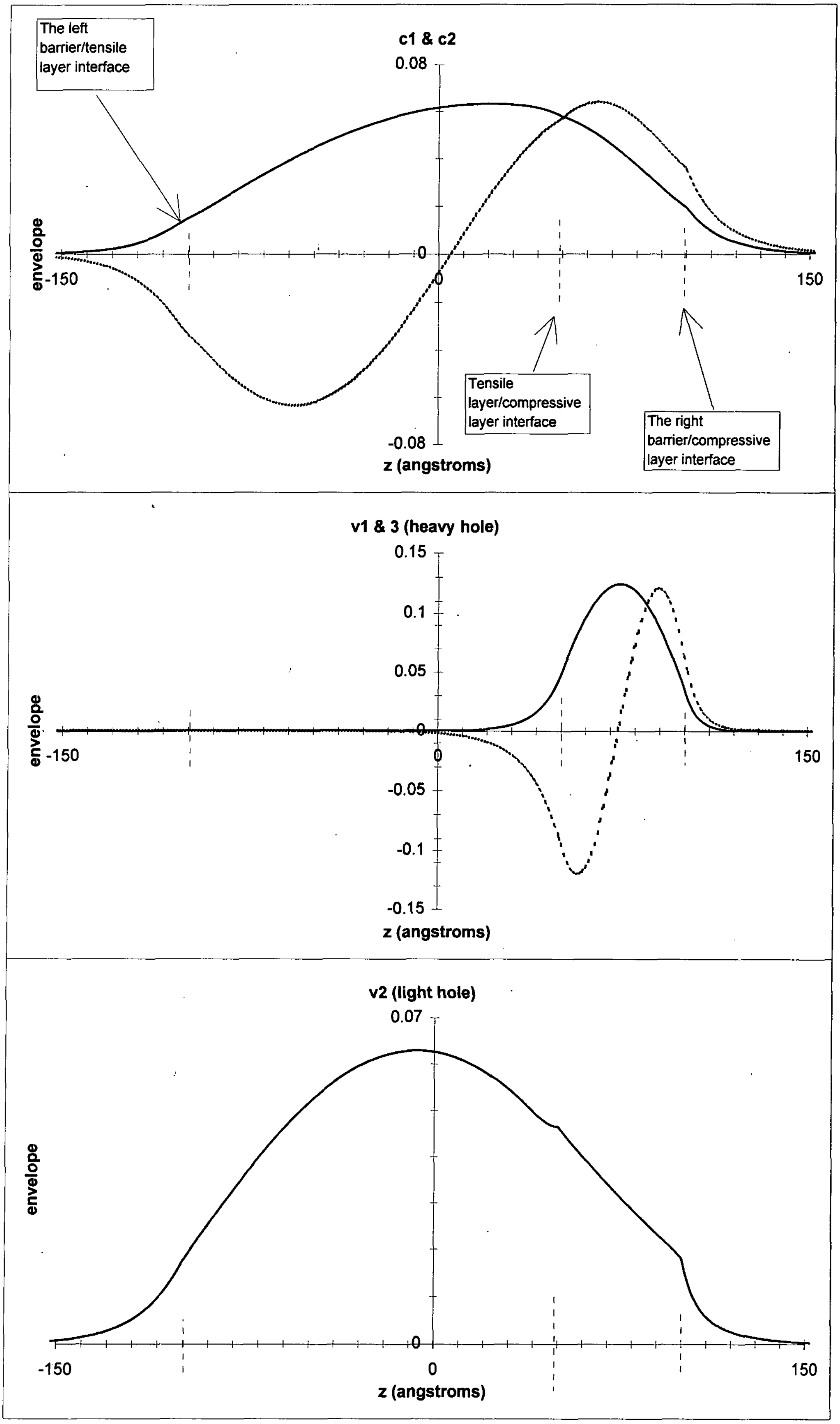

c1 & c2

The left barrier/tensile layer interface

Tensile layer/compressive layer interface

The right barrier/compressive layer interface

v1 & 3 (heavy hole)

v2 (light hole)

Figure 10: *Shows the envelope functions (real part) at $k_{||}=0$ for the two lowest conduction and the three highest valence subbands calculated using the* ***k.p*** *model for Structure 3.*

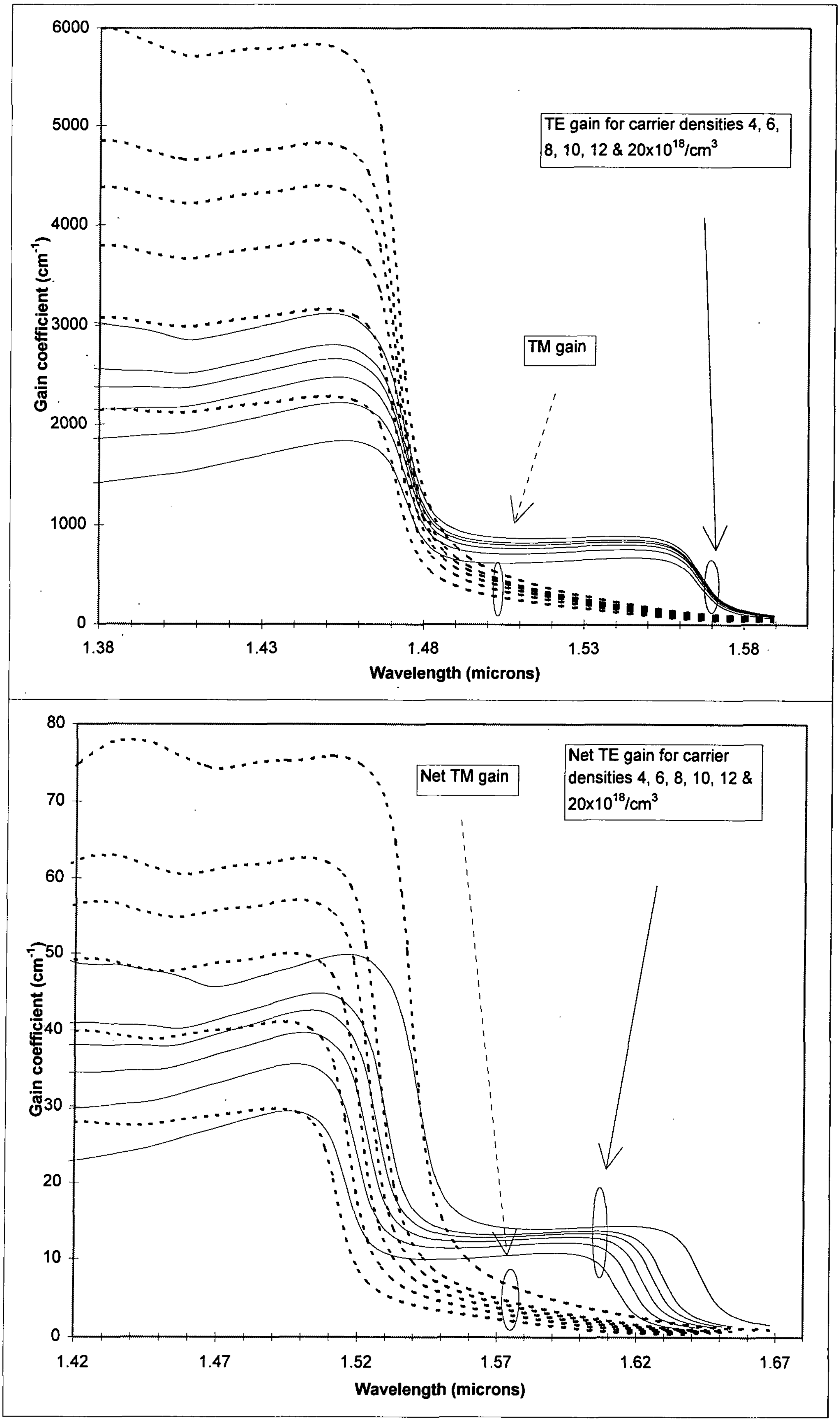

Figure 11: *The calculated room temperature TE and TM gains for Structure 3. The bottom figure includes optical confinement effects and bandgap narrowing whereas the top figure does not.*

at 1.5 μm for a carrier density of $4 \times 10^{18}/cm^3$. This shifts to approximately 1.55 μm at a carrier density of $20 \times 10^{18}/cm^3$.

Figure 12 shows the gain difference (in decibels) between the two modes as a function of wavelength and optical cavity length at a carrier density of $12 \times 10^{18}/cm^3$. The structure is polarization insensitive at 1.53 μm for all cavity lengths considered. However, for small shifts in wavelength about this point the polarization sensitivity increases rapidly. The wavelength at which the device is polarization insensitive is on the long wavelength shoulder of the main gain peak. This results in a maximum gain of approximately 14 dB for a device length of 1000 microns. In reality, the maximum gain could be bigger due to larger spectral broadening of this gain peak.

The third structure of the opposite strain type, which we will refer to as Structure 4, comprised 175 angstroms of 0.44% tensilely strained $In_{0.29}Ga_{0.71}As$ and 25 angstroms of 1.0% compressively strained $In_{0.78}Ga_{0.22}As_{0.8}P_{0.2}$ as the active region sandwiched between two layers of InP barriers. The bandedge alignments are similar to those in Figure 4. Figure 13 shows the calculated bandstructure. The material parameters are given in Appendix 6.

Figure 14 shows the relevant envelope functions at $k_{\|}=0$ for the lowest conduction and two highest valence subbands. Again, the essential features of the behaviour can be understood in terms of the bandedge profile of the structure (Figure 4).

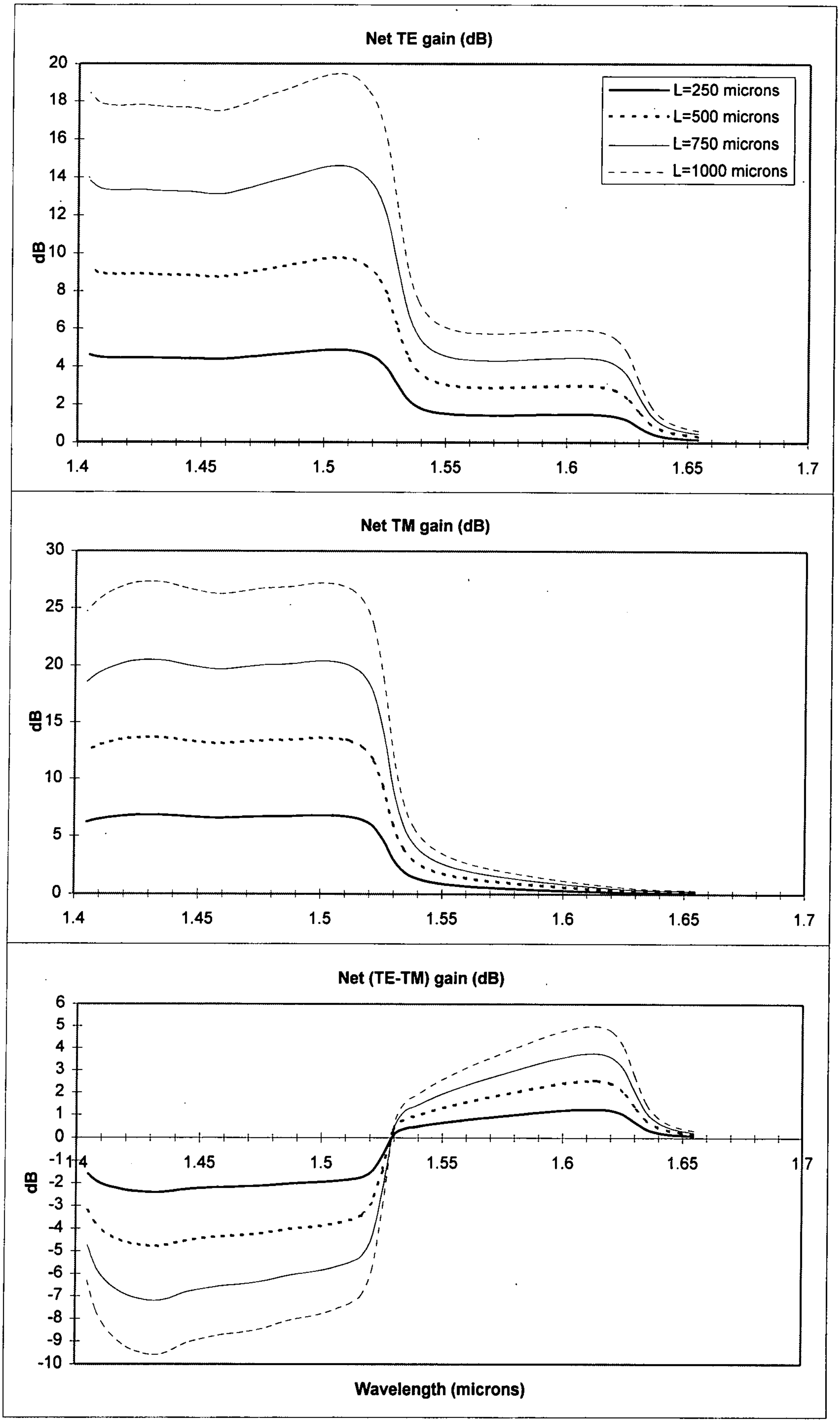

Figure 12: *The calculated net TE, TM and (TE-TM) gain at room temperature for Structure 3 for four device lengths at a carrier density of $12x10^{18}/cm^3$.*

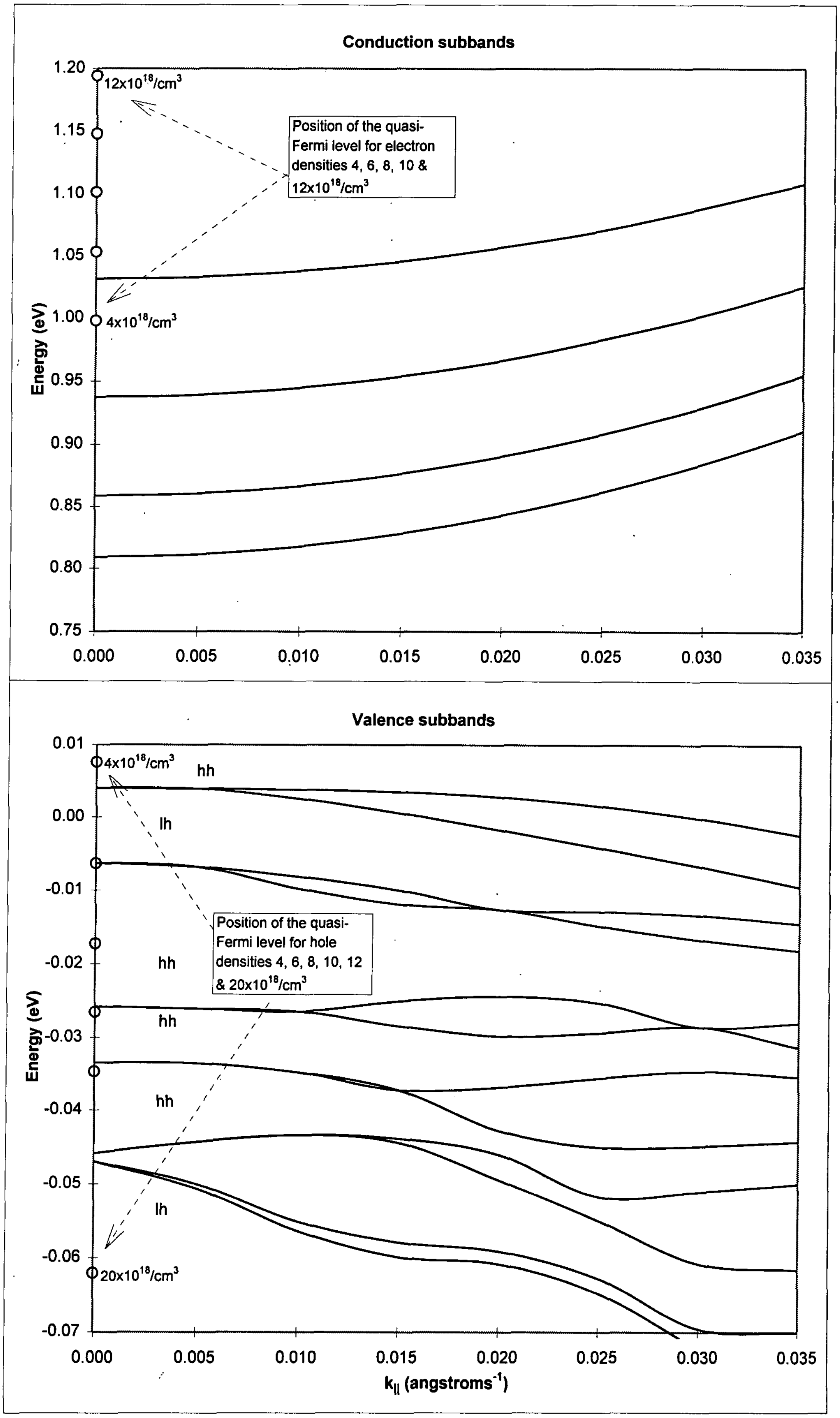

Figure 13: *Bandstructure for Structure 4, calculated using the* ***k.p*** *model. The structure is asymmetric which results in the double degeneracy of the subbands being lifted for* $k_{||}>0$.

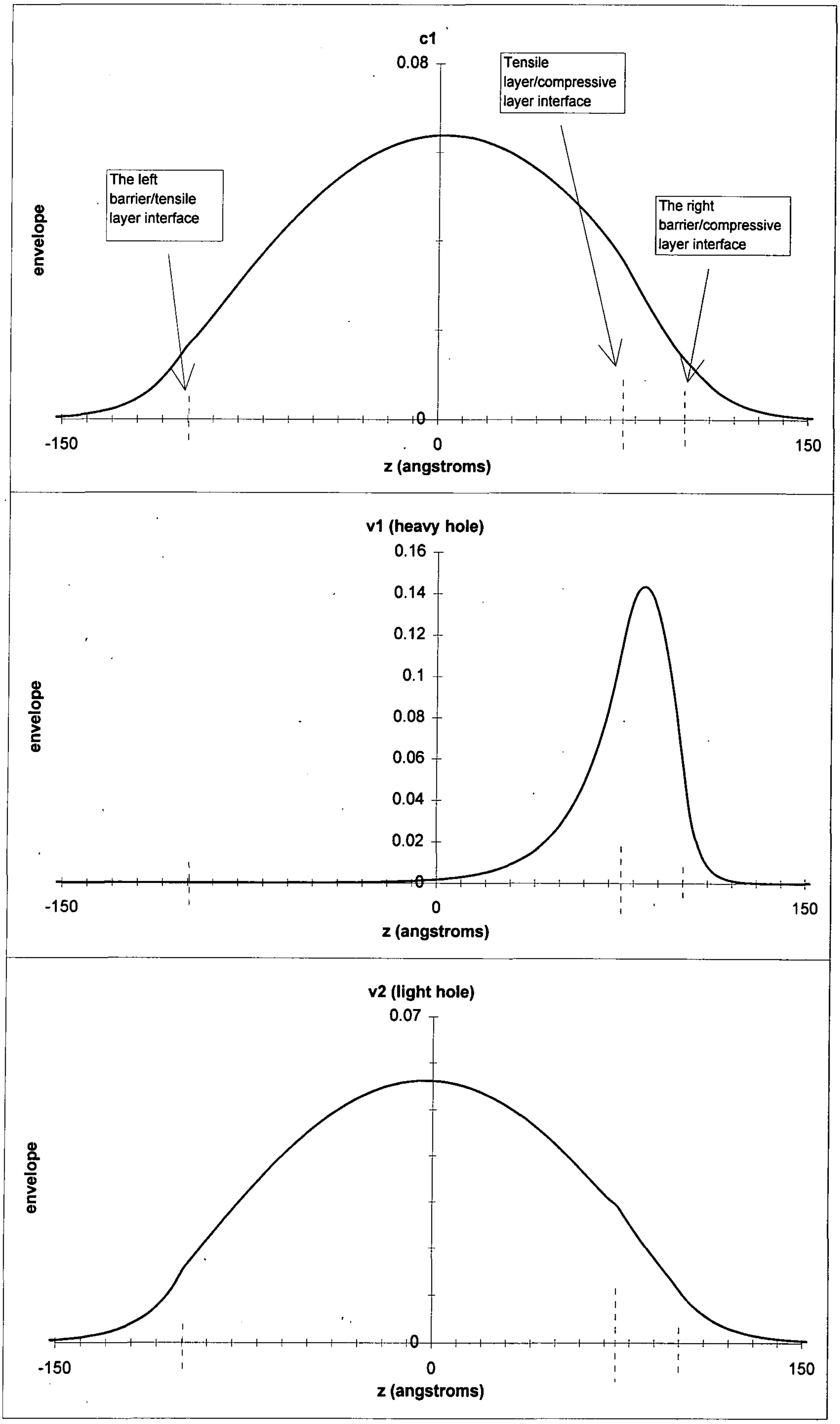

Figure 14: *Shows the envelope functions (real part) at $k_{||}=0$ for the lowest conduction and two highest valence subbands calculated using the* ***k.p*** *model for Structure 4.*

Figure 15 (top) shows the calculated TE and TM gains at room temperature for a range of carrier densities (no optical confinement effects or bandgap narrowing included). The TM gain dominates for all wavelengths of interest. The TE peak at 1.48 μm is due to the transition c1 to v3. The TM peak at 1.51 μm is due to the transition c1 to v2. The wavelength of minimum polarization sensitivity occurs at approximately 1.45 μm and does not shift greatly with increasing carrier density.

The power confinement factors were calculated using references [8-10], and found to be 0.025 and 0.021 for the TE and TM modes respectively. The net gain as a function of carrier density is shown in Figure 15 (bottom). The wavelength at which minimum sensivity occurs shifts from 1.48 μm at low carrier density towards 1.51 μm with increasing carrier density.

Figure 16 shows the gain difference (in decibels) between the two modes as a function of wavelength and optical cavity length at a carrier density of $12x10^{18}/cm^3$. The polarization sensitivity is less than 1 dB between 1.486 and 1.504 μm for a cavity length of 250 microns. This is also the wavelength region of maximum gain, which results in a value of 10 dB for this cavity length. A gain of approximately 20 dB could be realised for a cavity length of 500 microns, however the wavelength of minimum sensitivity (~1dB) is now 1.495 μm, and a small shift in wavelength about this point results in a significant increase in sensitivity.

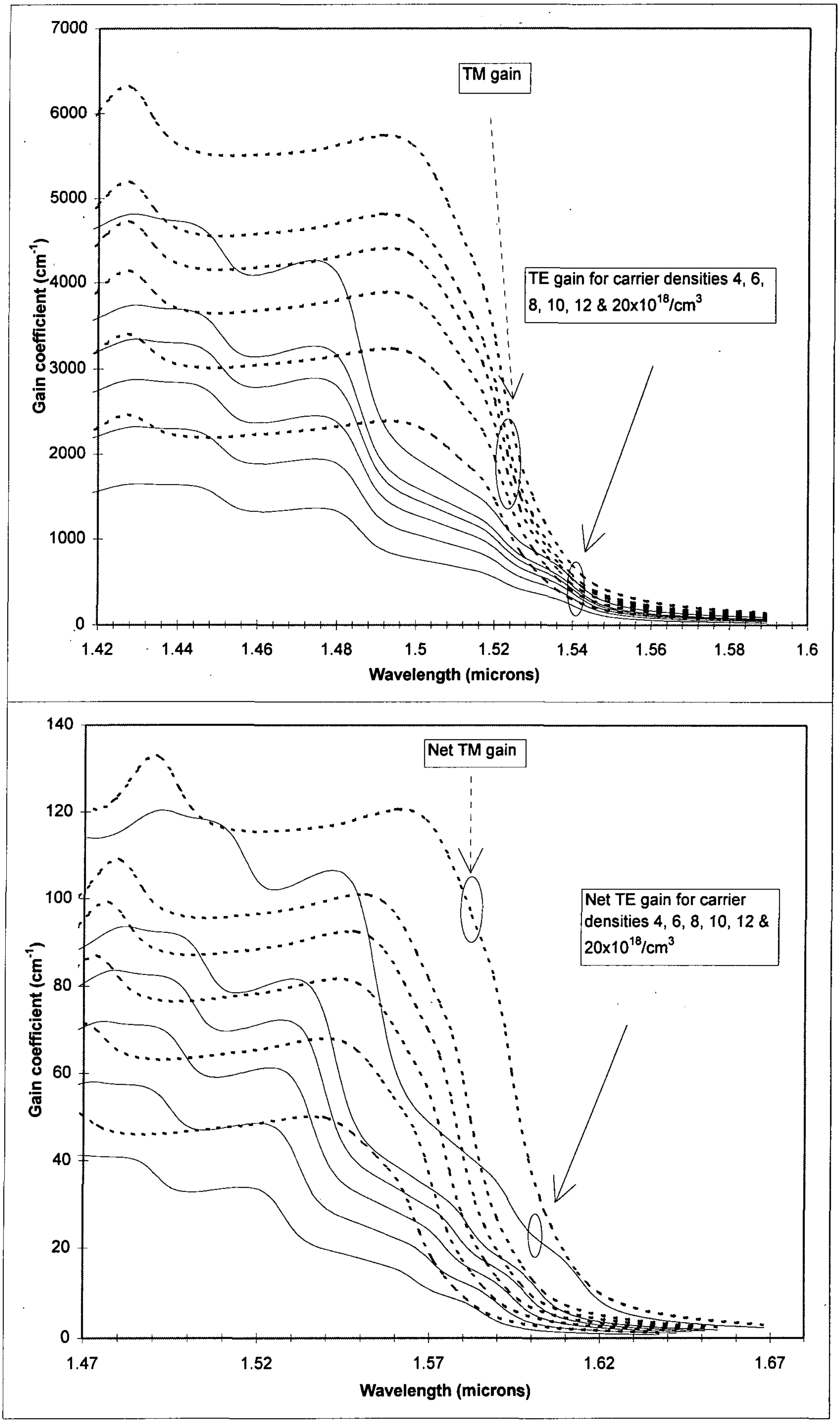

Figure 15: *The calculated room temperature TE and TM gains for Structure 4. The bottom figure includes optical confinement effects and bandgap narrowing whereas the top figure does not.*

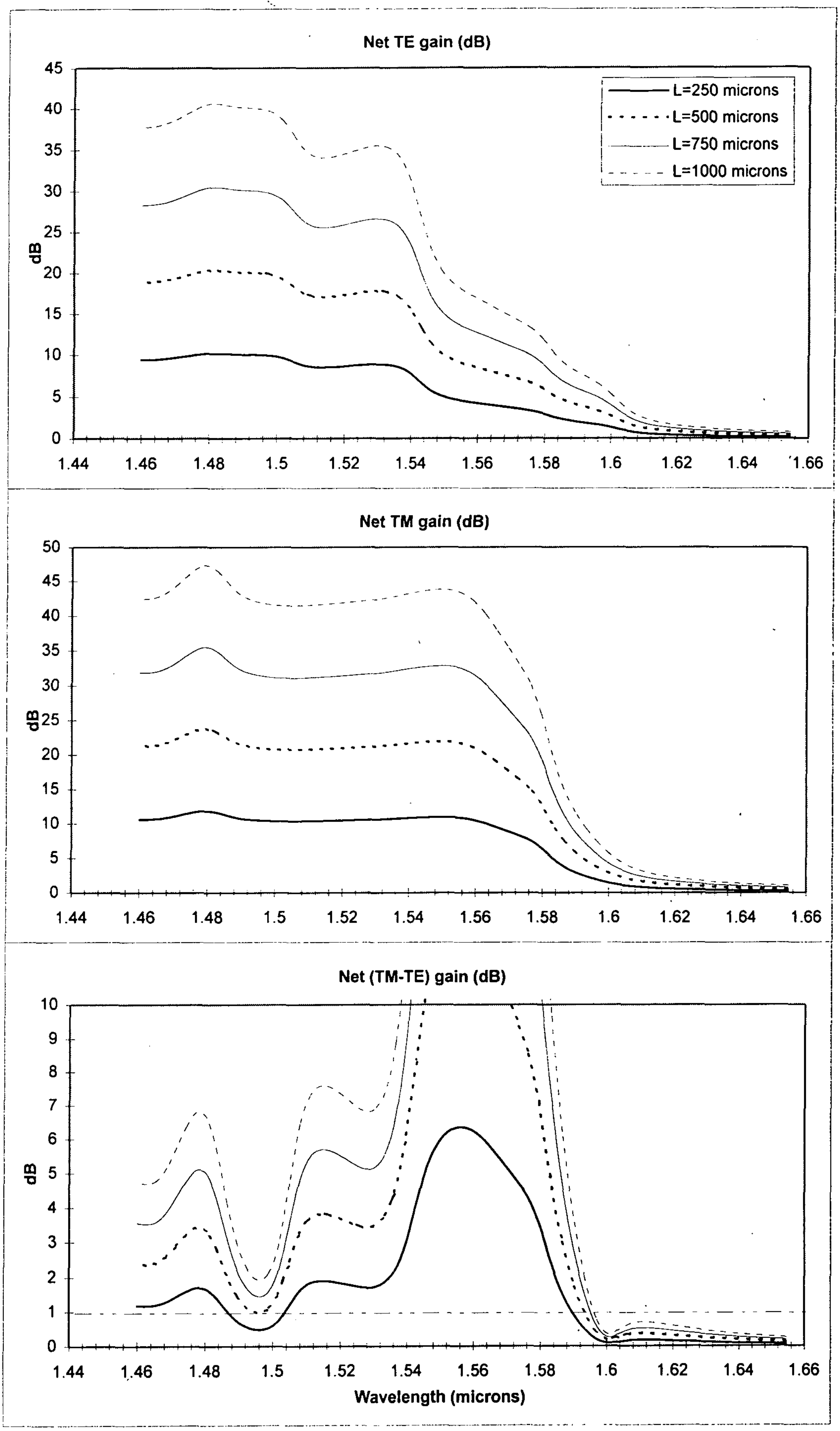

Figure 16: *The calculated net TE, TM and (TM-TE) gain at room temperature for Structure 4 for four device lengths at a carrier density of 12x10*^{18}*/cm*^{3}.

4.5 Discussion

Room temperature gain spectra have been calculated for two types of structure, namely a single tensilely strained quantum well (Structure 1), and a structure which had a stepped well active region which comprised two layers of opposite strain (Structures 2, 3 & 4).

Structure 1 manifested low polarization sensitivity at 1.485 μm, which is also the wavelength at which maximum TE and TM gain occurs. However, for a gain of approximately 27 dB the minimum polarization sensitivity is of the order of 3 dB for a cavity length of 375 microns. Further increases in tensile strain would push the point of minimum sensitivity to even shorter wavelengths due to the increased separation of the heavy and light hole states caused by shear stress. Therefore, a structure solely incorporating a single layer of tensilely strained *InGaAs* material is not suitable for polarization insensitive amplifier applications at 1.55 μm.

Structures 2, 3 & 4 showed varying degrees of performance. For Structure 2 it is possible to achieve a polarization sensivity of less than 1 dB at 1.49 μm but to the detriment of the maximum gain which is only 7 dB for a device length of 250 microns. Structure 3 shows polarization insensitivity at approximately 1.53 μm and it is possible to achieve a maximum gain at this wavelength of 14 dB for a cavity length of 1000 microns. For Structure 4, the polarization sensitivity is below 1 dB at approximately 1.5 μm and it is possible to achieve approximately 20 dB at this wavelength for a cavity length of 500 microns.

To highlight the relative performance of the four structures, the net TE, TM and TE-TM gain has been calculated at or close to device saturation for a cavity length of 250 microns and are shown in Figure 17. Structure 4 offers the best compromise of the structures considered. The polarization sensitivity is less than 1.5 dB between 1.47 and 1.546 μm (a bandwidth of 66 nm), and indeed is almost zero between 1.5 and 1.51 μm. The achievable gain for wavelengths between 1.47 and 1.546 μm is approximately 12 dB.

Another interesting result of this chapter is for Structure 2. A sixteen period superlattice version of Structure 2 has been examined experimentally [28,30,33], and results show that this structure has a polarization sensitivity of less than 1 dB between 1.5 and 1.585 μm (a bandwidth of 85 nm), and a maximum gain of 27 dB at 1.55 μm. Our calculated gain spectra, for a single period device, show both high polarization sensitivity and low maximum gain close to 1.5 μm. A one-dimensional effective mass calculation shows that for the superlattice there is a set of closely spaced conduction subbands at approximately halfway between the strained bulk conduction bandedges of both the tensile and compressive materials. The light hole subbands appear approximately halfway between the strained bulk light hole bandedges of both materials. The heavy hole subbands states are strongly confined in the compressive layer and essentially do not shift from the calculated energy for

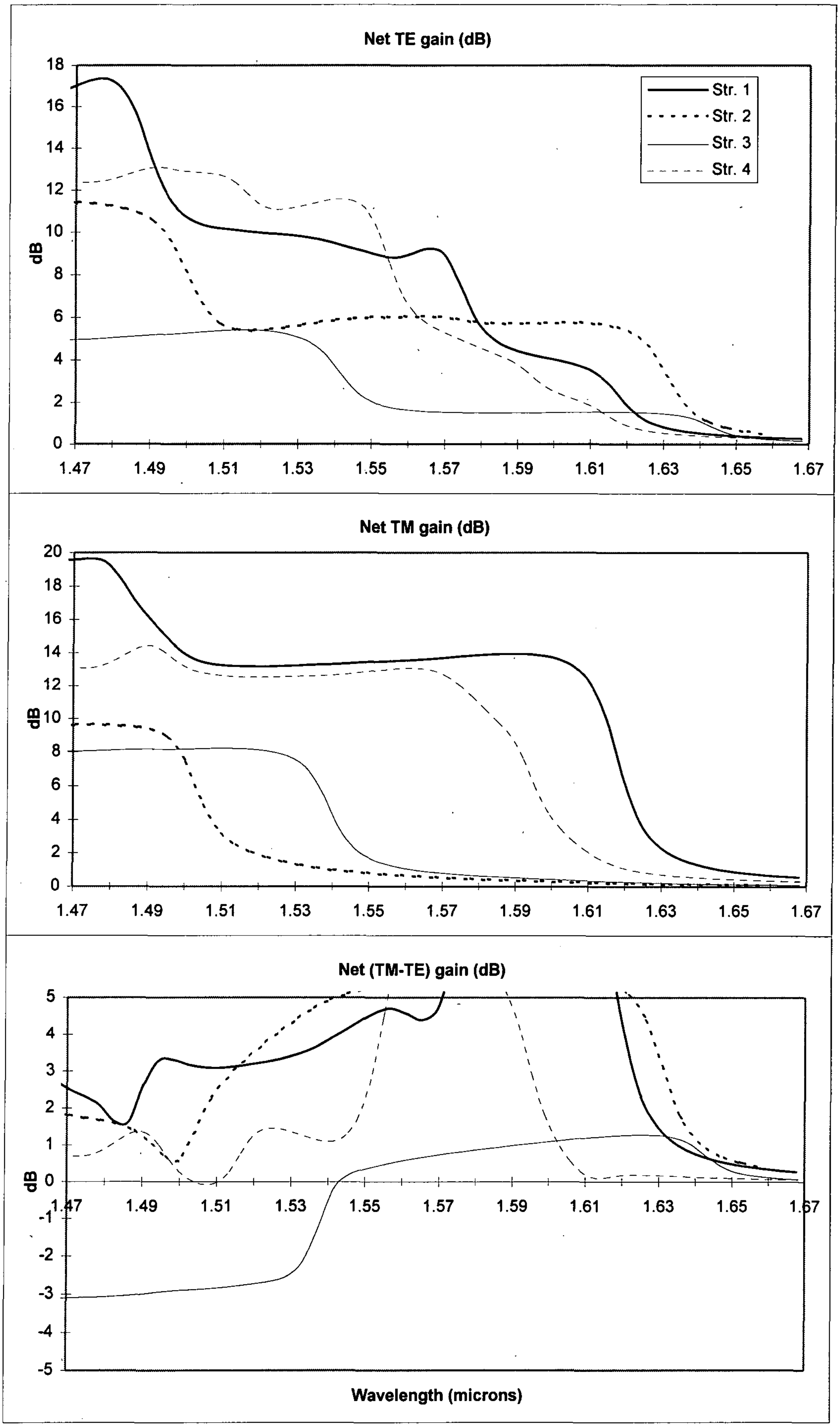

Figure 17: *The calculated net TE, TM and (TM-TE) gain at room temperature for Structures 1-4 for a device length of 250 microns at saturation.*

highest heavy hole subband for the one period structure [29]. Combining the results from the one-dimensional effective mass model, the calculated energy of the highest heavy subband for the one period structure obtained from the ***k.p*** model and the band offsets calculated using reference [46] suggest that the TE and TM gain peaks should occur at 1.58 and 1.52 μm respectively which is in reasonable agreement with the experimentally determined results.

This 'hybrid bulk' device offers greater and near equal optical confinement for both the TE and TM modes. The photon energy of the TM gain peak is essentially determined by the strained bulk bandedge line-ups, rather than quantum confinement effects on the respective conduction and light hole subbands. However, the photon energy of the TE gain peak is partly dependent on the compressive layer width which determines the heavy hole subband energies. The incorporation of tensile and compressive strain (see Section (2.3) of Chapter 2) also result in similar joint densities of states between conduction and heavy hole subbands, and between the conduction and light hole subbands. This combined with the fact that the c to hh and c to lh transitions are close in energy, produce very similar gain spectra close to the gain bandedge.

This argument receives further support from Godefroy *et al* [29], who examined a similar device to our Structure 4. Their structure was five periods of 140 angstroms of 0.5% tensilely strained $In_{0.46}Ga_{0.54}As$ and 67 angstroms of 1% compressively strained $In_{0.8}Ga_{0.2}As_{0.7}P_{0.3}$. Whilst the widths of the respective layers differ slightly from ours the overall width of a single period of the active region is nearly the same (actually 207 angstroms compared to our 200 angstroms). The most significant difference between our structure and theirs is the difference in compressive layer width. Their wider compressive layer will result in the confined heavy hole states shifting in energy towards the strained bulk heavy hole bandedge, which acts to push the TE gain peak (see Figure 15) towards longer wavelengths. This also results in the wavelength of minimum sensivity moving towards 1.55 μm. Their results showed a polarization sensitivity of less than 1 dB between 1.515 and 1.575 μm (a bandwidth of 60 nm), and a maximum gain of approximately 22 dB. The difference in compressive layer width does not account for the overall better performance of their device. The improvement mainly lies in the width of the structure as discussed for the comparison between Structure 2 and references [28,30,33].

The authors of references [14-17] examined multi-period structures using lattice matched *InGaAs* as the well material and tensilely strained barriers. The bandedge line-ups calculated using [46] showed that the conduction bandedge is lowest and the heavy hole and light hole bandedges are highest in the unstrained well material. However, the conduction and light hole states are still essentially delocalised across the whole structure, whilst the heavy hole states are strongly confined to the well material. Magari *et al* [17], showed that the TE gain peak appears at shorter wavelengths than the TM peak. This lends additional weight to the argument that the overall width of the structure determines the conduction and light hole subband energies and that the width of well material solely determines the heavy hole energies. If this were not the case then the expected gain spectra should show the TE peak at longer wavelengths than the TM peak by virtue of the fact that both the heavy hole and light hole bandedges are lowest and equal in the well material. The smaller effective mass of the light hole band in the well material should be manifested in the light hole energy being below that of the heavy hole energy, which would result in the TM peak being at a smaller wavelength compared to the TE peak. The device considered by Magari *et al* [17] showed very good polarization insensitivity at 1.55 μm and a maximum gain of 27.5 dB.

Summary

In this chapter room temperature gain calculations for both TE and TM modes were presented for four quantum well structures. The polarization dependence in the 1.55 μm wavelength region of the spectrum was discussed for a single tensilely strained quantum and three structures which incorporated both tensile and compressive material as the active layer. The results showed varying degrees of polarization insensitivity and maximum achievable gain close to 1.55 μm. Structure 4, which had 175 angstroms of 0.44% tensilely strained *InGaAs* and 25 angstroms of 1% compressively strained *InGaAsP* demonstrated a polarization sensitivity of less than 1.5 dB between 1.47 and 1.546 μm, and a gain of 12 dB over this wavelength range (at device saturation). A similar structure with five periods has been examined experimentally by other workers and shows good polarization insensitivity and maximum gain at 1.55 μm. The comparison between the theoretical and experimental results suggest that certain multi-period devices reported in the literature demonstrate better polarization insensitivity and produce larger gain in the 1.55 μm region of the spectrum. Although their growth is more involved the multi-period structures should also be more tolerant to slight deviations in layer thicknesses than the case for a single period structure.

References for Chapter Four

[1] M. Joma, H. Horikawa, M. Nakajima, M. Kawahara and T. Kamijoh, Fiber and Integrated Optics, **10**, 361 (1992)

[2] M. Joma, H. Horikawa, C. Q. Xu, K. Yamada, Y. Katoh and T. Kamijoh, Appl. Phys. Lett., **62**, 121 (1992)

[3] T. Aizawa, K. G. Ravikumar and R. Yamauchi, Electronic Letters, **29**, 21 (1993)

[4] K. Ravikumar, T. Aizawa and R. Yamauchi, IEEE Phot. Tech. Lett., **5**, 310 (1993)

[5] T. Aizawa, K. G. Ravikumar, S. Suzaki, T. Watanabe and R. Yamauchi, IEEE J. Quant. Elect., **30**, 585 (1994)

[6] D. Bour, K. J. Beernink, D. W. Treat, T. L. Paoli and R. L. Thornton, IEEE J. Quant. Elect., **30**, 2738 (1994)

[7] M. Joma, H. Horikawa, M. Nakajima and T. Kamijoh, Tech. Digest on Opt. Amp. and their Applics, 74 (1991)

[8] T. P. Pearsall, *GaInAsP Alloy Semiconductors*, 362 (1982)

[9] W. Streifer, D. R. Scifres and R. D. Burnham, Appl. Optics, **18**, 3547 (1979)

[10] D. Botez, IEEE J. Quant. Elect, **QE17**, 178 (1981)

[11] S. H. Park, J. I. Shim, K. Kudo, M. Asada & S. Arai, J. Appl. Phys., **72**, 279 (1992)

[12] M. Kaufman & A. Seidman, *Electronics Sourcebook for Technicians and Engineers*, 20-2 (1988)

[13] E. P. O' Reilly, G. Jones, A Ghiti and A. R. Adams, Electronics Letters, **27**, 1417 (1991)

[14] K. Magari, M. Okamoto, H. Yasaka, K. Sato, Y. Noguchi and O. Yasaka, Tech. Digest on Optical Amplifiers and their Applic., **13**, 30 (1990)

[15] M. Okamoto, K. Magari & Y. Itaya, "Polarization Controlled Semiconductor Photonic Devices by Strained-Barrier Superlattice Strutcures", 3rd Optoelectronics Conference (OEC90),184 (1990)

[16] K. Magari, M. Okamoto and Y. Noguchi, IEEE Trans. Phot. Tech. Lett., **3**, 998 (1991)

[17] K. Magari, M. Okamoto, Y. Suzuki, K. Sato, Y. Noguchi and O. Mikami, IEEE J. Quant. Elect., **30**, 695 (1994)

[18] P. J. A. Thijs, L. F. Tiemeijer, J. J. M. Binsma and T. van Dongen, IEEE J. Quant. Elect., **30**, 477 (1994)

[19] S. Dubovitsky, W. H. Steier, A. Mathur and P. D. Dapkus, IEEE J. Quant. Elect., **30**, 380 (1994)

[20] L. Tiemeijer, P. J. A. Thijs, T. V. Dongen, J. J. M. Binsma and E. J. Jansen, IEEE Phot. Tech. Lett., **6**, 1300 (1994)

[21] L. Tiemeijer, P. J. A. Thijs, T. van Dongen, R. W. M. Slootweg, J. M. M. van der Heijden, J. J. M. Binsma and M. P. C. M. Krijn, Appl. Phys. Lett., **62**,
826 (1993)

[22] A. Mathur and P. D. Dapkus, Appl. Phys. Lett., **61**, 2845 (1992)

[23] S. Dubovitsky, A. Mathur, W. H. Steier, P. D. Dapkus, IEEE Phot. Tech. Lett., **6**, 176 (1994)

[24] L. Tiemeijer, Proc. 21st Eur. Conf. on Opt. Comm. (ECOC'95 - Brussels), 259 (1995)

[25] T. Tanbun-Ek, N. A. Olsson, R. A. Logan, K. W. Wecht and A. M. Sergent, IEEE Phot. Tech. Lett., **3**, 103 (1991)

[26] B. I. Miller, Proc. 6th Int. Conf. on InP and Related Materials, 539 (1994)

[27] M. Newkirk, B. I. Miller, U. Koren, M. G. Young, M. Chien, R. M. Jopson and C. A. Burrus, IEEE Phot. Tech. Lett., **4**, 406 (1993)

[28] D. Sigogne, A. Ougazzaden, B. Mersali, J. Landreau, C. Amra and A. Ramdane, Proc. 21st Eur. Conf. on Opt. Comm. (ECOC'95 - Brussels), 267 (1995)

[29] A. Godefroy, A. Le Corre, F. Clerot, S. Salaun, S. Loualiche, J. C. Simon, L. Henry, C. Vaudry, J. C. Keromnes, G. Joulie and P. Lamouler, IEEE Phot. Tech. Lett., **7**, 473 (1995)

[30] A. Ougazzaden, D. Sigogne, A. Mircea, E. V. K. Rao, A. Ramdane and L. Silvestre, Electronic Lett., **31**, 1242 (1995)

[31] A. Mathur and P. D. Dapkus, IEEE Phot. Tech. Lett., **7**, 1243 (1995)

[32] U. Koren, B. I. Miller, M. G. Young, M. Chien, G. Raybon, T. Brenner, R. Ben-Michael, K. Dreyer and R. J. Capik, Electronic Lett., **32**, 111 (1995)

[33] D. Sigogne, A. Ougazzaden, D. Meichenin, B. Mersali, A. Carenco, J. C. Simon, I. Valiente, C. Vassallo and L. Billes, Electronic Lett., **32**, 1403 (1996)

[34] T. Saitoh and T. Mukai, Optical and Quantum Electronics, **21**, s47 (1989)

[35] N. A. Olsson, R. F. Kazarinov, W. A. Nordland, C. H. Henry, M. G. Oberg,

H. G. White, P. A. Garbinski and A. Savage, Electron. Lett., **25**, 1049 (1990)

[36] C. Q. Xu, K. Yamada, Y. Katoh, T. Kamijoh and M. Kawahara, Optical Amplifiers and their Applications, Santa Fe, New Mexico, Jun. **24-26**, 144 (1992)

[37] B. Mersali, G. Jelly, A. Accard, J. Lafragette, P. Doussiere, M. Lambert and B. Fernier, Electron. Lett., **26**, 124 (1990)

[38] T. Saitoh and T. Mukai, Optical and Quantum Electron., **21**, s47 (1989)

[39] T. Toyonaka, S. Tsuji, M. Haneda and Y. Ono, Electron. Lett., **27**, 941 (1990)

[40] G. Grosskopf, R. Ludwig, R. G. Waarts and H. G. Weber, Electron. Lett., **23**, 1387 (1987)

[41] N. A. Olsson, Electron. Lett., **24**, 1075 (1988)

[42] P. Doussiere, P. Garabedian, C. Graver, D. Bonnevie, T. Fillion, E. Derouin, M. Monnot, J. G. Provost, D. Leclerc and M. Klenk, IEEE Phot. Tech. Lett., **6**, 170 (1994)

[43] A. Kelly, I. F. Lealman, L. J. Rivers, S. D. Perrin and M. Silver, Electronics Lett., **32**, 1835 (1996)

[44] U. Koren, R. Ben-Michael, B. I. Miller, M. G. Young, M. Chien, H. H. Yaffe, G. Raybon and K. Dreyer, Electronic Lett., **30**, 1852 (1994)

[45] S. Kitamura, K. Komatsu and M. Kitamura, IEEE Phot. Tech. Lett., 6, 173 (1994)

[46] M. P. C. M. Krijn, Semicond. Sci. Technol., **6**, 27 (1991)

[47] E. O’ Reilly and G. P. Witchlow, Phys. Rev. B, **34**, 6030 (1986)

[48] E. O' Reilly, Semicond. Sci. Technol., **4**, 121 (1989)

[49] M. Sugawara, N. Okazaki, T. Fujii and S. Yamazaki, Phys. Rev. B, **48**, 8102 (1993)

[50] Y. Arakawa and Amnon Yariv, IEEE J. Quant. Elect., **QE-21**, 1666 (1985)

[51] M. Asada, IEEE J. Quant. Elect., **25**, 2019 (1989)

[52] A. I. Kucharska and D. J. Robbins, IEEE J. Quant. Elect., **26**, 443 (1990)

[53] M. P. Houng, Y. H. Wang and C. H. Chu, J. Appl. Phys., **77**, 6338 (1995)

CHAPTER FIVE

CONCLUSION

5.1 Summary

A method for the calculation of the electronic states and bandstructure for a strained quantum well structure using the eight band ***k.p*** method has been presented. The interfacial boundary conditions which result from an approximation to Burt's exact envelope function theory were calculated and included in the model. The effects of these boundary conditions on the bandstructure and wave functions were compared to those derived from the more widely used symmetrized Hamiltonian approach for a strained quantum well. The results showed that the Burt boundary conditions resulted in a very small shift in the conduction and light hole subband energies at zero in-plane wavevector. The corresponding envelope functions for both boundary conditions were virtually identical. For non-zero in-plane wavevector the effects are more pronounced but nevertheless did not result in any truly significant differences in the bandstructure.

The calculation of the optical absorption properties of a quantum well structure from the bandstructure and wave functions has also been described.

A simpler one-dimensional effective mass model has been developed which allows the rapid calculation of the electronic energies and dominant envelope functions at zero in-plane wavevector. The envelope functions of the other (minor) components of the wave functions were found by perturbation theory. The electronic energies and envelope functions calculated using the ***k.p*** and one-dimensional effective mass models generally showed excellent agreement.

In Chapter 3, a multi-layer ***k.p*** model was developed which allows the calculation of the electronic states and bandstructure for coupled quantum wells in an externally applied electric field. The bandstructure and electronic states were calculated for two asymmetric coupled quantum well structures and for three values of applied bias. The two structures were proposed by GEC-Marconi as possible candidates for 1.55 μm light intensity modulators. The calculated absorption spectra for Structure 1, which had an *n* doped *InP* region/100 angstroms of lattice matched *InGaAs*/20 angstroms *InP*/60 angstroms of lattice matched *InGaAs*/*p* doped *InP*, showed that at zero applied bias the base of an absorption shoulder appears at 1.55 μm. Application of a small applied bias resulted in a large increase in absorption at this wavelength. The calculations for Structure 2, which had an *n* doped *InP* region/60 angstroms of lattice matched *InGaAs*/20 angstroms *InP*/100 angstroms of lattice matched *InGaAs*/*p* doped *InP*, showed that a similar absorption shoulder extends through the wavelength of 1.55 μm. However, the application of bias only results in a small change in absorption at this wavelength. These results suggest that Structure 1 offers the better potential as an intensity modulator operating at 1.55 μm.

The theoretical results were also compared to experimental data, although it was recognised that the grown structures deviated from the target specifications. However the differences between the calculated and measured results were accounted for by recourse to a one-dimensional effective mass calculation based on the actual dimensions of the grown structure. As shown throughout the chapter, the results obtained from the one-dimensional effective mass model compared favourably with those obtained using the ***k.p*** model in respect of the electric field behaviour of the subband energies, envelope functions and optical matrix elements.

In Chapter 4, the polarization sensitivity of the gain for four optical amplifier structures was presented. Structure 1 was a 200 angstroms 0.44% tensilely strained *InGaAs* quantum well, and was predicted to produce a gain of approximately 27 dB and a polarization sensitivity of about 3 dB at 1.485 μm for a cavity length of 375 microns. However, neither this work nor that of other workers has produced a design for a single tensilely strained quantum well which can satisfy high gain and low polarization sensitivity at 1.55 μm.

The polarization sensitivity of the gain for three structures with a stepped well active region which incorporated both tensile and compressive material were calculated and presented. Structure 2 had 70 angstroms of 0.9% tensilely strained *InGaAs* and 80 angstroms of 1.1% compressively strained *InGaAsP* as the active region. The results showed a predicted maximum gain of 7 dB and minimum polarization sensitivity of less than 1 dB at 1.49 μm for a cavity length of 250 microns. Structure 3 had 150 angstroms of 1.0% tensilely strained *InGaAs* and 50 angstroms of 1.2% compressively strained *InGaAsP* as the active region. The results showed a maximum gain of approximately 14 dB and a zero polarization sensitivity at 1.53 μm for a cavity length of 1000 microns. The polarization sensitivity increases drastically for very small shifts in wavelength about 1.53 μm. Structure 4 had 175 angstroms of 0.44% tensilely strained *InGaAs* and 25 angstroms of 1.0% compressively strained *InGaAsP* as the active region. The results showed a maximum gain of approximately 12 dB and a polarization sensitivity of less than 1.5 dB between 1.47 and 1.546 μm for a cavity length of 250 microns (at device saturation). The polarization sensitivity is almost zero between the wavelengths 1.495 and 1.52 μm.

Structure 3 offers the lowest polarization sensitivity and high gain at 1.53 μm. However, the fact that the polarization sensitivity increases for even small shifts in wavelength about 1.53 μm make this device unsuitable as an amplifier candidate for an optical transmission system where signal pulses undergo wavelength dispersion. The resultant amplification could result in signal distortion. Structure 4, on the other hand, offers reasonable gain and low polarization sensitivity over a wide bandwidth. Whilst the polarisation sensitivity is not as low as can be achieved by Structure 3, an amplifier based on this structure would result in less signal distortion.

Multi-period versions of Structures 2 and 4 have been grown by other workers. The experimental results show high gain and polarization sensitivity of less than 1 dB at 1.55 μm, as well as wide bandwidths over which the polarization sensitivity is less than 1 dB. The overall width of these structures result in the formation of a set of conduction and light hole mini-bands close to their respective strained bulk bandedges. The states associated with the heavy hole subbands are strongly confined to the compressive layer. One-dimensional effective mass calculations show that the energy separation between the conduction and heavy hole subbands, and the conduction and light hole subbands are almost equal resulting in the TE and TM gain peaks appearing at the same wavelength. The presence of tensile and compressive strain acts to equalise the joint densities of states for the c-hh and c-lh transitions which result in the similar behaviour of TE and TM gain peaks versus wavelength. These experimental results suggest that the best polarization insensitive amplifier device will be a multi-period structure incorporating both tensilely strained barriers and compressively strained wells. The wider structure also produces large and almost equal TE and TM optical confinement factors, which means that large gains can be achieved for small optical cavity lengths.

5.2 Suggestions for further work

The calculations presented in Chapter 3 show that an asymmetric coupled quantum well structure offers the possibility of intensity modulation of light at a wavelength of 1.55 μm. The results presented were for TE polarized light only. The inclusion of a tensilely strained layer in a similar structure may offer the possibility of polarization insensitive intensity modulation at 1.55 μm. The multi-layer ***k.p*** model as it stands could be used to design such a structure.

The calculations presented in Chapter 4 examined the polarization sensitivity of single period stepped quantum well structures which incorporated both tensile and compressive layers. The calculated results showed that two of these single period devices displayed the required characteristics for polarization insensitive amplifier applications. However, experimental results for multi-period structures showed much improved performance compared to the theoretical results for the single period structures. Whilst the improved performance of the multi-period structures was inferred by recourse to a much simpler one-dimensional effective mass model, a more accurate calculation is required to confirm the result. It is unlikely that the eight band multi-layer ***k.p*** model as it stands could be used to model such wide structures due to numerical instability in the complex bandstructure approach which tends to become a problem for large structure widths. An alternative approach is to consider the structure as an infinite superlattice and make use of the periodicity of the system.

The multi-layer ***k.p*** model has been developed with flexibility in mind and has applications beyond the specific devices considered in this thesis. These applications could include quantum well cascade lasers, piezo-electric structures and devices which require self-consistent calculations due to the effects of carrier charge.

APPENDIX ONE

Room temperature material parameters used for bandstructure calculations in Chapter 2

	$\mathbf{In_{0.47}Ga_{0.53}As}$	$\mathbf{In_{0.74}Ga_{0.26}As_{0.57}P_{0.43}}$
$\mathbf{E_g}$ **(eV)**	0.827	1.015
Δ **(eV)**	0.321	0.237
P	6.029	6.451
s	-17.081	-22.303
γ_1	-4.321	-5.171
γ_2	-3.292	-3.568
γ_3	-2.703	-3.078
c	-7.035	-
m	0.662	-
l	-4.579	-
$\varepsilon_{\|\|}$	0.0044	0
ε_{zz}	-0.0043	0
$\Delta\mathbf{E_{voff}}$ **(eV)**	0.120	0

The material parameters for the four binary materials (InAs, GaAs, GaP and InP) were obtained from references [1,2]. E_g, Δ and ΔE_{voff} (the valence band offset), for the ternary/quaternary material in question, were calculated using the method proposed by Krijn [3]. All other ternary/quaternary material parameters are linearly interpolated from the binary values. P, s, γ_1, γ_2 and γ_3 are calculated using eq.(15)-(20) in Chapter 2.

[1] M. Silver and E. P. O' Reilly, IEEE J. of Quant. Elect., **31**, 1193 (1995)

[2] O. Madelung, Ed., Landolt-Bornstein, New Series, Group III, Vol. 17 (Springer, 1982)

[3] M. P. C. Krijn, Semicond. Sci. Technol., **6**, 27 (1991)

APPENDIX TWO

Room temperature material parameters used for bandstructure calculations in Chapter 3

	$In_{0.53}Ga_{0.47}As$	**$In_{0.55}Ga_{0.45}As$**	**InP**
E_g (eV)	0.764	0.743	1.35
Δ (eV)	0.324	0.325	0.110
P	5.980	5.961	5.812
s	-17.831	-18.035	-11.895
γ_1	-4.689	-4.802	-1.830
γ_2	-3.485	-3.545	-1.808
γ_3	-2.883	-2.938	-1.358
c	-	-6.861	-
m	-	0.683	-
l	-	-4.582	-
$\varepsilon_{\|\|}$	0	-0.0012	-
ε_{zz}	0	0.0011	-
ΔE_{voff} (eV) wrt InP valence bandedge	0.336	0.341	0

The conduction and valence band offsets for structures 1 and 2 considered in Chapter 3

Structure 1

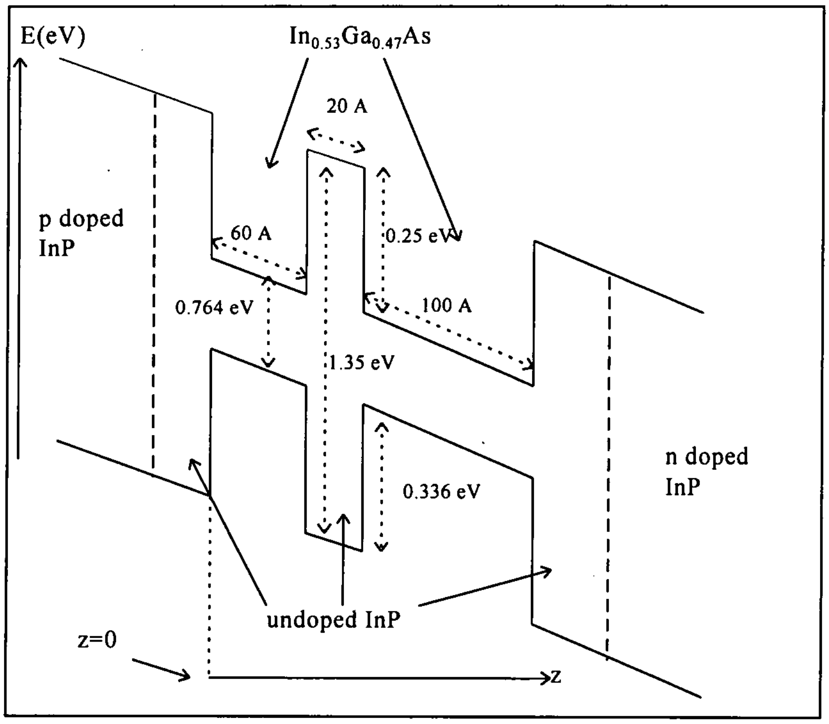

Structure 2

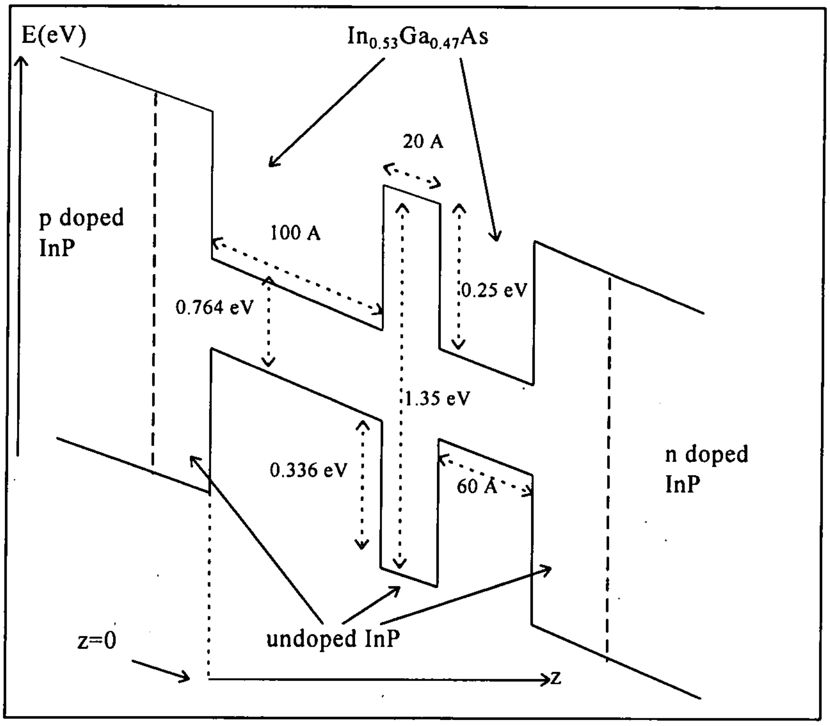

APPENDIX THREE

Bandgap narrowing as a function of carrier density

Carrier density ($\times 10^{18}/cm^3$)	**Carrier sheet density ($\times 10^{12}/cm^2$)**	**Bandgap narrowing energy (meV)**
1	1.000	14.6
2	1.587	20.3
3	2.080	21.7
4	2.520	22.9
5	2.924	24.1
6	3.302	25.2
7	3.659	26.2
8	4.000	27.2
9	4.327	28.1
10	4.642	29.0
11	4.946	29.9
12	5.242	30.7
20	7.368	36.8

The bandgap narrowing shown in the table above obtained from [1]

[1] S. H. Park, J. I. Shim, K. Kudo, M. Asada & S. Arai, J. Appl. Phys., **72**, 279 (1992)

APPENDIX FOUR

Room temperature material parameters used for bandstructure calculations for Structure 2 in Chapter 4

	$In_{0.41}Ga_{0.59}As$	**$In_{0.79}Ga_{0.21}As_{0.8}P_{0.2}$**	**InP**
E_g (eV)	0.894	0.735	1.35
Δ (eV)	0.320	0.302	0.110
P	6.060	6.122	5.812
s	-16.135	-22.617	-11.895
γ_1	-3.908	-5.817	-1.830
γ_2	-3.076	-3.996	-1.808
γ_3	-2.500	-3.415	-1.358
c	-7.166	-6.444	-
m	0.647	0.640	-
l	-4.576	-4.577	-
$\varepsilon_{\|\|}$	0.009	-0.011	-
ε_{zz}	-0.008	0.012	-
ΔE_{voff} (eV) wrt InP valence bandedge	0.304	0.319	0

APPENDIX FIVE

Room temperature material parameters used for bandstructure calculations for Structure 3 in Chapter 4

	$In_{0.39}Ga_{0.61}As$	**$In_{0.8}Ga_{0.2}As_{0.8}P_{0.2}$**	**InP**
E_g (eV)	0.916	0.725	1.35
Δ (eV)	0.320	0.302	0.110
P	6.067	6.110	5.812
s	-15.778	-22.676	-11.895
γ_1	-3.760	-5.862	-1.830
γ_2	-3.000	-4.021	-1.808
γ_3	-2.428	-3.437	-1.358
c	-7.210	-6.420	-
m	0.641	0.643	-
l	-4.576	-4.577	-
$\varepsilon_{\|\|}$	0.010	-0.012	-
ε_{zz}	-0.010	0.013	-
ΔE_{voff} (eV) wrt InP valence bandedge	0.299	0.321	0

APPENDIX SIX

Room temperature material parameters used for bandstructure calculations for Structure 4 in Chapter 4

	$In_{0.47}Ga_{0.53}As$	**$In_{0.78}Ga_{0.22}As_{0.8}P_{0.2}$**	**InP**
E_g (eV)	0.827	0.744	1.35
Δ (eV)	0.321	0.301	0.110
P	6.029	6.134	5.812
s	-17.081	-22.552	-11.895
γ_1	-4.321	-5.771	-1.830
γ_2	-3.292	-3.971	-1.808
γ_3	-2.703	-3.393	-1.358
c	-7.035	-6.468	-
m	0.662	0.637	-
l	-4.579	-4.577	-
$\varepsilon_{\|\|}$	0.0044	-0.010	-
ε_{zz}	-0.0043	0.011	-
ΔE_{voff} (eV) wrt InP valence bandedge	0.320	0.316	0

APPENDIX SEVEN

Calculation of the optical confinement factors

The refractive index for $Ga_xIn_{1-x}As_yP_{1-y}$ is estimated using the following equation [1]

$$n^2 = 1 + \frac{E_d}{E_0} + \frac{E_d}{E_0^3}E^2 + \frac{\eta E^4}{\pi}\ln\left[\frac{2E_0^2 - E_g^2 - E^2}{E_g^2 - E^2}\right]$$

where

n = refractive index

$$\eta = \frac{\pi E_d}{2E_0^3\left(E_0^2 - E_g^2\right)}$$

E = photon energy

$E_0 = 3.391 - 1.652y + 0.863y^2 - 0.123y^3$

$y = As$ content

$E_\mathrm{d} = 28.91 - 9.278y + 5.626y^2$

$E_\mathrm{g} = 1.35 - 0.72y + 0.12y^2$ = bulk energy gap

In the above equations, the lattice-matched condition (to *InP*), $y = 2.197x$, has been used.

The TE power confinement factor for the active region of the structure in question is estimated using the method proposed in [2,3] by

$$\Gamma_\mathrm{TE} = \frac{\gamma N_w t_w}{\bar{t}}$$

where

$$\gamma = \frac{D^2}{D^2+2}$$

$$D = \frac{2\pi\bar{t}}{\lambda}\sqrt{\bar{n}^2 - n_c^2}$$

$\bar{t} = N_w t_w + N_b t_b$

N_w = number of wells

t_w = well layer width

N_b = number of barriers

t_b = barrier layer width

$$\bar{n} = \frac{N_w t_w n_w + N_b t_b n_b}{\bar{t}}$$

n_w = refractive index of well material

n_b = refractive index of barrier material

n_c = refractive index of cladding material (*InP* for structures examined in this thesis)

λ = light wavelength

The TM power confinement factor for the active region of the structure in question is estimated using

$$\Gamma_{TM} = \Gamma_{TE}/1.2$$

This equation is based on numerical solutions (to Maxwell's Equations for a planar waveguide) for a range of structures similar to those described in this thesis (See Appendix E of reference [4]).

[1] T. P. Pearsall, *GaInAsP Alloy Semiconductors*, 362 (1982)

[2] W. Streifer, D. R. Scifres and R. D. Burnham, Appl. Optics, **18**, 3547 (1979)

[3] D. Botez, IEEE J. Quant. Elect, **QE17**, 178 (1981)

[4] J. Singh, *Semiconductor optoelectronics*, McGraw-Hill (1995)